Dissertation zur Erlangung des Doktorgrades
der Fakultät für Chemie und Pharmazie
der Ludwig–Maximilians–Universität München

INDIRECT TUNING OF THE CATHODIC PEMFC ELECTRODE MICROSTRUCTURE AND ITS FUNCTIONALITY FOR AUTOMOTIVE APPLICATION

LAURA FRIEDERIKE HERMANNS

aus
Düsseldorf, Deutschland

2017

Erklärung
Diese Dissertation wurde im Sinne von §7 der Promotionsordnung vom 28. November 2011 von Herrn Prof. Dr. Konstantin Karaghiosoff betreut.

Eidesstattliche Versicherung
Diese Dissertation wurde eigenständig und ohne unerlaubte Hilfe erarbeitet.

München, 01.03.2017

Laura Hermanns

Dissertation eingereicht am	26. Februar 2016
1. Gutachter:	Prof. Dr. Konstantin Karaghiosoff
2. Gutachter:	Prof. Dr. Christian Mohrdieck
Mündliche Prüfung am	04. April 2016

CREATIVITY IS THINKING UP NEW THINGS.
INNOVATION IS DOING NEW THINGS.

Theodore Levitt

ABSTRACT

A new generation of polymer electrolyte membrane fuel cells (PEMFCs) has started to enter the public market ahead with Toyota's model Mirai in 2015. Further on, several automakers also announced small scale production of fuel cell electric vehicles (FCEVs). Simultaneously the hydrogen infrastructure is aimed to be developed further in order to support FCEVs' market entry. In the last decade, PEMFC research has focused on characterization method development which should support the understanding of the catalyst layer (CL). Especially the CL's microstructure is not yet completely investigated. Due to the materials complexity, an accurate description of catalyst dispersions appears to be impossible. Hence, the present study focuses on experimental investigation of the catalytic ink particle size distribution and the corresponding catalyst layer morphology. An electrochemical evaluation was subsequently performed in order to categorize the CLs into sufficient or insufficient cell behavior. Therefore, a consecutive approach of parameter variation was carried out.

First, the manufacturing process of cathodic electrodes was investigated by selective analysis of catalyst layers resulting from diverse processed catalyst dispersions (mixing time variation). Second, the ionomer to carbon ratio (I/C) was varied in order to evaluate the pore network development and finally the particle size distribution was directly tuned with the goal to create differentiated catalyst layers. As a result, the mixing time and the particle size distribution tuning revealed detectable variations within the CL microstructure which were directly measurable with electrochemical testing. Hence, monomodal catalytic ink particle size distributions with a maximal size of 1 µm presented a 50 % reduced film thickness and slit shaped pores within the CL leading to a direct cell breakdown during electrochemical evaluation. In contrast, polymodal catalyst dispersions with a maximal size of 10 µm yielded well performing catalyst layers related to a sufficient pore and ionomer network which manage gas and proton transport, respectively.

These cell behaviors are predictable by using the identified catalyst dispersion and catalyst layer characteristics which include the state of the catalytic dispersion D*f*, the modality of the particle size distribution, the maximal particle size of the distribution x_{max}, the hysteresis loop of the resulting CL, and the specific surface area of the CL. A good cell performance was achieved when the catalyst dispersion presented a polymodal distribution below particle sizes of 10 µm, the absence of Mie scattering, and H2 type hysteresis loop for the resulting catalyst layer. On the other hand, poor cell performances are created with monomodal particle size distributions below 1 µm maximal size resulting in Mie scatter. Hence, a high particle packing density is observed within the CL so that slit shaped pores are created which induce a H4 type hysteresis loop and an early cell breakdown.

CONTENTS

1 Introduction 1

2 Aim of this work 3

3 State of the Art 5

3.1 PEMFCs for automotive application 5

3.2 Design and function of PEMFCs 5

3.2.1 Polymer electrolyte membrane (PEM) 6

3.2.2 Catalyst layer (CL) 7

3.2.3 Gas diffusion layers (GDL) 8

3.2.4 Bipolar plates 8

4 Experimental 9

4.1 CCM manufacturing and applied characterization techniques 9

4.1.1 Catalytic dispersions 9

4.1.2 Catalyst layers (CLs) 11

4.1.3 Catalyst coated membranes (CCMs) 15

5 Results and Discussion 17

5.1 Descriptive analysis of cathodic electrode production 17

5.1.1 Size reduction process of catalytic ink for cathodic catalyst layers 17

5.1.2 Determining the electrode´s microstructure by morphological analysis 22

5.1.3 Electrochemical component testing 30

5.1.4 Conclusion 32

5.2 Does the ionomer loading influence the pore size distribution and the overall electrode microstructure characteristics? 34

5.2.1 Catalyst dispersion analysis 34

5.2.2 Electrode analysis 35

5.2.3 Electrochemical component testing 40

5.2.4 Conclusion 43

5.3 CL microstructure tuning by particle size distribution variation of catalytic inks 45

5.3.1 Catalyst dispersion analysis 45

5.3.2 Electrode analysis 47

5.3.3 Electrochemical component testing 56

5.3.4 Conclusion 59

5.4 Discussion: Do the ink property settings determine the electrode microstructure independent of the deployed mixing technology? 61

6 Conclusion 69
7 Outlook 73
7.1 Hg–intrusion 73
7.2 Functional properties of cathodic catalyst layers 75
7.2.1 Sheet resistance 75
7.2.2 Adhesion force between catalyst layer and a substrate 77
8 Appendix 79
8.1 Samples for chapter 5.1 “Descriptive analysis of cathodic electrode production”. 79
8.2 Samples for chapter 5.2 “Does the ionomer loading influence the pore size distribution and the overall electrode microstructure characteristics?”. 79
8.3 Samples for chapter 5.3 “CL microstructure tuning by particle size distribution variation of catalytic inks” 79
8.4 Samples for 5.4 “Discussion: Does the ink property settings determine the electrode microstructure independent of the deployed mixing technology?”. 80
9 References 81

LIST OF ACRONYMS

AC	analytical centrifugation
ANOVA	analysis of variance
BET	Brunauer–Emmett–Teller
BEV	battery electric vehicle
BJH	Barrett–Joyner–Halenda
CAT	core automotive test
CCM	catalyst coated membrane
CL	catalyst layer
CO_2	Carbon dioxide
d	day
D*f*	fractal dimension
D[4;3]	volume–weighted mean particle diameter
EDX	energy dispersive x–ray
f	fraction of filled pores
F	filled pores with access to the gas phase
F	Fluorine
FCEV	fuel cell electric vehicle
FT	front tracking
FTP	fast transient polarization
g	gravitational force
GDL	gas diffusion layer
H_2	Hydrogen molecule
Hg	Mercury
HOT	heated operating condition
H&D	hot and dry condition
I	current
I/C	ionomer to carbon ratio
ICE	internal combustion engines
I(q)	scattering intensity
Ink	catalyst dispersion
ISO	International Organization for Standardization
IUPAC	International Union of Pure and Applied Chemistry
I–V curve	current–voltage curve
L	linear dimension

LO	laser and optical
MEA	membrane electrode assembly
MAT	MEA attribute tester
MLP	microporous layer
MT	mixing time
N_2	Nitrogen molecule
nanoCT	nanometer–Scale X–ray computed tomography
NOC	normal operating condition
OCV	open circuit voltage
OEM	Original Equipment Manufacturer
OPEC	Organization of the Petroleum Exporting Countries
PC	Polycarbonate
PEM	polymer electrolyte membrane
PEMFC	polymer electrolyte membrane fuel cell
PGV	particle size distribution
PSD	pore size distribution
PTFE	polytetrafluoroethylene
Pt	platinum
Q	scattering vector
R_a	averaged surface roughness
R_s	sheet resistance
RCF	relative centrifugal force
RH	relative humidity
SA	surface area
SEM	scanning electron microscopy
SLS	static light scattering
SOP	standard operating procedure
STP	standard temperature and pressure
TLP	transmitted light photography
wt %	Weight percentage
x_{max}	maximal particle diameter
XRF	X–ray fluorescence
Z	pore coordination number

ACKNOWLEDGMENT

I am using this opportunity to express my gratitude to everyone who supported me throughout my dissertation in particular the Chair of Inorganic Chemistry for Energetic Materials namely Prof. Dr. Konstantin Karaghiosoff and Prof. Dr. Thomas M. Klapötke. Further on, I would like to thank my current colleagues Dr. Helmut Rauner and Dr. Matteo Scolari who provided me the opportunity to become a member of the future-oriented fuel cell world within the Daimler AG. I am very thankful for their aspiring guidance, constructive criticism and idea-giving discussions.

My sincere thanks also go to all members of the PT/MBZ department who supported my work and research. Thank you all for being questioning and interested in my research results. I would like to highlight Matthias Pöhlmann, Sören Lindemann, and Julian Sorg who supported my research by performing imaging techniques such as SEM, nanoCT, and TLP. Additional thanks belong to Rajeevan Sivakumaran and Bernhard Wienk-Borgert who carried out the electrochemical and electric testing.

Last but not least, I would like to thank my family and friends for supporting me with their warmth, love, and humor throughout that time.

1 INTRODUCTION

“I do believe in the horse. The automobile is no more than a transitory phenomenon.” – this famous quote of Emperor Wilhelm II as a reaction to Carl Benz´s introduction of the first automobile in 1886 proves the evidence of misjudgment and uncertainties towards new arising technologies as its best. 130 years later, history shows that the automobile became by far one of the greatest inventions of the last centuries. Today, the automobile industry struggles again with new arising technologies and is trying to find its way to adaption. After the glory oil era, the global oil demand is still forecasted to reach 115 million barrels a day in 2035 which equals a 25 % increase of the present 92 million barrels a day in 2014.[1] In contrast, several opinions predict the global oil demand as far lower than the OPEC does. The powerful forces are named as the improvement of energy efficiency, the adoption of battery vehicles, hybrids, and fuel cell vehicles also towards truck fleets and the marine shipping, and the rising institution of carbon emission targets.[1] Especially the carbon emission targets force the OEMs to produce more zero–emission vehicles which include battery electric vehicles (BEVs) and fuel cell electric vehicles (FCEVs). Especially FCEVs benefit from higher well–to–wheel efficiency in comparison to common internal combustion engines (ICEs), acceptable ranges per filling of the tank (up to 600 km), and short refueling times. Simultaneously FCEVs face the hurdles of present energy intensive hydrogen production and a lacking H_2 infrastructure.[2,3] Therefore, the H_2 Mobility Initiative – founded in 2013 and transformed 2015 into a private joint venture covering six industrial companies – is expanding the total number of hydrogen filling stations across Germany to 400 by 2023.[4,5] Today, only a couple of dozen is found in Europe while California brings up 46 public stations and Japan will have completed 74 by early 2016.[6] The slowly arising stations demonstrate the complexity of matching the car roll–out process and the hydrogen infrastructure development.[6]

The CO_2 emission targets for the European Union are categorized into three levels: short term the upper CO_2 emission limit is reduced to 130 g CO_2/km (2012–2015), followed by a mid–term goal of 95 g CO_2/km (2020) which finally should reach 68 – 78 g CO_2/km by 2025 onwards.[2,7] Considering all sales market regions, a significant CO_2 emission reduction of averaged 28 % by 2020 is required.[2] As far as energy efficiency is improved, these goals could only be completed by the integration of reduced emission or zero–emission vehicles. Thus, the automotive industry is changing and once again it is demonstrating its agility towards emerging trends. The annual ranking of the “most innovative companies 2015” firstly presents equality in between technology companies and automakers within the top 10. Apple, Google, Microsoft, and Samsung place the first positions aside from Tesla Motors which is ranked at position 3. Toyota, BMW, and Daimler fill positions 6, 7, and 10, respectively.[8] All these companies launched successfully an alternative powered vehicle: Tesla Motors presented first a fully electrified sport car but is additionally not only an automaker but also an energy storage company that sells it battery components to competitors.[9,10] Tesla Motors understands its business concept as both hardware and software related.[10] Hence, Forbes magazine ranked Tesla Motors as the world´s most innovative company of 2015.[11] Toyota introduced the FCEV Mirai in 2015, while BMW experienced great success with its electric model i3 as the most frequently sold BEV in Germany in 2014.[6,12,13] Daimler started alternative powered car selling in 2009 with BEV and FCEV which demonstrated mature technology with the Mercedes–Benz F–Cell Word Drive in 2011.[14,15] Innovative companies are characterized by their ability of quick adoption to new technologies, implementation of lean research and development processes, and the application of digital, mobile, and big data.[8] Especially, occurring disruptive events challenge the companies and force them to immediate reaction. Today, four key areas are identified as such challenging topics which could lead the automotive industry towards a new golden age of technological advancement and automotive innovation which include the power train, lightweight

materials, connectivity, and active safety and assisted autonomous driving.[16] The automobile is changing from a collection of mechanical and hydraulic systems to a machine that is predominantly controlled by software and electronics.[16] Those trends are deduced from consumer research analysis and OEMs research and development spending as well as the numbers of patent fillings.[16] Further on, the automotive industry conversion and the application of new arising technologies are already visible in the present road transportation – even if FCEVs are still an exotic product.

Since Daimler belongs to one of the leading automakers focusing on fuel cell technology in Germany, this study presents experimental investigations of cathodic catalyst layers production processes and is trying to identify parameters that allow process efficiency increase so that cost reductions will pave the way for large–scale FCEV production.

2 AIM OF THIS WORK

The microstructure of polymer electrolyte membrane fuel cell catalyst layers is not yet completely investigated. Great effort in advanced characterization methods, especially electrode imaging and electrochemical analysis has taken place in the last decade.[3,17–19] But still, the common catalytic ink analysis techniques are lacking methods for the dispersion state analysis which also includes precise particle/agglomerate size distributions. Due to the materials complexity – highly porous catalyst powder with fractal geometries and networking ionomer with solvent depending swelling behavior – an accurate description of the catalytic ink appears to be impossible. Especially the selection of a suitable particle size analysis technique, which is usually utilizing light sources, is confronted with either black particles and complex refractive indices or transparent ionic polymers. Thus, the simultaneous detection of solid catalyst particles and a polymeric material represents insurmountable hurdles which lead to CL microstructure model development. Hence, the catalyst agglomerate size and other crucial characteristics such as the ionomer coating film thickness are estimated so that their impact on the CL formation could be evaluated.[17,20] In contrast to the widely used agglomerate models,[21–28] the present study focuses on experimental investigation of the catalytic ink particle size distribution. The catalyst particles/agglomerates serve as basis for the solid skeleton of the catalyst layer so that their distribution plays a key role for CL design optimization.[29,30] Epting et al. proposed that using a single agglomerate diameter as basis for modelling predictions is not adequate for precise results while using an agglomerate diameter distribution presented a far more sensitive output with approximately 70 % difference compared to the prediction running on a single agglomerate diameter.[30] This hypothesis validated for agglomerate model predictions should be reviewed within this study by experimental investigations.

Furthermore, the PEMFC electrodes consist of three components of which each is crucial for the overall fuel cell reaction: catalyst particles and their conductive support ensure the electron conduction, an interconnected ionomer network creates void space which serves as pore network for the gas transport and the ionomer itself guarantees the proton diffusion within the electrode.[17–19] The difficulty for electrode design optimization is the complexity of component interaction and mutual influence – in addition to applying suitable characterization methods. Thus, an ideal designed electrode includes reactant gases access to the catalytic active sites, proton and electron diffusion paths as well as water removal mechanisms avoiding gas diffusion path blocking.[17,18] Before CL design optimization could be performed, a deep understanding of the CL microstructure is needed. Especially the three networks build up by the catalyst particles, ionomer, and the resulting pores should be investigated within this study.

The goal of the present study is to identify characteristics within the catalyst coated membrane (CCM) production process which increase the overall cell performance. Thereby, raw materials, the applied production technologies as well as few material ratios are fixed which could reduce the expected output variation range. The investigated components include the catalytic ink, the catalyst layer (CL) coated on a decal substrate, and the CCM. Within this study, nitrogen physisorption analysis should be performed in addition to common optical microscopy techniques for CL analysis. Furthermore, the characterization of the catalytic ink is focused and its particle size distribution as well as stability and internal dispersion state analysis are introduced. According to the applied characterization techniques, adapted to fuel cell materials, promising results are expected in order of clear correlation between the three components catalytic ink, CL, and CCM. The hypothesis of indirect fuel cell performance tuning by adjusting the catalyst ink properties should be verified following the outlined approach (Fig. 2.1, bullet point 1).

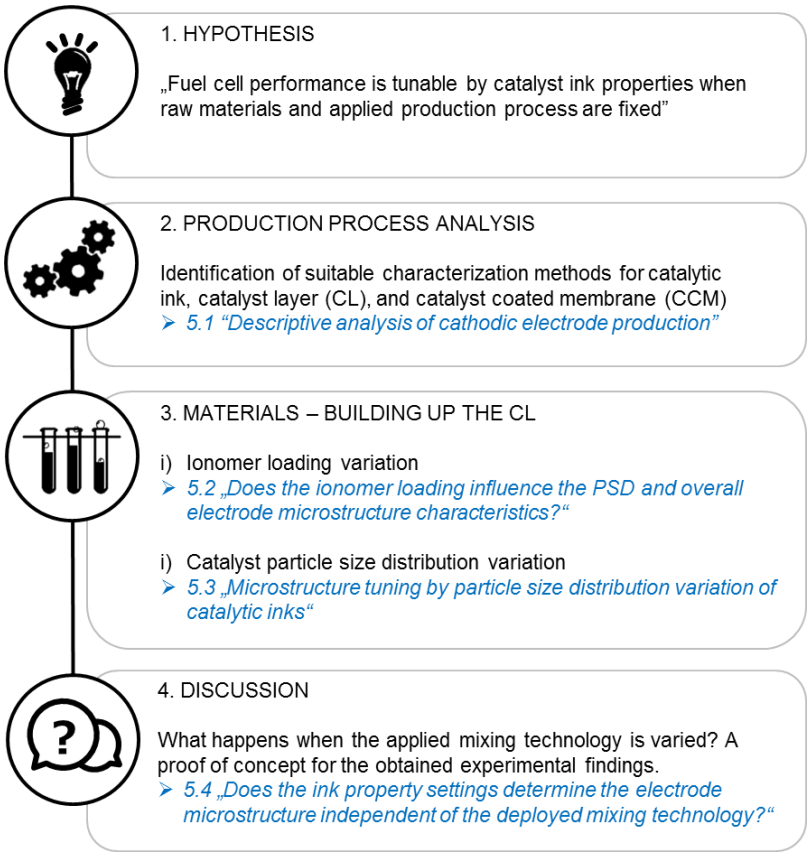

Fig. 2.1 Strategic outline for the present study.

After formulating the hypothesis, the present cathodic electrode manufacturing process should be investigated with respect to catalytic ink, electrode morphology, and catalyst coated membrane performance analysis. Relevant characterization techniques should be identified and further applied (Fig. 2.1, bullet point 2). Then, the electrode microstructure should be investigated by a consecutively variation sequence including ionomer loading and catalyst layer particle size distribution widths. Thereby, solely one parameter is changed at the same time so that first the ionomer loading is adjusted while platinum loading, solid contents, the solvent system ratio, the applied mixing energy and the resulting catalytic ink particle size distribution should remain constant. Second, a suitable ionomer loading is chosen and fixed whereas a range of diverse catalytic ink particle size distributions should be created. Here, the essential parameter platinum loading should also be fixed in order to guarantee comparable valid interpretation. All microstructural experiments should be completed with electrochemical single cell testing so that correlations between CL microstructural properties and cell behavior could be identified.

In conclusion, the experimental findings and correlations should be reviewed with a proof of concept by applying a diverse mixing technology. The goal is to create an identical ink particle size distribution so that the manufactured electrodes achieved from these two mixing technologies could be investigated and feasible differences revealed (Fig. 2.1, bullet point 4).

3 STATE OF THE ART

3.1 PEMFCs for automotive application

The applicability of polymer electrolyte membrane fuel cells (PEMFCs) has changed from a lab scale product into the most probable successor for automotive manufacturers during the last century. However, the first fuel cell was discovered by Christian Friedrich Schoenbein in 1838 already. It was considered as interesting "gas battery" but it took over a century until the first fuel cell was tested in a vehicle.[3,17] From 2005 onwards, the first production-ready passenger vehicles became public with a new generation of fuel cells. In contrast to prior handmade prototypes, these few hundred examples were produced by assembly lines and field tested in order to demonstrate mature technology. The Mercedes F-Cell B-Class, the Chevrolet Equinox FC, and the Honda FC-X Clarity presented approximately 90 kW fuel cell power, 150 km/h top speed, and 100 000 km durability. Further on, one tank covered 350 – 400 km and the refueling procedure was executed within less than 4 minutes. In 2015, a next generation of fuel cells entered the market in small quantities whereby Toyota's Mirai was the first of several announcements.[3,12] But still, FCEVs suffering from high production costs and durability targets as well as from fragmentary hydrogen distribution infrastructure.[2,3,31] Additional PEMFC power plant requirements are identified as high reliability and mass manufacturability. Future FCEVs need to fulfill a power target of approximately 80 kW in order to power a light-duty automobile.[32] Further power plant improvements coupled with smarter H2 tank integration are expected to increase the vehicle's range and the systems efficiency. Moreover, automotive industry is aiming to increase the durability standard of 2000 h towards 8000 h.[3]

In order to compete with traditional internal combustion engines (ICEs) the automotive fuel cell system costs need to be reduced to $25/kW.[3] The United States Department of Energy (DoE) annually presents a study for costs of a single automotive fuel cell system on the assumption for a yearly production of 500 000 vehicles: the former costs of $105/kW in 2006 are reduced by 48 % to $50/kW in 2014 which equals $24/kW for a PEMFC stack. The cost target for 2020 is aimed of $40/kW while an ultimate target for PEMFC systems after 2020 is set as $30/kW (80 kW PEMFC system, 500 000 units/year).[32,33] This promising data is related to ongoing MEA design optimization development which presents by far the most cost intensive component: on FC stack level, the MEA constitute 70 % while on FC system level it contributes 50 % of the total costs. Thus, the platinum loading was reduced from initial 1 mg/cm² ten years ago to present 0.35 mg/cm². Furthermore, industry is aiming for a platinum loading of 0.2 mg/cm².[3,33] Concluding, cost reduction will only be successfully completed by deepening the understanding of the MEA and its structural components.[3,34]

3.2 Design and function of PEMFCs

Polymer electrolyte membrane fuel cells (PEMFC) are designed for automotive application which means that they are operating at low temperatures. This fact reduces the design requirements a bit but on the other hand several properties such as resistance to high power densities, start-stop operation, and temperature varieties must be fulfilled.[17,18,35] Therefore, several components and materials are commonly used for PEMFC manufacturing which are described below. For most of the components (GDLs, PEMs, and CLs) and their manufacturing processes a large number of ref-

erences can be found within the literature.[3,17,19,36–40] Regarding the preparation of the catalytic ink dispersion, less literature is available: mostly the impact of organic solvents to the resulting electrode microstructure and the structure itself is investigated.[29,41–47] Many control levers within the catalytic dispersion have been reported but most of them were modelled only.[20,22,27,48,49] Few sources correlate classical colloidal dispersion findings[50,51] to the fuel cell system such as the thesis of Schlumbohm does.[52]

A fuel cell stack needs to power an engine – the automobile – so that a high cell performance is required. This is ensured by stacking hundreds of single fuel cells resulting in the fuel cell stack. The so–called single fuel cell consists of a membrane electrode assembly (MEA) which is embedded between two bipolar plates (chapter 3.2.4).[3,35] The MEA itself includes the catalyst coated membrane (CCM), a membrane which is usually a polymer electrolyte membrane (PEM; chapter 3.2.1) and the catalyst layers (CLs; chapter 3.2.2) designed as cathode and anode electrodes. The CCM is the powerhouse of the fuel cell since the electrochemical reaction takes places: the hydrogen molecule is ionized into protons and electrons from which the protons only are transported through the membrane (Eq. 3.1). The remaining electrons create a potential difference between the electrodes so that a direct current is induced which powers the electric motor. The cathode electrode is fed with oxygen which will be reduced into the reaction product water (Eq. 3.2). In order to guarantee water transport within the cathode, a sufficient porosity is required which is described in chapter 3.2.2.[17,38] Eq. 3.3 present the overall fuel cell redox reaction.

$$2H_2 \rightarrow 4H^+ + 4e^- \qquad \textbf{Eq. 3.1}$$

$$O_2 + 4H^+ + 4e^- \rightarrow 2H_2O \qquad \textbf{Eq. 3.2}$$

$$O_2 + 2H_2 \rightarrow 2H_2O \qquad \textbf{Eq. 3.3}$$

3.2.1 Polymer electrolyte membrane (PEM)

The membrane framed with anode and cathode, is responsible for the PEMFC durability and therefore also one of the most important components of a fuel cell which directly influences its lifetime. The membrane's function is to exchange protons between anode and cathode side which explains its second common name proton exchange membrane (PEM). Furthermore, the membrane is insulating towards electrons and prevents gas crossover events for the reactants (H_2 and O_2). For proper fuel cell operation, the membrane needs a precisely adjusted level of hydration so that ionic transport (proton conduction) throughout the membrane is guaranteed.[38,53] The perfluorosulfonic acid (PFSA) membrane Nafion® manufactured and distributed by DuPont™ is the most common PEM for automotive application.[54] Its chemical structure is shown in Fig. 3.1: the backbone structure ensure mechanical strength while the sulfonic acid groups manage the proton transport.[53–55]

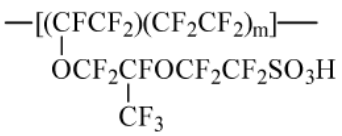

Fig. 3.1 Chemical structure of Nafion.[54]

Polymer electrolyte membranes face diverse stressing events during automotive operation: rapid changing loads such as start/stop or freeze/thaw operations can damage the membrane. Here, different mechanisms are literature known such as the chemical or mechanical degradation.[18]

These processes can develop pinholes within the membrane so that gas transport through the membrane can occur resulting in a system short-circuit which is the main cause for fuel cell failure.

3.2.2 Catalyst layer (CL)

The catalyst layer (CL) is the most important component of a fuel cell by hosting the electrochemical reaction at the metal/electrolyte interface.[17] Besides this main reaction, several processes are running simultaneously which include interfacial charge transfer, electron and proton transport, as well as reactant gas (O_2 and H_2) and product mass (H_2O) transport.[17] Thus, the catalyst layer morphology should support the proceeding reactions which is realized through the application of porous materials loaded with catalyst particles (Fig. 3.2).[3,17,19] The advantage of porous carbon materials is their conductivity and high surface areas so that they are typically found in electrochemical energy conversion and storage applications such as capacitors, photoelectrochemical cells, batteries, and fuel cells.[17] Especially the large surface area is favorable for the formation of large interfaces with the electrolyte which allows the generation of high power densities within the catalyst layer.[3,17,56] Characteristic platinum particles present diameters of 2 – 5 nm while their support material exists as primary particles with averaged diameter of 5 – 20 nm. Primary fuel cell carbon support is usually carbon black or graphitized carbon black which is further aggregated into agglomerates (~100 nm diameter) or aggregates (~1 µm diameter).[46,57,58] The resulting structures demonstrate diverse pore types which are categorized into micropores between crystalline domains inside the primary carbon particles (<2 nm), mesopores of 2 –50 nm diameter inside agglomerates, or macropores (>50 nm) between agglomerates.[17,46] Fig. 3.2 illustrates a typical fuel cell catalyst layer morphology.[17] The original classification of pores was initially proposed by Sing et al. for IUPAC application and further adapted by the fuel cell community so that meso- and macropores are also referred to as primary and secondary pores, respectively.[17,29,46,59] These types of pores are directly linked to the electrochemical reaction: hydrophilic primary pores are partially filled with liquid water while the larger more hydrophobic secondary pores manage the gas transport.[17,60]

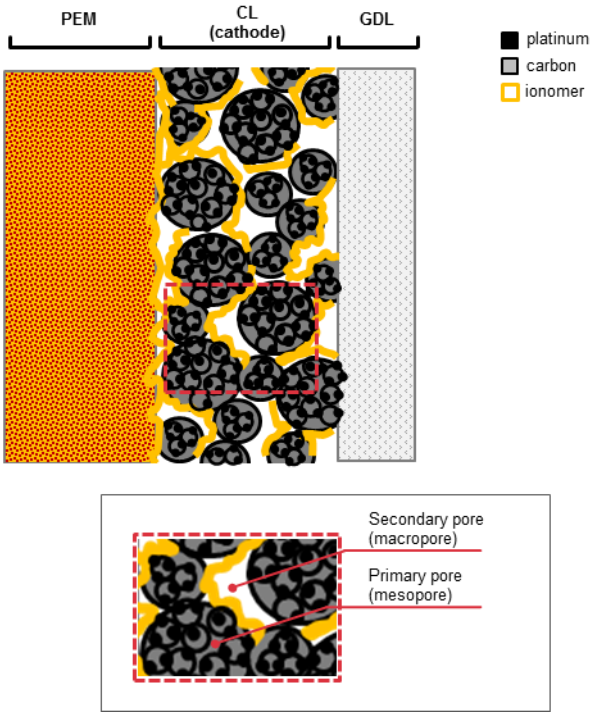

Fig. 3.2 Catalyst layer morphology sketch. Micropores are found inside primary carbon particles while meso- (primary) and macropores (secondary pores) are formed inside or between carbon agglomerates, respectively.[17]

Today, fuel cell research focuses on understanding correlations between structural insights and physical or electrochemical properties. The results often support material development and design optimization. Especially the progress within nanotechnology and instrumentation revealed more precise characterization within the nanometer or subnanometer scale. In general, catalyst layer characterization is mainly based on 2D or 3D microscopic or scattering techniques. Microscopic characterization has the drawback of small local region analysis but benefits from real–space observation of investigated morphologies. In contrast, scattering techniques represent large sample areas and result in statistical averaged information but simultaneously require a model for interpretation which is based on several assumptions. Thus, the question is usually not which of these two characterization types is the best for structural analysis but rather the combination of both reveal the most information.[3] 2D electron microscopy techniques such as scanning electron microscopy (SEM), field–emission (FE)–SEM, transmission electron microscopy (TEM), high–resolution TEM (HRTEM), TEM–energy dispersive X–ray spectroscopy (EDXS), scanning transmission electron microscopy (STEM), and 3D electron microscopy (ET) are standard characterization techniques for catalyst, carbon support, and ionomer analysis. Here, the catalyst particle size, distribution, as well as its dispersion on the carbon support is investigated. Regarding catalyst development and durability studies, the particles sizes are characterized before and after fuel cell operation in order to evaluate platinum nanoparticle growth or carbon corrosion phenomena.[3,18] Catalyst layer porosity and composition analysis are carried out by porosimetry (mercury intrusion porosimetry, MIP, or standard contact porosimetry, SCP), physisorption, and X–ray photoelectron spectroscopy (XPS).

Advanced microscopic techniques include additives such an *in-situ* TEM sample holder or the environmental SEM (ESEM) whereby realistic atmospheres are created. For example ESEM technique allows the addition of small volumes of diverse gases or water vapor so that MEA images are captured under quasi *in-situ* humid conditions. Thus, further MEA characteristics such as wettability, water transport behavior or ice growing mechanisms could be collected which support understanding the complex collaboration of the single MEA components.[18]

3.2.3 Gas diffusion layers (GDL)

Porous gas diffusion layers manage the reactants' (H_2 and O_2) distribution towards the catalyst layers and frame both anode and cathode (Fig. 3.2).[19,53] Owed to the GDLs' position within a MEA – connecting the catalyst layers and bipolar plates – they need to be electrically conductive. GDLs are manufactured from porous carbon papers with a thickness ranging from 100 – 300 µm and presenting porosities of 80 % and pore diameters of approximately 10 µm, respectively.[19] Additionally, they support the mechanical strength with their carbon network and improve the water management of the MEA: therefore, the carbon papers are impregnated with hydrophobic polymer (PTFE).[19,37] Moreover, the GDL is coupled with an additional microporous layer (MPL) on its catalyst layer contact side with respect to increased mass transport ability at high current densities.[37]

3.2.4 Bipolar plates

Bipolar plates cover a range of functions in order to support and protect a single cell unit. These functions mainly include electron transfer and macroscopic gas distribution so that the plates need to present electrical and thermal conductivity which are typical properties of metals. The plates are manufactures with a channel structure on their surface so that they are often titled as bipolar plates. Several structures are applied which include channel, finger, or mesh appearance. Their manufacturing becomes challenging due to the requirement of minimal thickness related to their weight which present the main fraction of one unit cell. Further on, the microscopic gas distribution is carried out by the porous GDLs. Moreover, the plates support the mechanical strength of the complete stack and separate unit cells from each other. Furthermore, the plates need to present high corrosion resistance which is usually achieved by the use of graphite plates. When metal plates should be utilized they require an additional protection coating in order to demonstrate the corrosion resistance. Today, graphite plates are predominately deployed due to their natural corrosion resistance. Further on, ideal bipolar plates manage pressure drop over the transportation path and production water removal.[19]

4 EXPERIMENTAL

4.1 CCM manufacturing and applied characterization techniques

Samples for investigation are taken from the CCM manufacturing process that included the catalytic dispersion (ink), the catalyst layer (electrode), and the catalyst coated membrane (CCM). Catalytic inks consisted of Pt–supported carbon, 25 wt% ionomer dispersion, and a fuel cell solvent (water, primary organic alcohols, and solvent mixtures). The weight percentage of the solid components ranged in between 8 wt% and 10 wt%. The ink mixing process covered a seven day processing time using a roll mixing technology. After terminating the mixing procedure the ink was coated to a decal substrate which yielded the cathodic catalyst layer (electrode). Finally, the CL was transferred to a fuel cell membrane using a hot–pressing roll to roll process. More details on fuel cell catalyst layer preparation can be found in the literature.[40,42–44,52]

4.1.1 Catalytic dispersions

The catalytic dispersions were analyzed using static light scattering technique and analytical centrifugation.

Static light scattering. Laser diffraction experiments were performed at 22° C using the Mastersizer 3000 with the Hydro SM dispersion unit (Malvern Instruments Ltd.) according to ISO 13320 (2009).[61] Temperature was controlled by a Thermo Scientific Haake Circulator ARCTIC SC 100 – A10. Results were obtained as volume–weighted particle size distributions and averaged of 10 measurements. Samples were prepared by adding 0.05 g ink into 5 g of solvent which were continuously mixed before usage. The measurement cell eluent equaled always the utilized solvent. For the measurement 0.6 ml of the prepared dilution were injected into the dispersion unit resulting in a final dilution of 1:10 000. The sample flow was set as 1000 rpm and a target laser obscuration of ~10 % was aspired. The Mastersizer Software directly calculated characteristic parameters such as the volume–weighted mean diameter D[4;3] and the 10 %–quantile Dv[10], 50 %–quantile Dv[50], and the 90 %–quantile Dv[90] for the corresponding cumulative particle size distribution.[62,63] The three quantiles were used for boxplot presentation of the corresponding particle size distributions complemented with their maximal and minimal particle sizes. Likewise, a particle size distribution plot was extracted from the Malvern Software following the representation norm.[61] The relative amount of small particles (< 0.3 µm) was extracted from the particle size distribution plot: the distribution curve was mathematically integrated using OriginPro® software. A threshold was set at 0.3 µm so that the relative fraction of small–sized particles could be calculated. Further on, the fractal dimension D*f* was calculated using the scattering intensity I(q) and its corresponding scattering angle θ data which was transformed into the scattering wave vector Q using Eq. 4.1 where n is the refracted index of the solvent and λ is the laser wavelength of the used laser light source.[64–66]

$$Q = \left(\frac{4\pi n}{\lambda}\right) sin\frac{\theta}{2} \qquad \textbf{Eq. 4.1}$$

Plotting this data as a double logarithmic plot I(q) versus Q allows the determination of the fractal dimension D*f* within the Q–range which is limited by the light scattering instrument's detection range with θ_{min} = 0.015° and θ_{max} = 144°. The resulting slope of the data sets within the Q–range equal the fractal dimension D*f* (Eq. 4.2, Eq. 4.3).[64,66,67]

$$I(q) \approx q^{D_f} \qquad \textbf{Eq. 4.2}$$

$$\log I\,(q) = -D_f \log q \qquad \textbf{Eq. 4.3}$$

Within this work three different types of D*f* values were detected which could be categorized into D*f* > 1 for aggregated and D*f* < 1 for non–aggregated catalytic dispersions, respectively. These inks were characterized with polymodal particle size distributions whereas monomodal distributions below a maximal particle diameter of 1 µm demonstrated Mie scattering which is typically observed for monodispersed colloidal dispersion.[64] Further on, dispersions presenting Mie scattering also demonstrated high dispersion stability which is illustrated in Fig. 4.1.

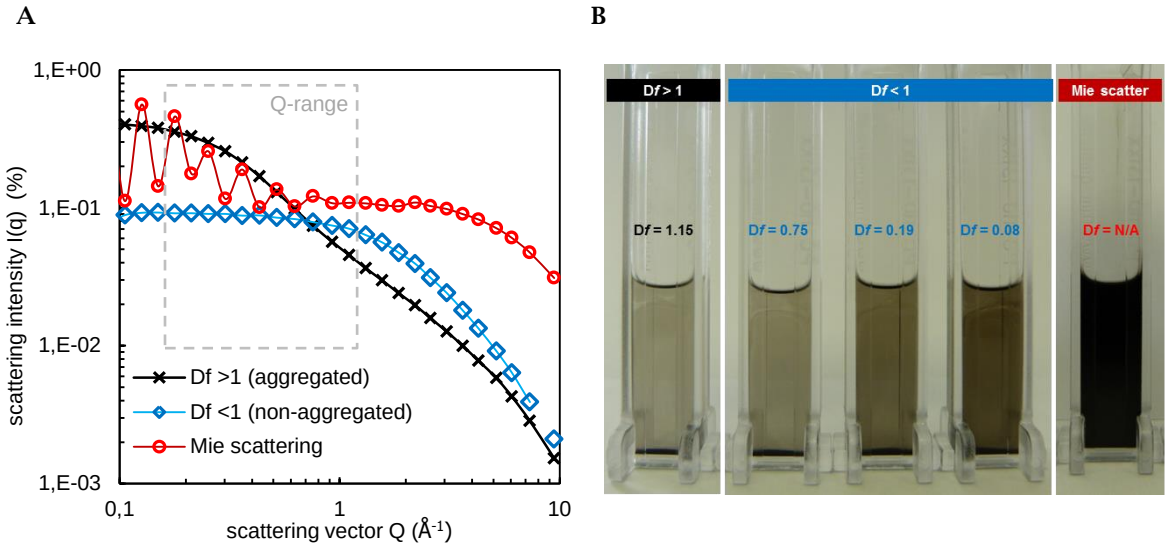

Fig. 4.1 Log–log plot for internal structure analysis of catalytic dispersions (**A**). Scattering intensity I(q) and scattering vector Q are obtained from static light measurements. The plot present three identified dispersion levels: aggregated (D*f* >1), non–aggregated (D*f* <1), and Mie scattering that invalidates D*f* determination. (**B**) presents the corresponding catalytic dispersions after centrifugation for 20 min at 2300 g.

Analytical centrifugation. Analytical centrifugation experiments of catalytic dispersions were carried out according to ISO 13318–2 using the 8–channel LUMifuge LF 1112–62 with a light source of 865 nm (L.U.M. GmbH) and SEPView® 6.4 Software.[68] Polycarbonate (PC) cells with path length of 2 mm were used. Standard operation measurements (SOPs) for 0.01 wt% catalytic dispersions were performed at 22° C, 4000 rpm, and 2300 g for 20.8 min. Front tracking (FT) analysis was applied by SEPView® software. The measured transmission data was analyzed within 107 – 129.8 mm using a moving average (9 points) and a threshold of 15 % transmission. The resulting sedimentation velocity at 2300 g was converted into sedimentation velocity at gravity, on condition that a linear correlation between the relative centrifugal force (RCF) and the corresponding sedimentation velocity existed.[69]

4.1.2 Catalyst layers (CLs)

Catalyst layers were investigated with a range of *ex-situ* characterization techniques. Therefore, a systematic approach was the method of choice (Fig. 4.2) whereby first the surface appearance was analyzed focusing on diverse resolutions and sizes of investigation area followed by cross-sectional and internal structure analysis (Table 4.1). Each technique yielded different characteristics so that a complete three-dimensional result is expected.

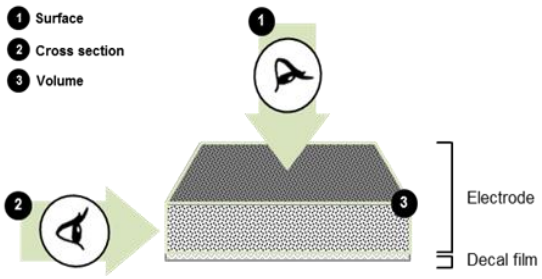

Fig. 4.2 Systematic approach for catalyst layer characterization.

Table 4.1 Specific investigation areas for the applied characterization methods.

CL section	Method	Investigated area/ volume	Output
Surface **(1)**	Laser confocal microscopy	5.6×10^{-4} cm²	• roughness • crack area
	Nanometer-scale X-ray computed tomography (nanoCT)	2.0×10^{-2} cm²	• crack area
	Transmitted light photography	6.4×10^{1} cm²	• void area
	Scanning electron microscopy	6.0×10^{-3} cm²	• particle morphology
Cross section **(2)**	Scanning electron microscopy	$1.6 - 2.2 \times 10^{-6}$ cm²	• thickness • material distribution
Internal structure **(3)**	N_2 physisorption	1.5×10^{2} cm² 0.10 – 0.14 cm³ 0.35 – 300 nm	• internal surface area • pore volume • pore size distribution

Laser confocal microscopy. Catalyst layer surface analysis was performed with the laser confocal microscope VK-9710 and a 50-times magnification lens (Keyence Corporation). The recorded images were further processed with the corresponding VK Analyzer Software by applying tilt correction and noise reduction. Additionally to the laser and optical (LO) image a 3D picture was captured which was used for crack area calculation (Fig. 4.3, A). Here, a programmed MATLAB algorithm (The MathWorks, Inc.) was applied which originally was developed for TLP image analysis and yielded a binary image (Fig. 4.3, B; see "Transmitted light photography"). Further on, the algorithm identified the amount and size of black and white pixels so that the cumulative crack area (black pixels) was calculated from the ratio of black pixels related to the total amount of pixels.[70] Moreover, the averaged surface roughness R_a was received from VK Analyzer Software.

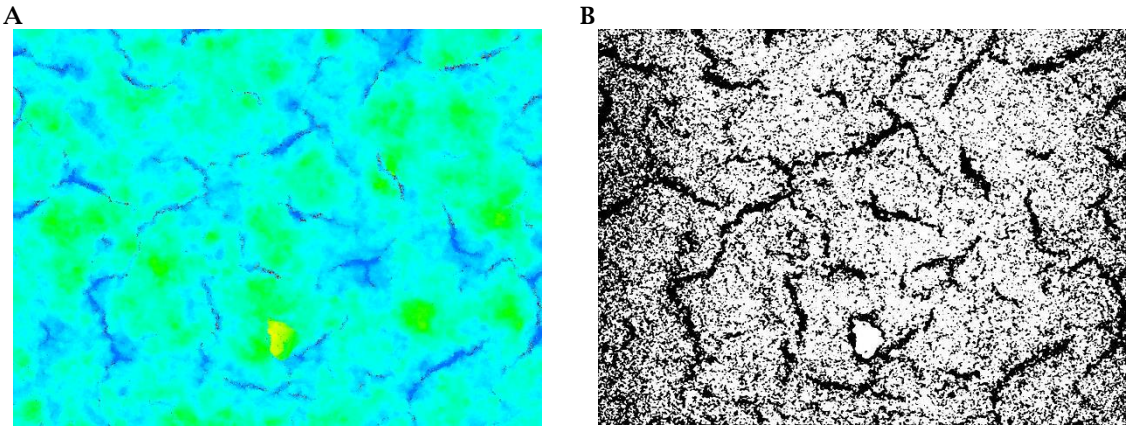

Fig. 4.3 3D-laser confocal microscope image (**A**) and the corresponding binary image (**B**) extracted from the MATLAB algorithm.

Nanometer-Scale X-ray computed tomography (nanoCT). A 0.25 cm² sample was used for CL surface visualization recorded by the nanoCT® system phoenix nanotom m (General Electric Company; voxel size of 300 nm and 160kV acceleration voltage). The sample was fixed with tape on its horizontal edges on a glass substrate stabilized for the standing position during nanoCT® imaging (Fig. 4.4). Recorded images were used for crack area calculation using an algorithm programmed with MATLAB (The MathWorks, Inc.) originally developed for TLP image analysis (see "Transmitted light photography").[70] The amount of black pixels related to the total amount of pixels was used for crack area identification.

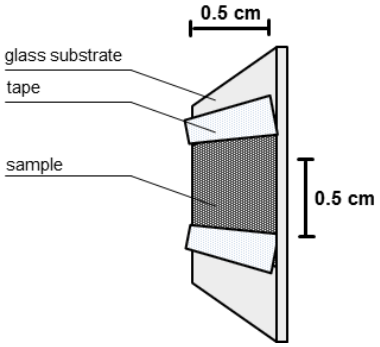

Fig. 4.4 Illustration of sample preparation.

Transmitted light photography. Transmitted light through the CL sample was captured with the SLR camera Nikon D5500 (Nikon GmbH). The investigated samples were cut into 8 x 8 cm pieces (64 cm²) and were covered with a dark plate. Camera settings were adjusted to 1/10 sec exposure time, ISO image sensitivity of 10 000, and maximum aperture of 3.2 for cathodic catalyst layers. The transmitted light desk was run with 1.8 A and 24 V. The distance between the sample and the camera lens was 663 mm. The picture capturing was initiated by closing the dark room and triggering the shutter. Further on, the recorded images were processed using an algorithm programmed with MATLAB (The MathWorks, Inc.): The original image was converted into a binary one using a fixed threshold which was identified by the Otsu method.[71] In order to find the best fitting threshold, a range of thresholds were applied framing the Otsu threshold. Hence, the amount of voids (white pixels) is used as parameter for CL characterization.[70]

Scanning electron microscopy. CL surfaces and cross sections were visualized with TESCAN Mira 3 XM SEM, coupled with a high brightness field emission gun.

Nitrogen physisorption. The characteristic specific surface area (BET SA), pore volume and pore size distribution of catalyst layers were obtained by applying nitrogen physisorption using an AUTOSORB–iQ MP (Quantachrome GmbH & Co. KG) in the partial pressure range of 0.025 – 0.998. Cathodic catalyst layers show both micro– and mesopores which render it necessary to apply two methods. A classical macroscopic, thermo–dynamic concept in combination with a statistical model reported a realistic pore description for each category. Thus, the BJH method was applied for meso– and macropores ranging from 2 – 300 nm pore width while a slit/cylindrical QSDFT model was used for micropores and narrow mesopores (0.4 – 35 nm pore width).[72–76] The total pore volume was found at 0.998 P/P_0 by conversion to the liquid N_2 volume using the conversion factor of 0.001 547, under the assumption that the density of condensed N_2 in the pores is equal to the density of bulk liquid N_2.[46,77] Further on, the sorption isotherm and its hysteresis loop are categorized according to IUPAC classification (Fig. 4.5).[59]

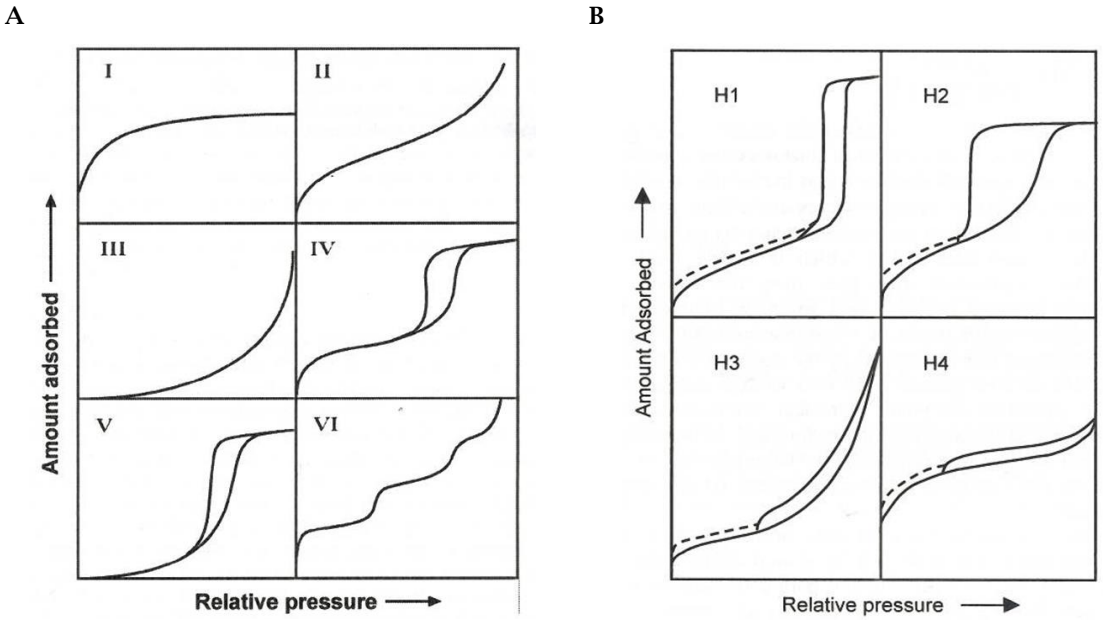

Fig. 4.5 IUPAC classification for sorption isotherms (**A**) and their hysteresis loops (**B**).[59] BET method is applicable only to sorption isotherms presenting type II and IV (non–porous or macroporous solids or rather mesoporous solids with pore diameter between 2 nm and 50 nm).[78]

Sample preparation was carried out as in Fig. 4.6 described: a cathodic coated decal (KCD) retainer was cut in 10 x 15 cm sample size which further was cut in half. The sample pieces were shaped into a roll with a maximum diameter of 10 mm guaranteeing the usage of 12 mm sample cells. The KCD sample was degassed at 90° C for 5 h prior to the sorption experiment which was performed immediately afterwards. Therefore, the sample weight before and after degassing must be known. The sorption experiment itself was performed at 77K with Nitrogen as adsorbate gas. The measurement protocol included 46 adsorption and 48 desorption data points. Recorded data was reported in pore diameter (nm), pressure (torr) in its corresponding relative pressure (P/P_0), adsorbed volume in cm^3 plotted in linear diagrams (s. isotherm diagrams; Fig. 5.9, Fig. 5.20, Fig. 5.34). In order to determine the weight of the coated electrode without the decal substrate, the electrode was washed of using ethanol. Then, the blank decal was weighted again which yielded the indirect electrode weight. This process contained a weighting error of approximately 1%. The deviation in between similar electrodes was recorded as 9% which mainly occurs from local structure differences of the electrode itself. The instruments deviation is stated as 1% and yielded a repeatability of 6% for the investigated cathodic electrodes. The adsorption ability of the decal substrate was identified as negligible with a measured pore volume of 0.0004 cm^3/g. Hence, the recorded isotherm data was corrected to the effective electrode weight under the assumption of no significant influence of the substrate. The BET SA was calculated from the multi–point BET slope using the adsorption data in between 0.05 – 0.30 P/P_0 according to ISO 9277:2010 and additional correction performed by the Micropore BET Assistant within the ASiQwin Software.[78]

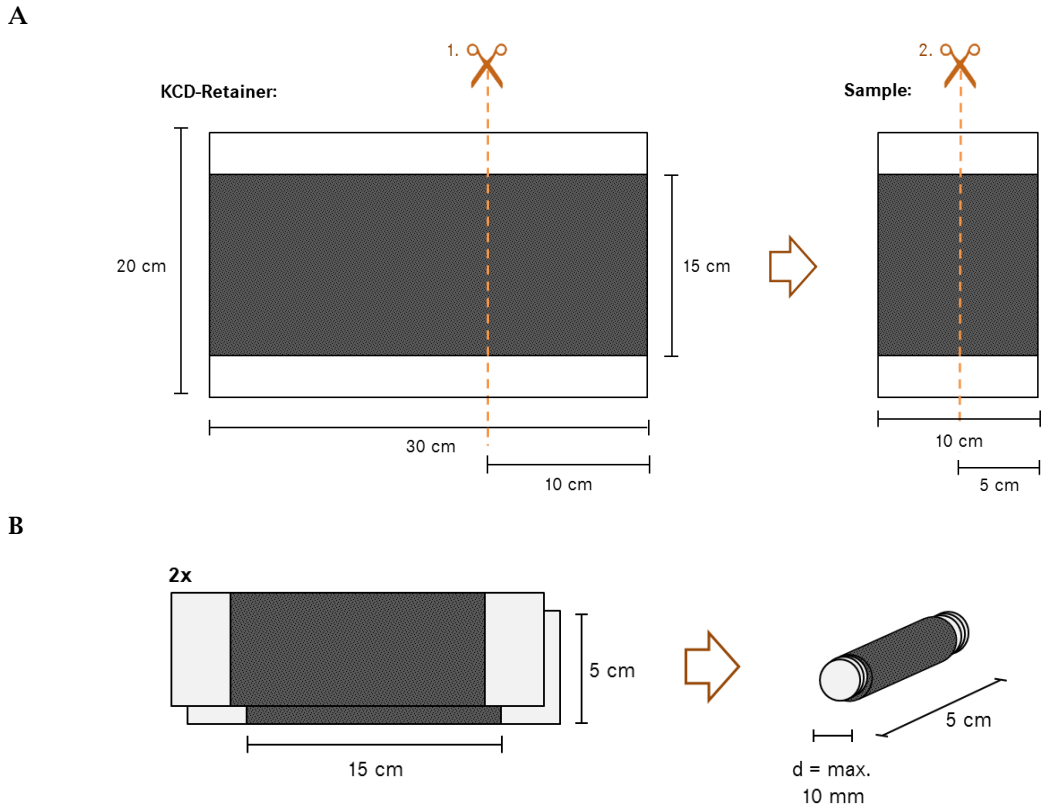

Fig. 4.6 Sample preparation of cathodic coated decals (KCD retainer) for nitrogen physisorption.

Using the advanced pore network analysis proposed by Seaton et al., allows the determination of the mean coordination number of the pore network Z and the size of a typical microparticle which is expressed as a number of pore length L which are both deduced from the sorption hysteresis loop.[79–82] Therefore, Eq. 4.4 is used which describes the relation between Z and L related to f and F which present the fraction of filled pores f and filled pores with access to the gas phase F, respectively.[83] The modelling study of Kirkpatrick et al. resulted in a generalized scaling function which is used for calculation: the measured sorption data is fitted to this scaling function which uses the critical exponents $\beta = 0.41$ and $\gamma = 0.88$. Further on, the least square method was applied in order to find the best fit.[84]

$$L^{\frac{\beta}{\gamma}} ZF = h\left[\left(Zf - \frac{3}{2}\right) L^{\frac{\beta}{\gamma}}\right] \qquad \textbf{Eq. 4.4}$$

Mercury intrusion. Hg-intrusion measurements were carried out using a Poremaster-60-GT instrument (Quantachrome GmbH & Co. KG). The measurement procedure followed DIN 66133.[85] The measurement range covered pore diameter of 3.6 nm to 150 µm (using a contact angle of 140°) which needed to be divided into the low pressure range (200 µm – 4.3 µm) and the high pressure range (10.7 µm – 3.6 nm). The applied Poremaster® software (version 8.01) achieved transition between those sections within the overlapping range. Furthermore, few measurement requirements needed to be fulfilled in order to obtain the pure measurement signal for the catalyst layers: the decal substrate, a plastic film, produced additional signals due to its elastic deformation at high pressures (here, maximal 4000 bar). Thus, a simultaneous measurement of a blank decal substrate – equaling the CL sample decal in its mass and geometry – was performed. The obtained data was used for subtraction from the CL measurement data so that the resulting difference equaled the pure measurement signal of the porous CL. For the sample preparation a CL was cut into twenty slices of about 7.5 mm width which presented sufficient material for one

measurement. Before starting the measurement, the CL on decal was weighted and subsequently after measurement washed off with ethanol and dried at 60° C. The resulting weight was used for effective CL weight calculation which was further used for data correction.

Sheet resistance. In-plane conductivity (or sheet resistance) measurements of CLs were performed using the four-point probe measurement approach (Fig. 4.7).[40,86] Here, the sample geometry is correlated to the measured resistances R_s and resulting material properties so that diverse correction factors needed to be respected. According to Eq. 4.5, F_{1D} takes the influence of the sample's film thickness into account and F_{2G} its geometrical properties such as length and width, while F_{3S} includes the offset of the four tips from the center point of the investigated sample.[40] Further on, the current flowed in between the outer tips (15 mA) while the inner tips were included into potential measurements. Samples were cut into 5 x 5 cm pieces before investigation. Their thicknesses were extracted from SEM experiments.

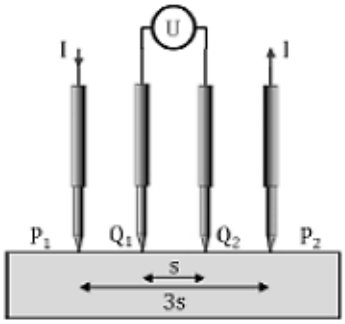

Fig. 4.7 Four-point probe measurement technique for in-plane conductivity characterization.[40,86]

$$R_s = \frac{U_V}{I} F = \frac{U_V}{I} F_{1D} F_{2G} F_{3S} \qquad \textbf{Eq. 4.5}$$

Adhesion test (adhesion CL/decal substrate). The tensile and shear adhesion force between the catalyst layer and its decal substrate was investigated with a shear test proposed by Frölich et al.[40] Therefore, an adhesive (19 mm wide, type H5413, 3M) was attached to the CL surface and its interface loaded until failure (tensile tester Z2.5 zwickiLine, Zwick Roell; testing speed: 2 mm/min). The maximal force meaning the shear strength was used as characteristic parameter. The test results were considered as valid when the catalyst layer was completely removed from the decal substrate. For sample preparation CLs were cut into 5 x 1 cm² pieces and the adhesive placed as Fig. 4.8. illustrates.

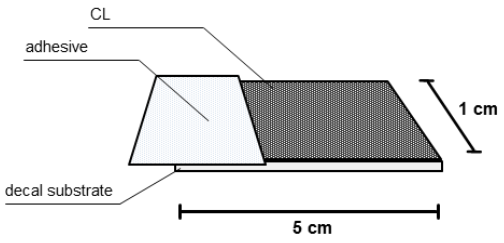

Fig. 4.8 Illustration of a prepared sample for adhesion test.

4.1.3 Catalyst coated membranes (CCMs)

CCMs were electrochemically investigated using two types of single-cell measurements: MEA attribute testing (MAT) and core automotive testing (CAT) which differ predominantly in investigation area. MAT worked with circular 3 cm² and CAT with rectangular 40 cm² of active area where-

as CAT is more realistic to stack testing due to its MEA geometry and flow field application.[39] Both testing methods recorded characteristic current–voltage curves (I–V curves) during constant temperature, relative humidity (RH) or gaseous stoichiometry whereby MAT I–V curve recording was applied with OCV cleaning.[87] Thus, typical I–V curves[88] were recorded at normal conditions (68° C) which was realized with tempered channels through anode and cathode using a Pt100 resistance thermometer. The standard deviation of the temperature control was less than 0.2° C. Further on, reaction gases were precisely tempered and humidified before entering the measuring cell. The standardized volume flow is controlled by an EL–Flow–Mass flow controller (Bronkhorst Deutschland Nord GmbH). Thereby, the gas inlet and outlet pressures were recorded while the output pressure was controlled. The maximal pressure difference at the cathode was 0.05 bar. Current or voltage regulation was performed by an electrical load. Atmosphere control (temperature and humidity) was tracked by the installed regulation of the cleanroom where the test station was installed.[39] A similar and simplified schematic of the test station as well as typical polarization (I–V) curves can be found respectively in Fig. 6 and Fig. 1 of the US patent 2006/0051628 A1.[88]

Sample preparation used a mounting bracket in order to manufacture comparable MEAs. Therefore, the CCM and the corresponding GDLs were cut rectangular, overlaid, and laminated with a plastic frame in order to hinder displacement. MEA performance evaluation started with a conditioning phase, followed by current density recording at 100 mV and 650 mV. Furthermore, comparable cell voltages (MAT and CAT) were recorded at 1.7 A/cm² at normal conditions (68° C, 100 % RH) and hot conditions (80° C, 50 % RH), respectively.

5 RESULTS AND DISCUSSION

5.1 Descriptive analysis of cathodic electrode production

PEMFC cathodes contain two solid components of which each has a specific function: the catalyst itself driving the electrochemical reaction in order to convert chemical energy into electricity and the ionomer coating the catalyst particles creating a proton conducting network within the electrode. In order to understand the electrode formation process with respect to the individual component relevance, the manufacturing process of cathodic PEMFC electrodes is investigated. The subsequent analysis provides a detailed focus on the products ranging from the initial catalyst dispersion over the electrode to the membrane electrode assembly (MEA). This work focuses on cathodic electrodes and their specific requirements for the electrode's microstructure.

5.1.1 Size reduction process of catalytic ink for cathodic catalyst layers

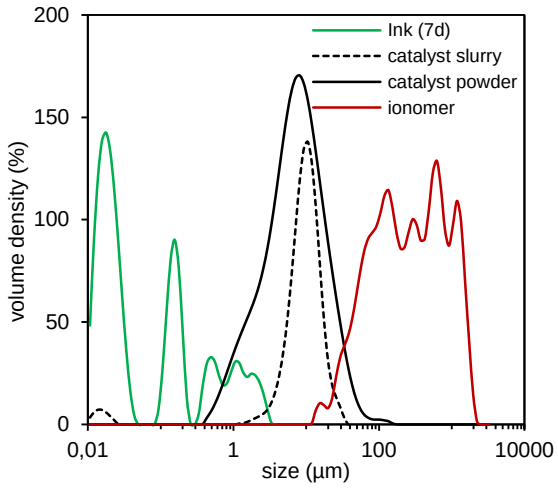

Fig. 5.1 Particle size distribution of raw materials and catalyst ink after 7 days of mixing obtained from static light scattering (SLS) experiments.

Catalyst dispersions (inks) contain catalyst powder and ionomer as main solids. For ideal catalyst utilization the overall catalyst surface should be increased. Thus, particle size reduction and appropriate particle stabilization is crucially required with respect to the fact that small particles having high surface energies are driven by surface energy minimization and tending therefore to agglomeration. Fig. 5.1 illustrates particle size distributions of the solid materials (catalyst powder and ionomer) ranging from 1 µm to 300 µm sizes. The catalytic ink finally contains the solids including an additional solvent system in order to merge the components which are further processed so that after seven days of mixing the resulting particle size distribution obtained by static light scattering technique is smaller than 2 µm. A deep dive into the particle size distribution evolution of the catalytic ink allows assumptions regarding evolving processes (Fig. 5.2, A): during the first hour of mixing particle sizes do not significantly change. Only after two process hours a detectable decrease in particle size distribution width and the median distribution value, Dv(50), from initial 2.82 µm to 1.29 µm is observed. After 24 hours mixing time the Dv(50) is further reduced by 87 % from 0.90 µm to 0.12 µm while its minimum is achieved after 48 hours of mixing (0.03 µm). The 10 %-decile (Dv10) of the particle size distribution remains unchanged during the size reduction process with an average size close to 0.01 µm. Thus, the highest variation within the particle size distribution is depicted by consideration of the 90 %-decile (Dv90): the initial value of 10.54 µm decreases to 1.08 µm within 168 hours (7d) of mixing which equals a size reduction of 90 %. It should be noted that even after 48 hours a size reduction of 90 % has taken place. Hence, the last 120 hours of mixing may not be necessary due to an ideal equilibrium state determination between polymeric

aggregation and breakage.[89] Concluding, the size reduction process has a main influence on particle size distribution width associated with the Dv50 and Dv90 values, which indicates a superior agglomerate/aggregate crushing and an overall homogenization of catalyst dispersion.

Furthermore, the relative amount for small particles (< 0.3 µm) can be used as indication for the effectiveness of the size reduction process. In contrast to the Dv50 and Dv90 values, the relative amount show further increase of 4 % from 48 hours (2d) mixing onwards (Fig. 5.2, B). Thus, the mixing process may not be terminated after 168 hours (7d) process time. It could be expected that a process extension lead to slightly smaller particle size distributions which is not feasible for manufacturing processes whereas efficiency is a key parameter with respect to time and costs. Furthermore, the applied energy input as well as the amount of ionomer dispersion could be adapted in order to generate smaller particles. As mentioned before, the main particle size reduction takes places within the first two mixing days: the initial amount of 0.3 % small particles is increased to 6 % after the first process day, followed by a further increase to 14 % after 2 days of mixing. Concluding, the relative amount of small particles is more sensitive than the characteristics from the boxplot diagram due to incorporation of the volume density for depicted particle sizes.

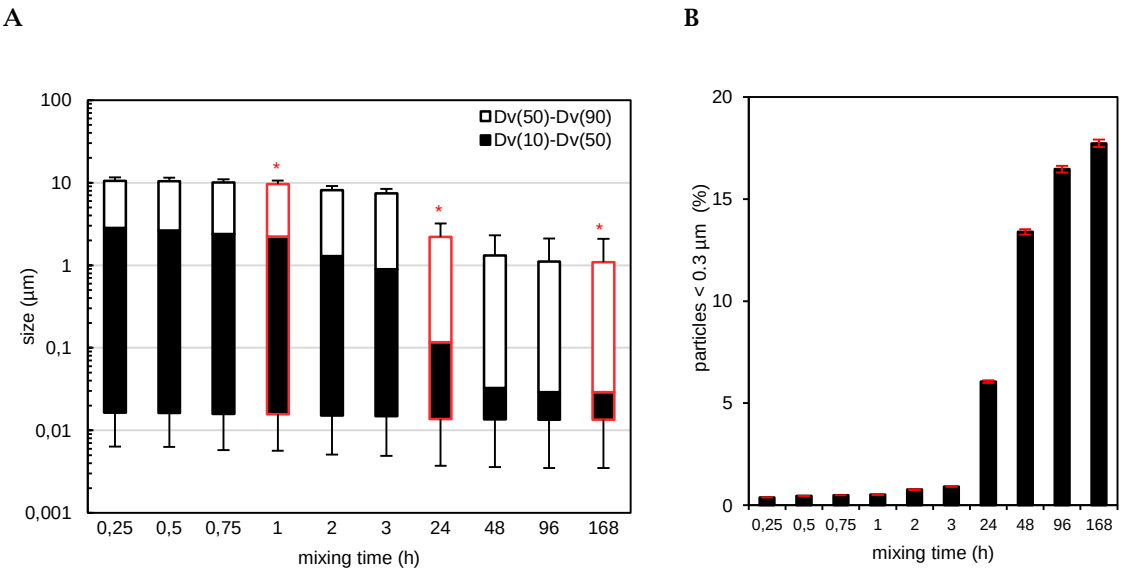

Fig. 5.2 Evolution of particle size distributions (**A**) and the relative amount of particles smaller 0.3 µm (**B**) during mixing time. Highlighted samples (*, 1h, 1d, and 7d) are used for electrode preparation and further characterization.

Catalytic inks contain a polymeric component – the ionomer – which is responsible for particle stabilization and network development. These microclusters can be analyzed by size and internal structure using static light scattering (SLS) when ranging within the micrometer scale. It is literature-known that colloidal aggregates are self-similar objects, obeying the fractal geometry.[64,67] This means that their mass scales individually with their size following a certain power law, with a scaling exponent referred to as fractal dimension, D*f* as an indication how compact the internal structure is.[51,66,67,90] Thus, the fractal dimension can be obtained from the linear region of the double logarithmic plot I(q) versus Q (chapter 4.1.1). Fig. 5.3 (B) illustrates the resulting D*f* values: the ionomer dispersion with a fractal dimension larger than 2, the catalytic ink group 1 with a D*f* value greater than 1 (starting time point until 1h of mixing) and the catalytic ink group 2 presenting D*f* values below 1 (mixing times greater than 1d). Concluding, the targeted D*f* value less than 1, resulting well dispersed catalyst inks, are derived after a process time greater than 1 day. The previous assumption of mixing time reduction due to constant particle size distributions after 48 hours processing could be further substantiated with the internal structure analysis: after two days of mixing the aggregate structure does not change significantly which indicates a completed catalyst coating or at least achievement of the equilibrium state between ionomer aggrega-

tion and breakage. Thus, the detected increase in relative small particle amount does not play a key role for the overall internal aggregate structure.

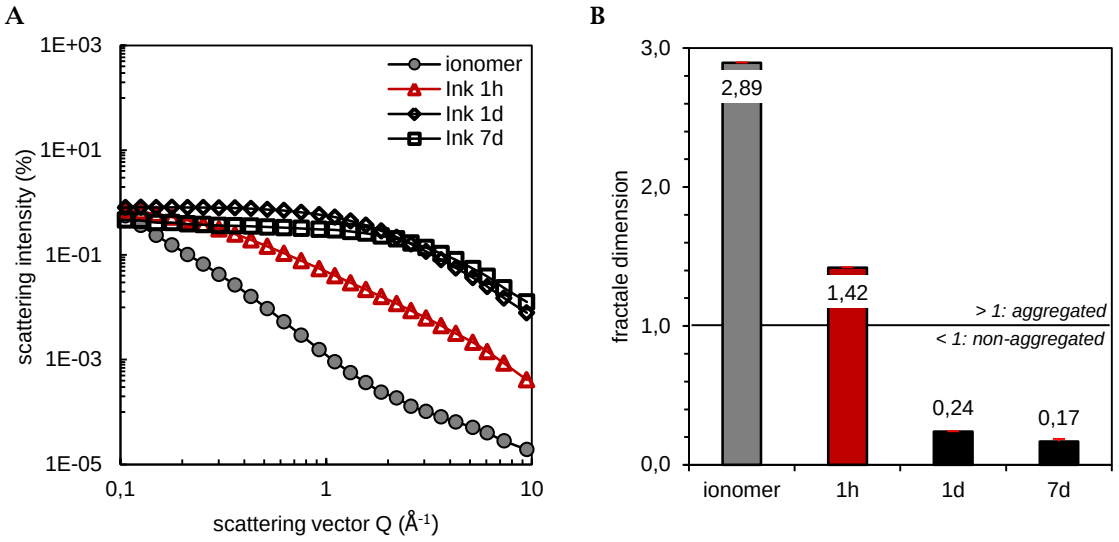

Fig. 5.3 Microcluster analysis of the internal dispersion structure of three different catalyst inks and one ionomer dispersion. (**A**) show the double logarithmic plot I(q) versus Q and (**B**) the corresponding D*f* values.

It should be noted that during the mixing process two actions proceed simultaneously: the particle size reduction where energy input is the main driving force and particle stabilization which is competing with the agglomeration process. An ideal manufactured catalytic ink has precisely adjusted particle sizes (for high catalyst utilization) including an appropriate stabilizer ratio in order to prevent agglomeration and build an interconnected network, respectively. Regarding the equal values for particle sizes and internal structure after 48 hours of mixing it could be assumed that there is a lack of energy and/or stabilizer. Against the background of electrode microstructure and its specific requirements for fuel cell functionality the influence of the catalytic ink properties, especially their particle size distribution and internal aggregate structure, should be subsequently investigated by an extensive electrode characterization.

From the manufacturing perspective the intermediate product – the catalytic ink – must meet the criteria to guarantee suitability to the subsequent coating process which includes dispersion stability and a fluid-like appearance. A specific process window must be overcome where the dispersion state should not change. Every variation in particle size distribution or aggregate state will influence the layer formation and therefore affect the electrode's microstructure which is directly connected to its functionality. Based on these manufacturing requirements, additional analytical centrifugation experiments were carried out. Typical separation kinetic profiles are illustrated in Fig. 5.4 (A): As expected the catalyst slurry immediately sediment due to the absence of stabilizing ionomer. The catalyst inks could be categorized into the previous identified groups: group 1 contains the dispersion with a mixing time less than 1 hour whereas group 2 includes dispersions processed longer than 1 day. Consideration of the supplementing particle size distribution diagram (Fig. 5.4, B) confirm the assumption of direct sedimentation of the catalyst slurry due to the presence of large particles (~10 µm) and the absence of any stabilizer. The catalyst ink processed for 1 hour equals the catalyst slurry with the deviation of smaller particles (<0.3 µm) representing the supernatant. Larger particles (>1 µm) tend to sediment earlier, resulting in a first separation boundary at 1.2 minutes, followed by a second boundary at 3.4 minutes. Thus, all catalytic inks show two separation boundaries matching their particle size distributions which could be divided into three main fractions: particles smaller than 0.03 µm (primary particles), aggregates with averaged diameters in between 0.1 and 0.3 µm (here still denoted as small particles) and agglomerates with diameters larger than 0.3 µm.

A **B**

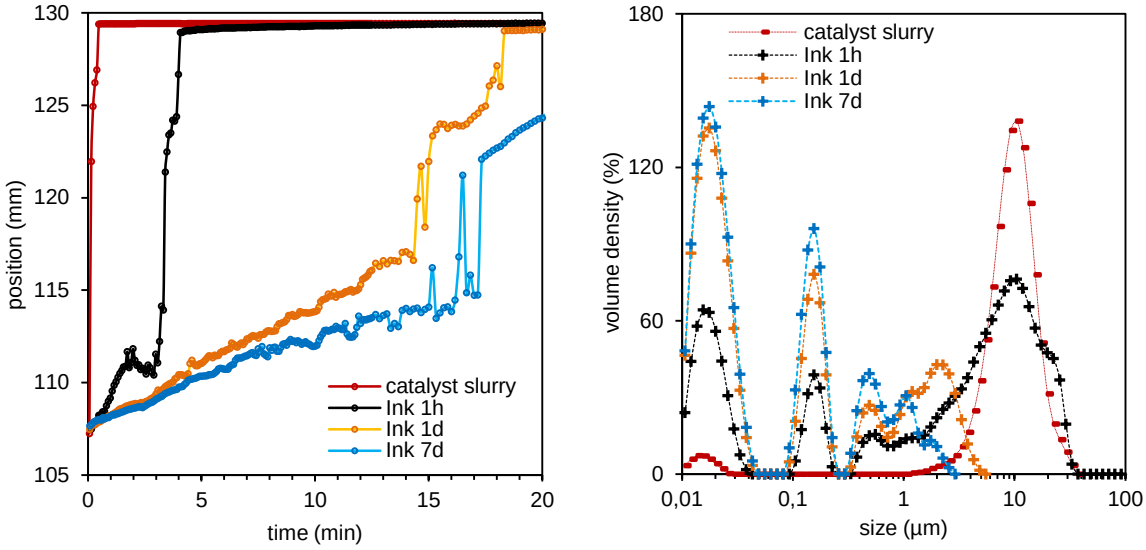

Fig. 5.4 Separation kinetics determined from analytical centrifugation at 2300 g (**A**) and particle size distribution diagram obtained from SLS (**B**) for catalyst slurry and catalyst dispersions with different mixing times.

Regarding the sedimentation velocities in Table 5.1 it is clear that the mixing process reduce the overall particle size distribution with superior agglomerate crushing. Thus, sedimentation velocities decrease with increased mixing time yielding a sedimentation velocity for a seven day processed ink of ~10.59 µm/s at 2325 g which simulates 60 days at earth gravitation and a real-time sedimentation velocity of ~0.005 µm/s. Concluding, catalytic dispersions with mixing times greater than 1 day (group 2) could be indicated as stable and therefore used within the manufacturing process.

Table 5.1 Separation boundary and sedimentation velocity obtained from analytical centrifugation analysis of 0.01 % concentrated dispersion at 22° C for 20.8 minutes at 2300 g. Sedimentation velocities were obtained at 15 % transmission. Linear dependency between relative centrifugal force (RCF) and sedimentation velocity was examined before accelerated v_{sed} was transformed into v_{sed} at gravity.

sample	**Separation boundary (min)**	**v_{sed} (µm/s) at 2325 g**	v_{sed} (µm/s) at gravity
slurry	0.1	129.30 ± 0.05	0.055
1h	1.2 3.4	28.21 ± 0.62	0.012
1d	14.8 17.9	14.95 ± 0.55	0.006
7d	15.2 16.5	10.59 ± 0.31	0.005

5.1.1.1 Summary catalytic ink analysis

Catalytic inks were characterized in order to gain particle size distributions of used raw materials such as catalyst powder and ionomer solution. A wet grinding process is the method of choice for material merging and overall size reduction of the solid materials. Thus, static light scattering (SLS) and analytical centrifugation (AC) were used for particle size, internal structure, and dispersion stability analysis. Particle size distribution and the internal structure are crucial dispersions characteristics which predominantly influence the film formation and therefore determine the electrode's microstructure and functionality whereas the dispersion stability must overcome the process window requirements regarding the manufacturing time. In general, the typical mixing time of catalyst dispersions take seven process days (168 h). In order to evaluate the particle size distribution evolution within this process three time points (1h, 1d, and 7d) were picked and extensively analyzed (Fig. 5.5). Considering the particle size distribution, the Dv(90) value shrinks from 9.58 µm (1h mixing) to 1.08 µm (7d mixing) which equals a size reduction of 90 %. Even after 1d of mixing the Dv(90) was reduced by 80 % to 2.21 µm indicating a rapid deagglomeration process. It could be assumed that further particle size reduction is not supported due to a lack of stabilizer. Thus, using the applied energy input and the specific ionomer to carbon ratio as carried out here, an equilibrium state within the catalyst dispersion is already achieved after a mixing time of 1d. The internal structure analysis underlines these findings: only the 1h sample shows an aggregated structure with a fractal dimension of 1.04 whereas the 1d and 7d samples present non-aggregated behavior indicated by D*f* values of 0.31 and 0.13, respectively. Furthermore, analytical centrifugation results complete the picture so that the three analyzed samples could be categorized into two groups: group 1 (coarse dispersion) containing the 1h mixed sample yielding inhomogeneous and instable catalyst dispersion whereas group 2 (fine dispersion) represents homogeneous and stable dispersions which meet the manufacturing requirements of fluid-like appearance, high stability and structure resistance to shear force application. Fig. 5.5 illustrates the experimental particle size data and their estimated impact on the catalyst layer structure which is subsequently investigated.

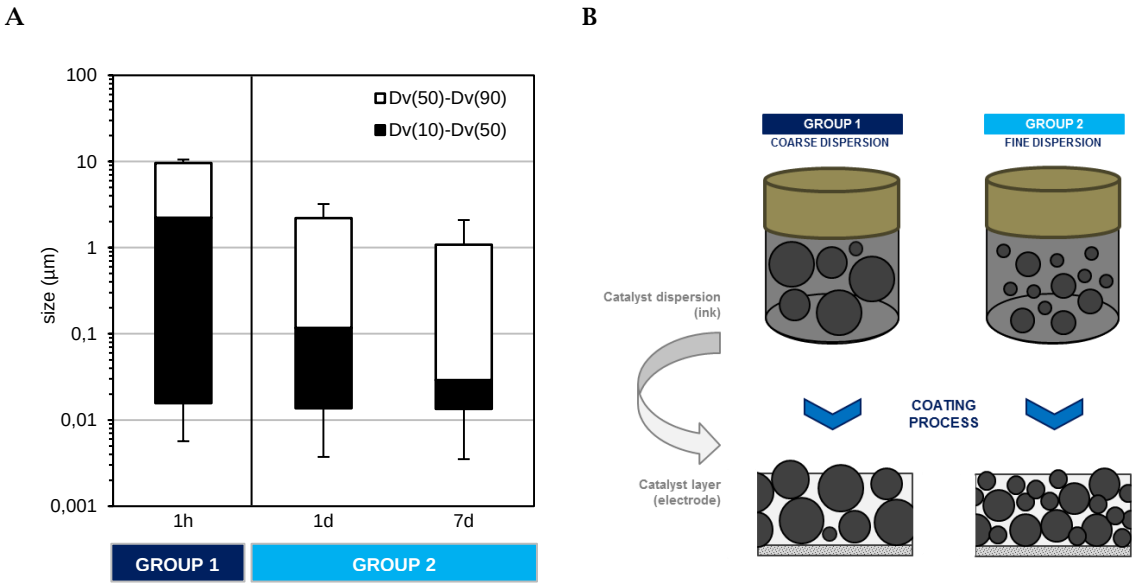

Fig. 5.5 Experimental particle size distribution data (**A**) and model description (**B**) of categorized groups.

5.1.2 Determining the electrode´s microstructure by morphological analysis

The cathodic electrode microstructure should be investigated regarding surface appearance, cross–sectional observation, and specific surface area as well as pore size distribution. Preliminary sample categorization should be proven and the hypothesized correlation between catalytic ink particle size distribution and microstructure determination should be further examined. Although the 1h sample was identified as unsuitable for the coating process it is included within the subsequent characterization in order to reveal the prior assumption.

5.1.2.1 Surface analysis of cathodic electrodes

Laser confocal microscopy allows 3D visualization of electrode's surface. Fig. 5.6 (B) illustrates surface appearances obtained from catalyst inks which were coated after mixing for 1h, 1d, and 7d. The group 2 samples show similar surface conditions of continuous layer with less or crack–free area (blue spots) and an overall smoothness confirmed by low surface roughness of 0.42 µm and 0.27 µm, respectively. In contrast, the 1h sample is characterized by a cracky appearance (~5.4 % crack area) and high surface roughness of 1.55 µm. Additional nanoCT images (Fig. 5.6, C) verify the laser confocal microscopy results: cracky appearance (~15 %) of the 1h sample and continuous layers for 1d and 7d samples with crack areas of 0.5 % and 0 %. The discrepancy between the calculated crack area of the 1h sample using laser confocal microscopy and nanoCT imaging are most probably due to image artefacts such as reflections initiated by specimen's thermal sensitivity and its associated curvature which could be clearly identified at the upper and lower picture edges. Moreover, the specimen movement during image capturing is also responsible for resolution losses as achieved for the 7d sample. Thus, nanoCT imaging should not be applied as default characterization method even though the investigation area of 2.0×10^{-2} cm² is much larger than the typical laser confocal microscopy area of 5.6×10^{-4} cm². Contrary, the calculated crack area of the 1d probe shows very good agreement between the two methods and results ~0.5 % in both cases. Further SEM examinations (Fig. 5.6, D) yielded an overall averaged particle diameter for all three samples of ~80 nm. The primary catalyst particle shape is not altered during mixing procedure so that their catalytic functionality should not be influenced. Thus, the applied energy is suitable in order to grind the agglomerates and simultaneously keep the existing morphology. In contrast to the SLS technique SEM analysis yields "primary" catalyst particles sizes whereas the SLS technique display the overall particle size distribution focused on agglomerate sizes. The combination of both methods allows assumption regarding the initial and coated solid component structure. Furthermore, the SEM surface images validate the prior sample grouping with respect to large cracks and inhomogeneous film for the 1h sample while the group 2 samples show similar surface appearance.

As demonstrated the applied characterization techniques (Fig. 5.6, B–D) gained two electrode types differentiating in surface appearance including surface roughness, crack area, and film homogeneity. Those results follow the previous postulated correlation between catalyst ink properties and their resulting electrode structure. The model description deduced from the ink characterization reflects the surface analysis findings in good agreement (Fig. 5.6, A).

Transmitted light photography (TLP) is the single method which considerable shows differences between all three samples. Fig. 5.6 (E) illustrates the detected transmission: the 1h sample is overexposed due to a high number of cracks, whereas the 1d sample presents more light spots than sample 7d. Even though the group 2 electrodes (1d, 7d) show similar surface appearance their internal microstructure are expected to differ. Their catalytic ink particle distribution equally indicates small differences underlined by a 4 % increased relative amount of small particles. It is feasible, that the detected light spots depict void space between agglomerates. Thus, it could be assumed that the main void size of 10 pixels equals approximately 200 µm with the notice of inconsistencies due to light reflection errors. Nevertheless, there is an obvious gap between sample 1d and 7d. The slight changes within the ink particle size distribution especially the increase in small particles could be responsible for a void space filling which leads to a higher packing density and thus creating less detectable light spots. Hence, two feasible scenarios should be proven: First, the progressive particle size reduction leading to void space filling or second

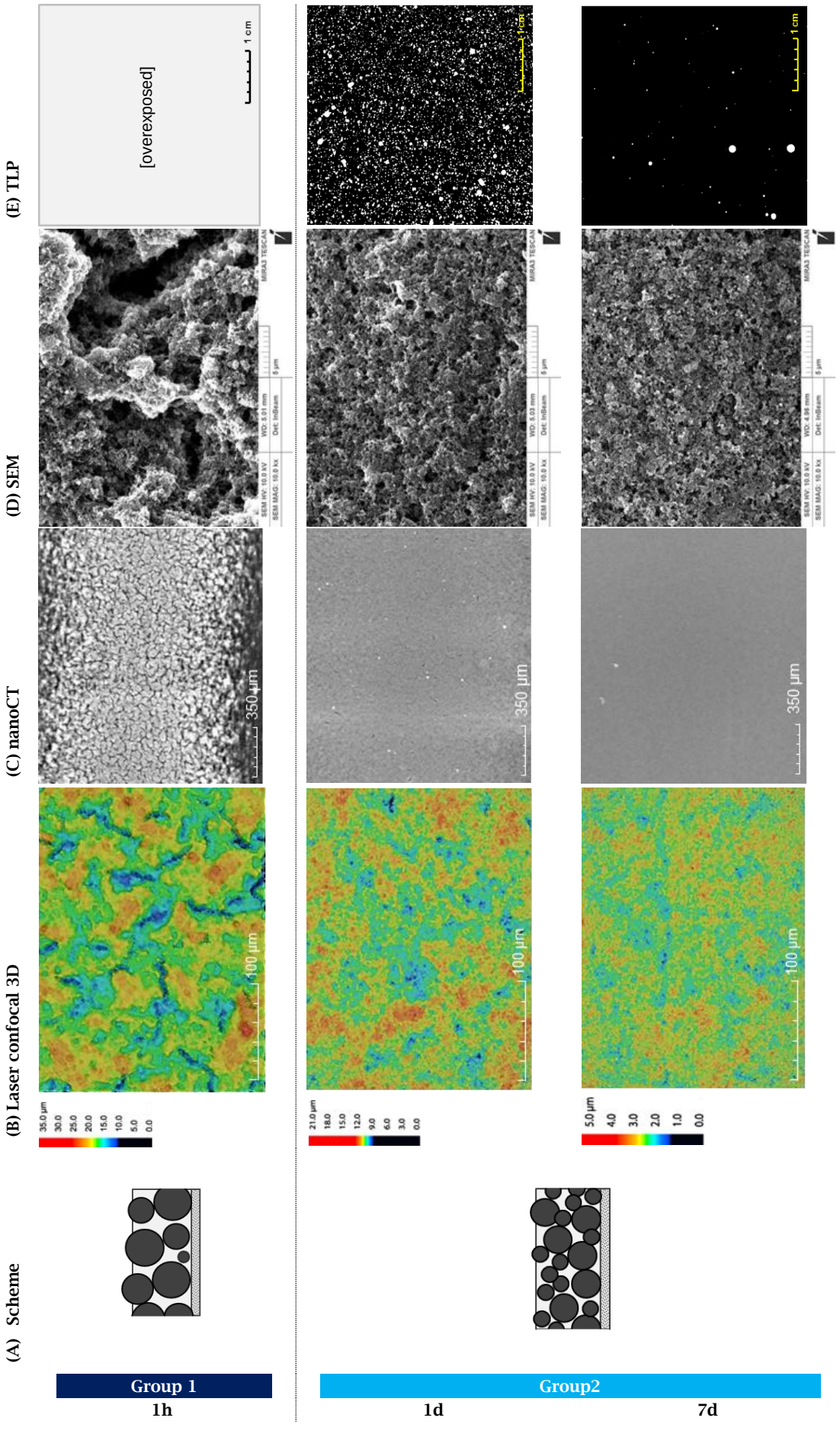

Fig. 5.6 Surface analysis results obtained from diverse techniques: model description (**A**), laser confocal 3D (**B**), nanoCT (**C**), and SEM images (**D**), and binary images of transmitted light photography (**E**) of electrodes coated from 1h, 1d, and 7d processed catalytic inks. The 1h probe of (**E**) is overexposed due to its high void area.

a thicker ionomer coating of the catalyst particles resulting a better connected ionomer network and less void space (Fig. 5.7). The prior investigations suggest considering scenario 1 as realistic objective. Scenario 2 should still be further examined but facing simultaneously the difficulty of ionomer imaging. Thus, additional cross-sectional SEM investigation including EDX elemental mapping should give further insights.

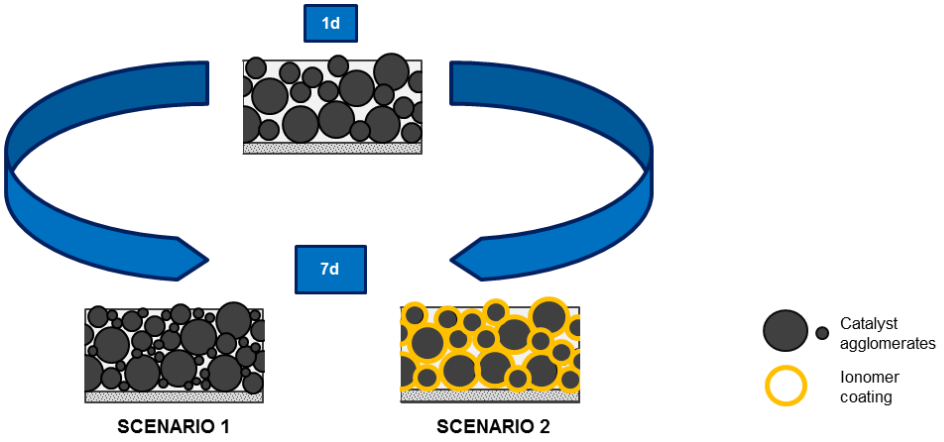

Fig. 5.7 Model description for feasible electrode scenarios resulting from ink mixing processes: void space filling with occurring small particles (1) or ionomer coating thickening (2).

5.1.2.2 Cross-sectional cathode characterization

Cross-sectional electrode analysis completes the previous presented picture of sample grouping into specimens terminating the mixing procedure before or after 1d duration. Electrode's thickness decrease with increasing mixing time which precisely equal a decrease of initial ~21 µm for group 1 to final ~9 µm thickness for group 2 samples (Fig. 5.8, A). Prior surface analysis corresponds with these findings with respect to smoother surface roughness for electrodes obtained from longer proceeded catalytic inks. Furthermore, a slight thickness decrease (1 µm) within group 2 samples confirm scenario 1 with respect to an increased volume density of small particles leading to void space filling in between catalyst agglomerates. Considering the electrode porosity, it is obvious that the group 1 sample demonstrate larger pores and material inhomogeneity due to a short mixing time of 1h duration. In contrast, the group 2 samples show smaller pore widths and similar pore distribution, as well as material homogeneity. The elemental mapping for platinum confirms large accumulation for the 1h sample electrode whereas homogeneous distribution is found for the group 2 samples (Fig. 5.8, B). All samples are loaded with 0.25 mg/cm² platinum each, verified by XRF measurements. Moreover, the elemental fluorine EDX analysis reveals substrate-sided fluorine accumulation for all samples which also could possibly related to measurement artefacts (Fig. 5.8, C). Thus, an ionomer concentration gradient is expected top-downwards which would interfere with ideal cell behavior presuming homogeneous material distribution. Feasible candidates causing this inhomogeneity can be identified as film drying process issues meaning precisely the catalyst dispersion viscosity which influences the mass transport and diffusion processes during electrode drying or the deployed solvent system leading also to complex evaporation processes. Hence, further evidence for scenario 2 could not be found due to a lack in resolution owed to the characterization technique.

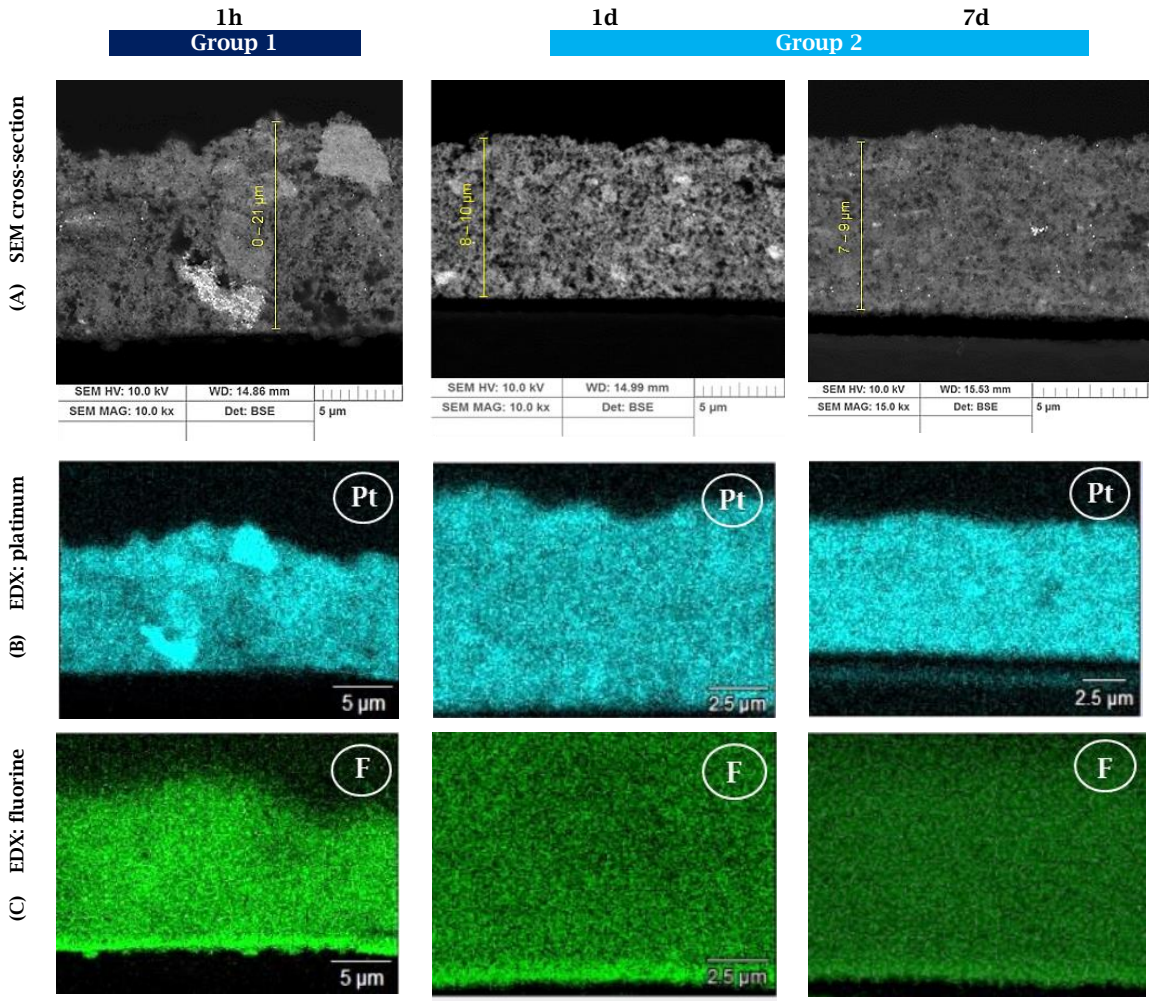

Fig. 5.8 Electrode lateral view images achieved from SEM cross-sectional imaging of coated electrodes from different time points of the mixing procedure: 1h, 1d, and 7d (**A**). Elemental mapping illustrates platinum (**B**) and fluorine (**C**) distribution. All electrodes are loaded with ~0.25 mg/cm² platinum.

5.1.2.3 Micropore analysis by gas sorption

The typical nitrogen adsorption–desorption cycles of a common fuel cell catalyst powder and the manufactured catalyst layers are illustrated in Fig. 5.9 (A). According to the International Union of Pure and Applied Chemistry (IUPAC) classification for sorption isotherms, the depicted sorption shapes follow type IV isotherms which characterize mesoporous materials and allow application of the BET method, diverse pore size distribution analysis methods, and pore volume determination.[59] The beginning of the sorption curve within the low partial pressure range indicates a monolayer–multilayer adsorption followed by the main characteristic of type IV isotherms, the hysteresis loop which is associated with the occurrence of pore condensation. Limited adsorbate uptake over the range of high partial pressures could be correlated to a complete pore filling. Considering the hysteresis loops, further IUPAC classification yields two types: H3 type, representing the catalyst powder and possibly the 1h electrode and H2 type, illustrating electrodes obtained from longer proceeded inks (Fig. 5.9, B+C). H3 type hysteresis loops are literature-known for the absence of an upper adsorption limitation at high partial pressure and slit shaped pores which are typical for carbon supported catalyst powders – here the investigated catalyst powder isotherm is more similar to H3 than H2 hysteresis loop.[72] Manufactured catalyst layers are indicated by ionomer coated catalyst particles arranged within an interconnected ionomer network which should result in mesoporous material characteristics (hysteresis loop type H2). Thus, the 1h electrode is more catalyst-like corresponding to a previously identified unsuitable process time. As prior mentioned the short mixed catalyst ink was depicted as incapable for the manufacturing process leading to an inhomogeneous distributed electrode. Hence, those large platinum

accumulations could cause the catalyst-like sorption response of the 1h electrode sample. In contrast, the electrodes obtained from longer proceeded inks follow precisely H2 type hysteresis loops. They indicate the presence of an interconnected porous network with a wide distribution of pore sizes. Thus, network and pore blocking effects are responsible for the typical hysteresis shape which can be found in Fig. 5.9 (C).[72] Using the advanced network model of Seaton et al.[91,81] the values for the mean coordination number, Z, is determined as 2.6, 2.7, and 2.8 for increased process time. Furthermore, the linear dimension, L, yields also an increase ranging from 6.3 to 8.6. Both network characteristics demonstrate an increase in network connectivity (Z) and count of micropores within a macropore (L) which meet the hypothesis of scenario 1 (Fig. 5.7). Higher pore connectivity is gained by agglomerate or aggregate crushing resulting in non-coated porous catalyst surfaces and an increased linear dimension equaling void space filling with smaller particles. Scenario 2, ionomer coating thickening is expected to decrease the pore network connectivity which support scenario 1 as realistic objective.

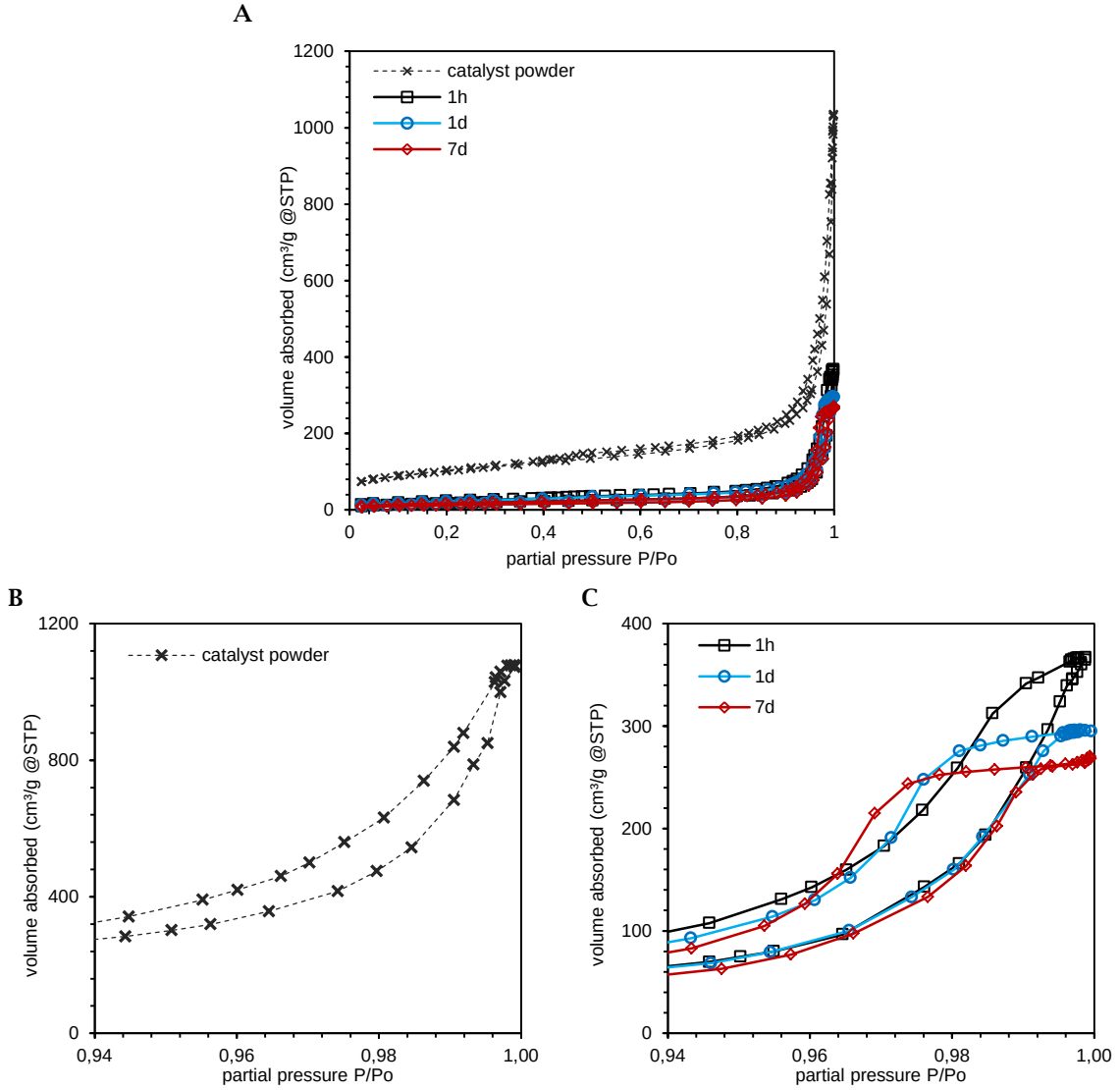

Fig. 5.9 Nitrogen sorption isotherms of catalyst powder and electrodes on decal film coated after different ink mixing times (**A**). (**B**) and (**C**) illustrate their typical hysteresis loops according to IUPAC classified as H3 like and H2 type, respectively.[92]

The recorded Nitrogen sorption data in between 0.05– 0.3 P/P_0 was further analyzed using the Micropore BET Assistant offered by the instrument's software. Due to the presence of micro–, meso– and macropores at least two different pore analysis models should be applied. The classical macroscopic, thermo–dynamic concept is linked to pore condensation phenomena which often fail to describe pore filling of micropores and even narrow mesopores.[92] A more realistic picture can be obtained by applying a Density Functional Theory (DFT) which is based on statistical calculations.[76] Especially the Quenched Solid State DFT (QSDFT) model is designed for carbon materials with heterogeneous surfaces.[75] Thus, these two approaches are focused with the goal of deducing a complete and precise description over the range of micro– to macropores.

In general, the catalyst carbon support defines the porosity of the solid components and therefore the overall specific surface area of the cathodic electrodes. The initial Pt/C–catalyst BET surface area of ~360 m^2/g would theoretically lead to an electrode BET surface area of ~216 m^2/g with respect to a catalyst loading of 60 % per g electrode. This value could not be reproduced with the as–synthesized electrodes due to the addition of ionomer which coats the catalyst particles and leads to an overall pore decrease (Fig. 5.10). Comparing the MBET SA to the total QSDFT SA of the catalyst powder, no significant differences can be found (Fig. 5.10, A). The coincidence is owed to the catalyst microstructure containing mostly micro– and narrow mesopores which means that both models are able to present precise results. Regarding the micropore SA, the QSDFT model is slightly higher and theoretically more precise than the t–method postulated by de Boer.[93] Regarding the manufactured electrodes, the differences between the classical (BET, de Boer) and the statistical (QSDFT) models are significant and about approximately 22% for each type of electrode (Fig. 5.10, B). This gap can be explained with the diverse pore width covered by the models: the QSDFT concept ignores macropores which are included within the classical approach. Thus, the diverse results cannot be interpreted separated from each other but supplementary. As noted above, micropore SAs should be used from QSDFT calculation due to its high accuracy. Additionally, the QSDFT model covers pore widths of 0.4 – 35 nm, so that also mesopore SAs can be obtained from QSDFT calculation. The gap between total QSDFT SA and MBET SA can be interpreted as macropore SA.

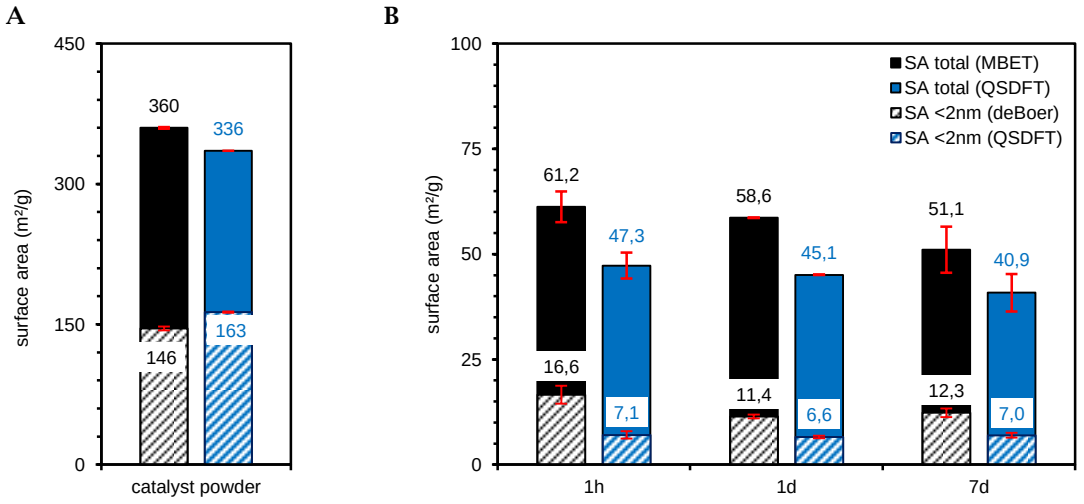

Fig. 5.10 BET surface area for a common fuel cell catalyst powder (**A**) and coated electrodes after different ink mixing times (**B**).

Regarding the manufacturing time (1h, 1d, and 7d) for the three specific electrodes, following results can be found: the micropore QSDFT SA stays constant over time with ~7.0 m^2/g for all three electrode types whereas the QSDFT and MBET total SA slightly decrease by approximately 14 % and 17 %, respectively (1h to 7d, s. Fig. 5.10, B). Due to the fact, that also the difference between the MBET and QSDFT total SA became smaller over time, a primary macropore loss can be hypothesized. Taking additionally the pore volume results into account, the previously drawn picture can be underlined: the micropore volume results stay constant for the three types of electrode over time for both de Boer and QSDFT method with ~0.005 cm^3/g (Fig. 5.11, B). Here, even the total QSDFT pore volume which can be interpreted as total micro– and mesopore volume stays

constant for progressive manufacturing time. This leads to the assumption that the decrease in the total pore volume over time can be linked to a primary loss of macropores (Fig. 5.11, B). However, these results fit into the previously drawn model for particle grinding process over time which postulated a void space filling so that the particle packing density increase and the electrode's porosity decrease.

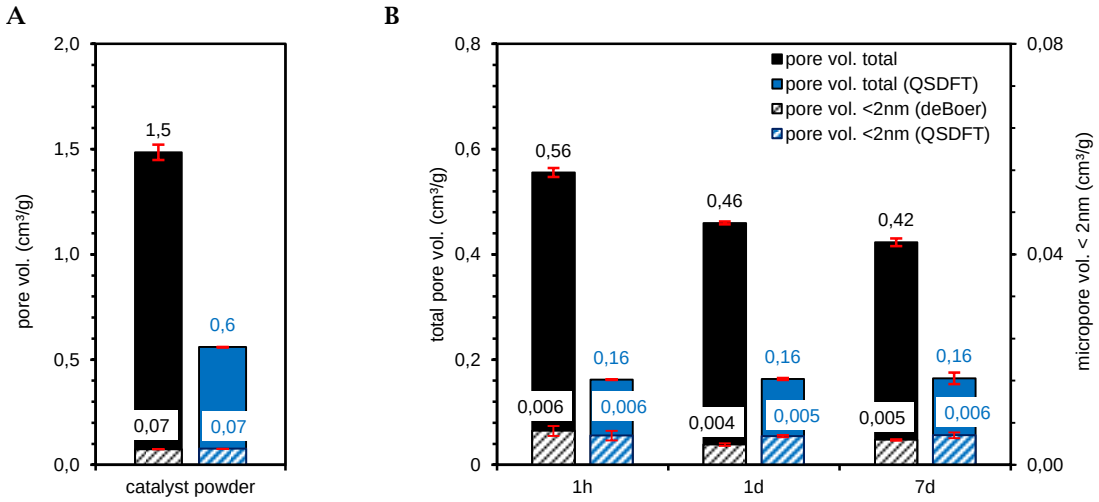

Fig. 5.11 Illustration of the total pore volume for the catalyst powder (**A**) and the investigated catalyst layers obtained from classical macroscopic and statistical models (**B**).

Applying the BJH model to the recorded desorption data, pore size distributions (PSD) for cathodic electrodes can be illustrated (Fig. 5.12). It is obvious that the PSDs of all manufactured electrodes follow the catalyst powder PSD since it presents the main component and therefore determines the main characteristics. However, the manufacturing process has some impact on the PSD shape: the overall PSD width is shrinking over time and shifts towards smaller pore diameters which can be linked to the particle grinding process. In general, the longer proceeded cathodic electrodes present two main peaks: one at 3.5 nm (mesopores) and a second at 75 nm or 63 nm for the 1d and 7d sample, respectively. In contrast, electrodes from shorter processing times (1h) mostly present narrow mesopores.

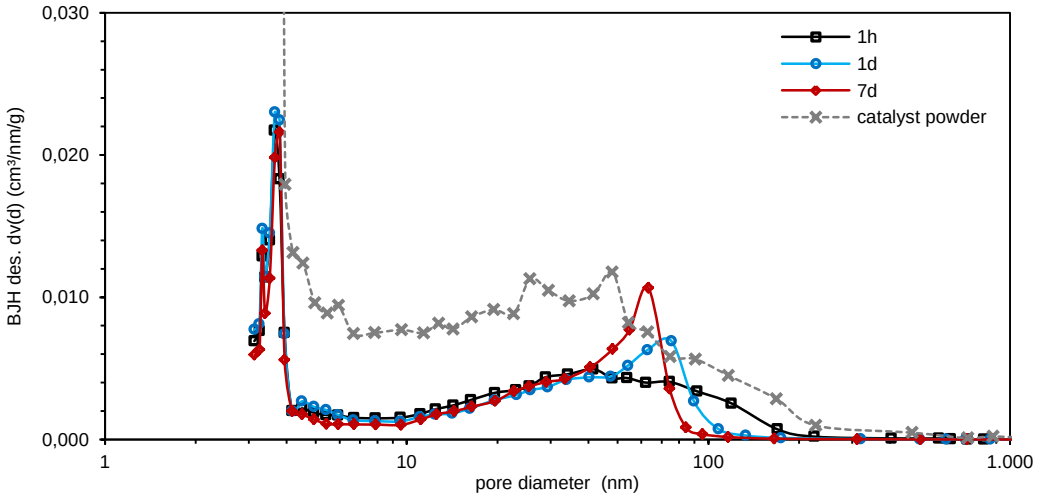

Fig. 5.12 Pore size distributions for catalyst powder and manufactured electrodes calculated from the desorption data using the BJH model.

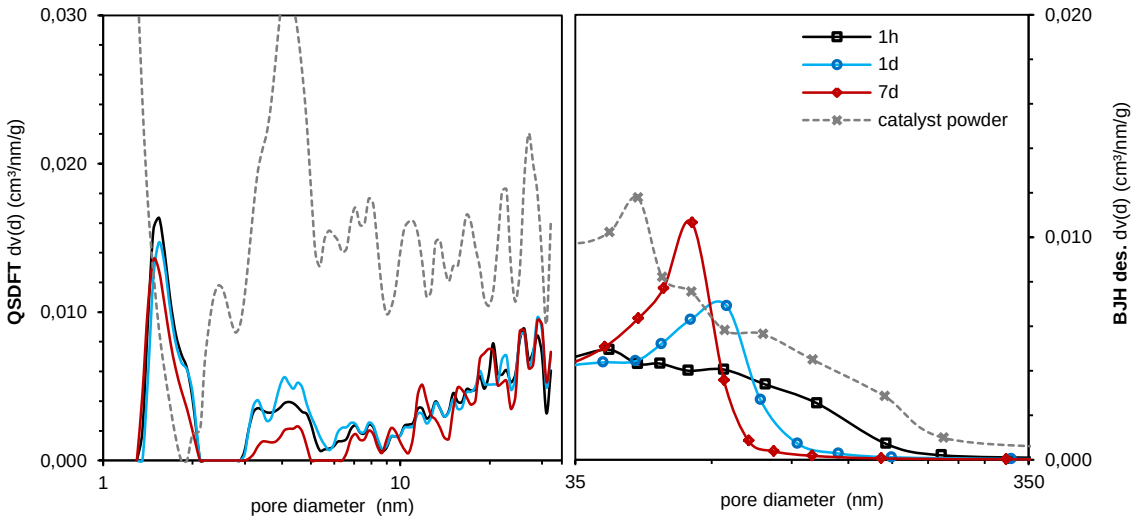

Fig. 5.13 Pore size distribution plots obtained from nitrogen physisorption data using a QSDFT model and BJH method.

In order to evaluate the micropores, an additional PSD plot obtained from the QSDFT data set is illustrated in Fig. 5.13. All three electrode types present similar PSD shapes corresponding again to the initial catalyst powder PSD. Further on, the volume fraction for pore diameters in between 3–5 nm slightly decreases for the 7d sample in comparison to the 1h and 1d sample. This can be an indicator that the catalyst dispersion grinding process is too long and important pores are lost. Literature often postulates an agglomerate structure regarding the cathodic electrode microstructure. Hence, two types of pores are identified: primary pores inside the agglomerates containing catalyst particles surrounded by an ionomer film and secondary pores between those agglomerates.[46,17] With respect to the electrode functionality both types are crucial for high cell performances. Especially the secondary pores play a key role for gas transport so that the pore width should guarantee reactant transport. Summarizing the experimental data, the 7d sample is expected to yield higher cell performances compared to the 1h sample due to its optimized pore size structure containing a high fraction of mesopores for gaseous transport while maintaining micropores for high catalyst utilization. The 1d sample shows similar pore structure so that comparable performances should be obtained.

5.1.3 Electrochemical component testing

Fig. 5.14 show polarization curves comparing the performance of three different electrode designs obtained from diverse processed catalytic inks. The preliminary sample categorization with respect to their microstructural differences could be further validated. Group 1 (1h) indicates lower cell performances at high current densities whereas no significant differences between the group 2 samples had been achieved. The two groups clearly differentiate within their microstructure regarding the pore size distribution: group 1 presents a low fraction of macropores and inhomogeneous film formation while group 2 samples (1d, 7d) are indicated by main fractions of micro- and macropores simultaneously. This type of cathodic electrode, containing both micro- and macropores, is optimizes for fuel cell operation where micropores are necessary for catalyst utilization and macropores crucially needed for mass transport (O_2, H_2O). Further on, the studies of Akabori et al. and Secanell et al. estimated the overall surface area of catalyst particles as the main effective influential parameter regarding cell performances. This means that a decrease in agglomerate size would lead to diminished surface area per agglomerate but simultaneously increase the amount of agglomerates so that the total surface area is increased.[28,49] Hence, Akabori's explanations can be partially confirmed with these experimental findings: longer proceeded catalytic inks yield smaller sized catalyst particles equaling an increase in the overall surface area but

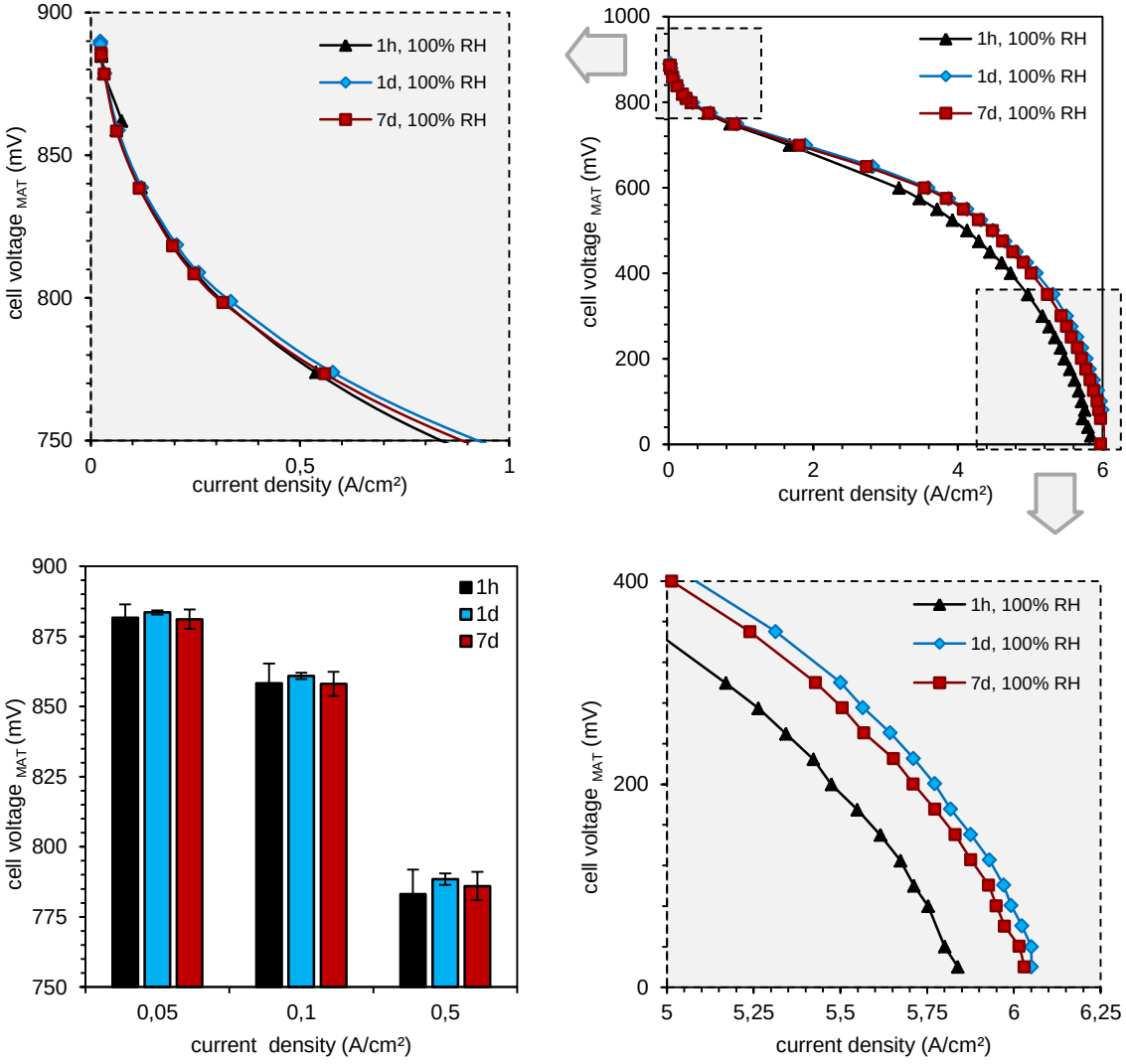

Fig. 5.14 MAT polarization curves obtained from applied voltages in the range of 0–1 V (top right). Current densities were recorded at 68° C at 100 % RH (=NOC). Additional OCV cleaning was performed in between the measurement points. Zoom 1 (top left) illustrate the kinetic area including the corresponding cell voltages at 0.05, 0.1, and 0.5 A/cm² whereas zoom 2 (bottom right) depict the mass transport area.

simultaneously smaller particles lead to a loss in secondary pores (macropores) creating higher electrode packing densities. Thus, small sized pore widths present shorter diffusion pathways for

reactants and ions with the concurring risk of mass transport issues. Furthermore, Khajeh-Hosseini-Dalasm et al. propose several structural characteristics as influential parameter affecting the cathode catalyst layer performance including the platinum loading, the total ionomer volume fraction, and the catalyst layer thickness.[20] While platinum (0.25 mg/cm²) and ionomer loadings (~30 %) were fixed here, the electrode thickness was reduced by 50 % during ink mixing process. Thus, it can be hypothesized that the main influential parameter for these catalyst layer performances is the pore size distribution of the cathodic electrodes. The experimental findings underline that longer proceeded electrodes present an optimized microstructure for fuel cell application.

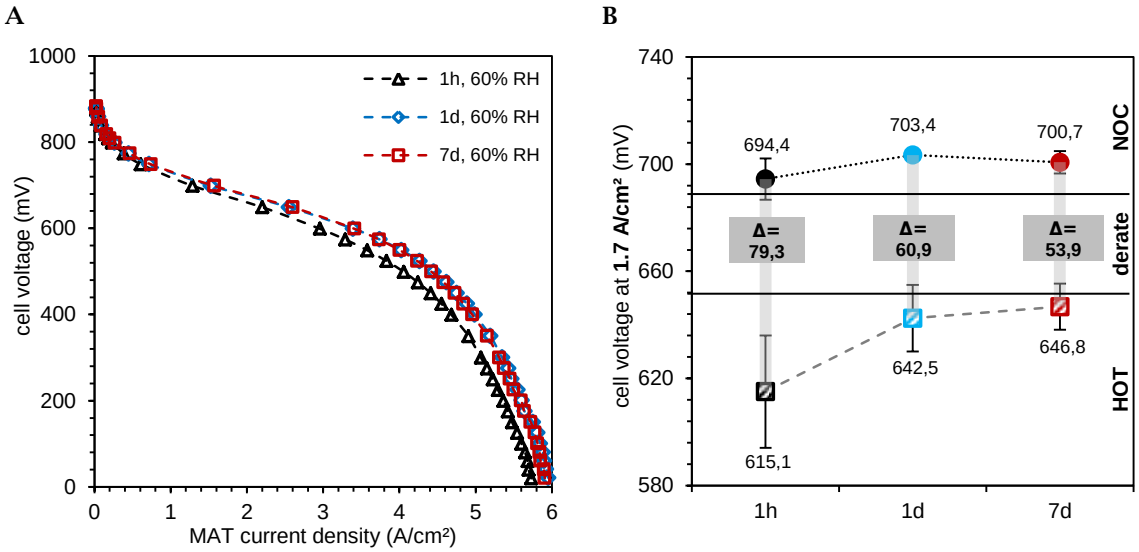

Fig. 5.15 (A) MAT polarization curve recorded with OCV cleaning at 68° C and 60 % RH. (B) steady state points recorded at 1.7 A/cm² for 68° C, 100 % RH (normal condition) and 80° C, 50 % RH (hot and dry condition) for all three electrode designs (1h, 1d, and 7d). The difference between NOC and HOT measurement points is designated as derate, Δ (mV).

When varying the relative humidity conditions during I-V curve recording, insights on the proton conductivity ability and possibly mass transport issues can be achieved. Fig. 5.15 (A) show polarization curves at dry conditions (60 % RH) which match the catalyst layer behavior during wet conditions. The overall cell performances are slightly reduced due the membrane's lower proton conductivity but especially the group differentiation already starts during low current densities resulting from diverse connected ionomer networks within the electrodes. However, dry conditions demonstrate high fraction of gaseous oxygen which reduces the overall electrode proton conductivity leading to decreased cell performances. The 1h sample's low performance correlates well with previous structural findings regarding electrode's thickness and roughness. Especially the nitrogen sorption response fitting more the catalyst powder hysteresis loop than those for typical mesoporous electrodes including the aggregated state description for the catalytic ink are strong indications for unsuitable material processing in order to meet fuel cell electrode requirements. It is obvious that the catalytically active and therefore crucial three-component-phases have not yet been sufficiently developed. Concluding, a process ink mixing time duration of 1h is not recommended.

An equal picture is drawn when the operation temperature was varied in order to demonstrate driving conditions. A temperature decrease and maintained relative humidity (100 %) reduced the reaction kinetic whereas the proton conductivity ability remains unaffected. Thus, product water participates longer within the electrode pore network which leads to mass transport issues. Fig. 5.16 (A, B) illustrates current densities at 650 mV (ohmic resistance range) and 100 mV (mass transport range) for normal (68° C) and cold (30° C) conditions. In both cases preliminary sample categorization is valid: the 1h sample demonstrates significant performance differences during both operating conditions. At both steady states (650 and 100 mV) the group 2 samples yield 10 % and 5 % higher current densities at 68° C compared to the group 1 sample, respectively. In contrast, during cold conditions the group 2 samples indicate a current density

loss of 38 % for both steady states. Thus, the 1h specimen's microstructure is likely to avoid mass transport issues corresponding to the presence of large pores and a high electrode thickness. In contrast, the reduced cell performances for group 2 are correlated to smaller pore diameters within the electrode resulting in a hindered water removal process. The results in Fig. 5.15 (B) combine temperature and relative humidity adjustment. A raised reaction kinetic and decreased proton conductivity ability (80° C, 50 % RH) lead to smaller performance losses within the group 2 samples corresponding to a well-connected ionomer network whereas the 1h sample is identified by a poor ionomer network and faces higher resistances which have to be overcome by the ions in order to drive the electrochemical reaction. The performance differences obtained from relative humidity variation in Fig. 5.15 (A) are also valid for hot operation conditions. Concluding, all investigated testing points at diverse operating conditions yield overall high performances for the group 2 samples. Thus, their microstructure indicates an ideal ionomer network distribution including well adapted pore size distribution avoiding mass transport issues.

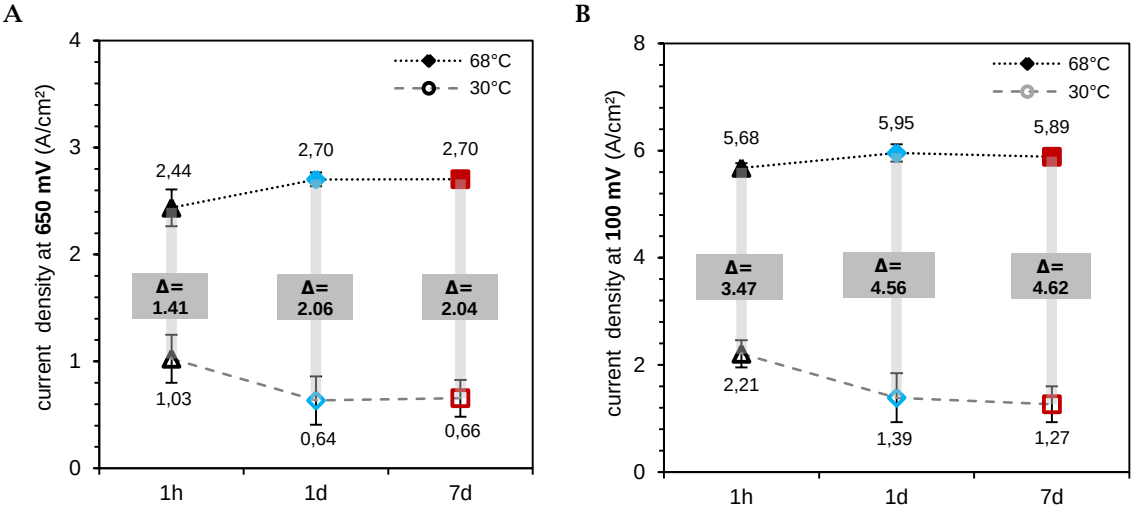

Fig. 5.16 Current densities at 650 mV (**A**) and 100 mV (**B**) recorded at 68° C and 30° C at 100 % RH, respectively, in order to obtain electrode structural insights.

Moreover, it should be noted that single cell testing should be used as a first estimation for cell behavior on stack level. A realistic stack prediction takes into account mutual influence of the single cells, gaseous flow steams, and leakage issues whereas the stack is incorporated into a testing infrastructure simulating the automotive powertrain. Thus, further electrochemical testing is strongly recommended.

5.1.4 Conclusion

PEMFC performances are mainly affected by the cathode catalyst layer performance. Thus, the understanding of the electrode's microstructure is crucially essential in order to optimize their design. In the last decade several improvements regarding manufacturing techniques, platinum utilization, and development of catalyst support materials have been developed but a complete comprehension of the complex component interaction is still lacking. Today, various computational models investigate the catalyst layer structure and its optimum component composition. They are often performed prior to time consuming and expensive experiments.[28] Literature-known concepts focus on pseudo-homogeneous film models[49,60,94], agglomerate models[21–27,47] and pore-scale models.[47,48,95] Concerning the catalyst agglomerate and aggregate diameter within the catalyst ink only a few experimental data exist although Pt nanoparticles and primary particles of the support material are well-known. Thus, model descriptions estimate agglomerate sizes or pore size distributions based on the catalyst mean diameter in dispersion. Hence, the present work fills the gap not only by catalyst dispersion state and their corresponding particle size distributions analysis but also directly correlates these characteristics to the electrode microstructure which finally determines its performance.

Static light scattering is sensitive to catalyst agglomerate and aggregate detection so that the particle size distribution process investigated here is characterized in great detail. In order to fabricate electrodes, differentiating in their microstructure, three different processed catalytic inks were selected: 1h, 1d, and 7d. The samples were further categorized into 2 groups containing large aggregates of about 10 µm diameter (1h; group 1) and smaller sized agglomerates of about 1 µm diameter (1d, 7d; group 2), respectively. Internal catalyst dispersion analysis also yielded aggregation status for the group 1 whereas the group 2 samples were well–dispersed. However, optical methods analyzing the electrode appearance followed the specimen categorization and include laser confocal microscopy, nanoCT, scanning electron microscopy, and transmitted light photography technique as well as pore size distributions obtained from BJH and QSDFT analysis of nitrogen sorption experiments. Concluding, group 1 specimen show aggregated dispersion state, leading to rough and cracky surface appearance further elaborated by inhomogeneous material distribution (platinum agglomeration), catalyst–like sorption behavior (H3 type hysteresis loop), and presence of large macropores. All these structural characteristics lead to lower cell performance compared to group 2 samples. Their initial dispersed catalyst particle size distribution show smaller sized agglomerates leading to smooth and crack–free electrode surfaces. Furthermore, the electrode material distribution is highly homogeneous yielding pore size widths corresponding to mesoporous materials. Few methods were able to detect differences between the group 2 samples: SLS particle size distribution as well as the internal catalyst dispersion analysis stated a higher fraction of smaller sized catalyst particles within the 7d sample. Merely electrode surface roughness and pore volume analysis but also void area measurements were sensitive to the sample's differences. These findings underline the importance of understanding the electrode microstructure in order to optimize the cell performance.

5.2 Does the ionomer loading influence the pore size distribution and the overall electrode microstructure characteristics?

The literature depicts three structural parameter as main influential regarding the cathode catalyst layer performance including the ionomer volume fraction, the electrode thickness, and platinum loading.[28] Thus, these parameters should be consecutively varied whereas the platinum loading remains constant due to production requirements and its costs. First, a targeted manipulation of the ionomer volume fraction with maintaining catalyst particle size distribution width is performed. Four ionomer to carbon ratios were chosen including 1.00, 1.10, 1.20, and 1.35.

5.2.1 Catalyst dispersion analysis

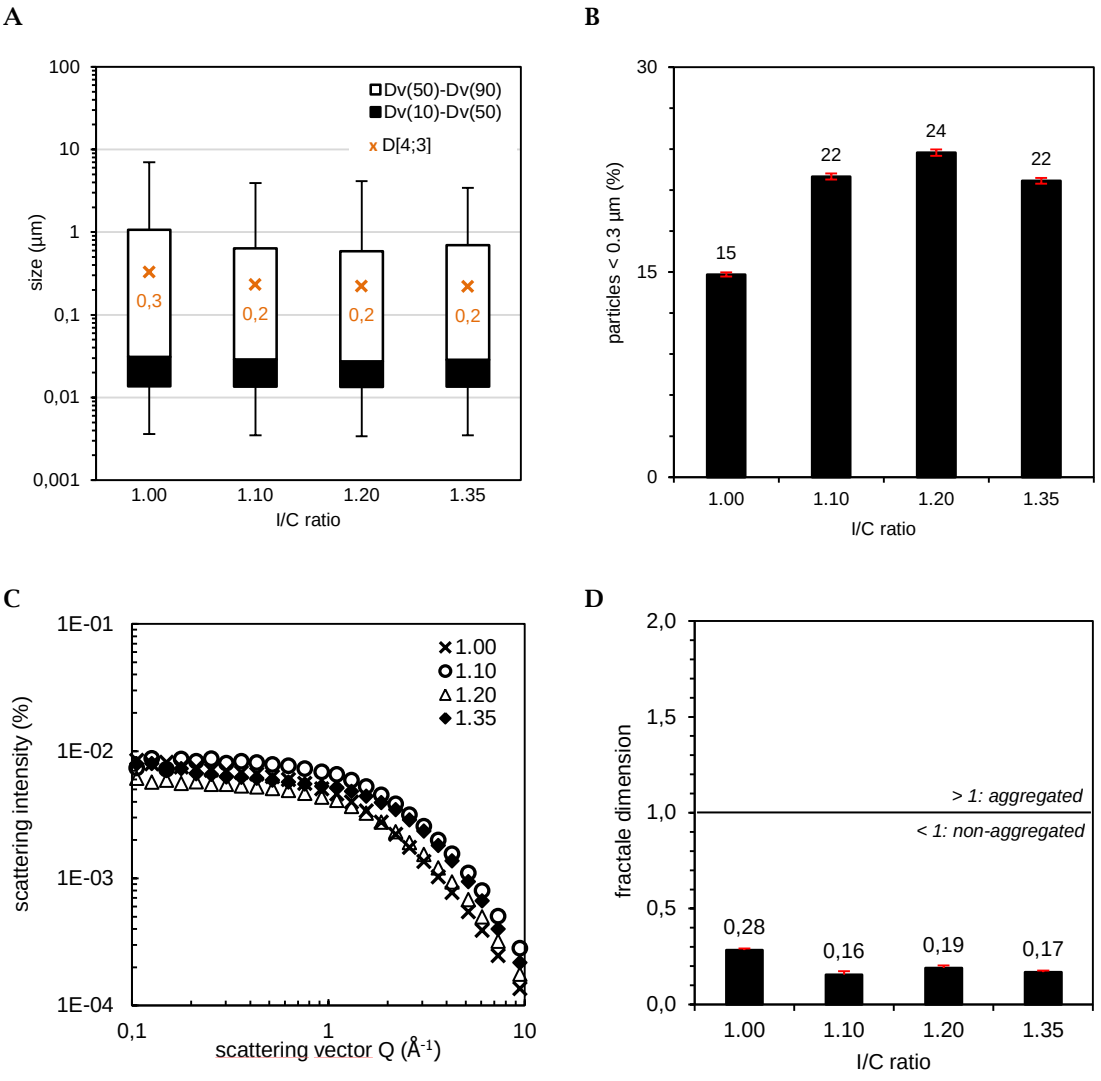

Fig. 5.17 Particle size characteristics obtained from SLS measurements for synthesized catalyst dispersions with diverse ionomer loadings: (**A**) particle size distribution, (**B**) relative amount of particles smaller 0.3 µm, and (**C**) internal aggregation structure plot and its corresponding D*f* values (**D**).

Fig. 5.17 (A) illustrates particle size distributions obtained from the investigated catalyst dispersions with varied ionomer content. All samples show similar distributions widths including a

maximum size of 10 µm whereas the main fraction is achieved in between 0.01 µm and 1 µm. Moreover, increased ionomer volume fractions result in a slight decrease within the particle size distribution due to the additional stabilizer. The volume–weighted particle diameter, D[4;3], shrinks from ~328 nm (I/C 1.00) to ~219 nm for I/C 1.35. Thus, the relative amount for small particles (<0.3 µm) in Fig. 5.17 (B) also yield the highest value for I/C 1.35. The catalytic ink internal structure analysis (Fig. 5.17, C) depicts similar results for fractal dimension values of averaged 0.17 with the exception of 0.28 for I/C 1.00 which correlates with the lower amount of small particles (Fig. 5.17, B) indicating a higher amount of agglomerates within the obtained particle size distribution (Fig. 5.17, A).

5.2.2 Electrode analysis

The ionomer volume fraction is important for particle stabilization in catalytic inks whereas its function within the catalyst layer is crucially essential for the fuel cell performance. The catalyst particles have to be coated with ionomer in order to guarantee catalytic active area but also remaining ionomer is needed for network development. Thus, the ionomer distribution and its structural influence on the pore network are subsequently investigated. Especially, the question is if the ionomer loading influences the pore size distribution characteristic or if the particle size distribution determines the pore network.

5.2.2.1 Surface analysis using imaging techniques

Optical surface analysis could not identify detailed differences between the four investigated electrodes with varied ionomer loadings (Fig. 5.18). Surface roughness measurements yielded averaged 0.257 µm corresponding to similar low crack areas of ~0.7 % for all investigated samples. Furthermore, SEM analysis yields similar pore structure including non–altered catalyst morphological structure. Even transmitted light photography gives no further insights (Fig. 5.18, C). The detected void areas range from 0.01 % to 0.05 % and bear no correlation to the electrode´s ionomer loading.

5.2.2.2 Cross-sectional characterization

Catalyst layer thickness show similar appearance with averaged 8.5 µm for all four designs as illustrated in Fig. 5.19 (A). Additional elemental EDX mapping of the cross–sectional area demonstrate a decal sided fluorine accumulation almost independent of the electrode´s ionomer loading (Fig. 5.19, B). It should be noted that this accumulation could also be possibly related to a method's artefacts. Thus, it is hypothesized that the drying process is not optimized with respect to homogeneous material distribution. It seems that diffusion or evaporation process causes a flow of material resulting in detected material accumulation. Furthermore, a closer look allows the postulation of a fluorine accumulation thinning with increasing ionomer loading possibly underlining a viscosity dependent on drying process or the ionomer dependent network creation ability respecting its gel structure. In contrast, Fig. 5.19 (C) illustrates a highly homogeneous platinum distribution.

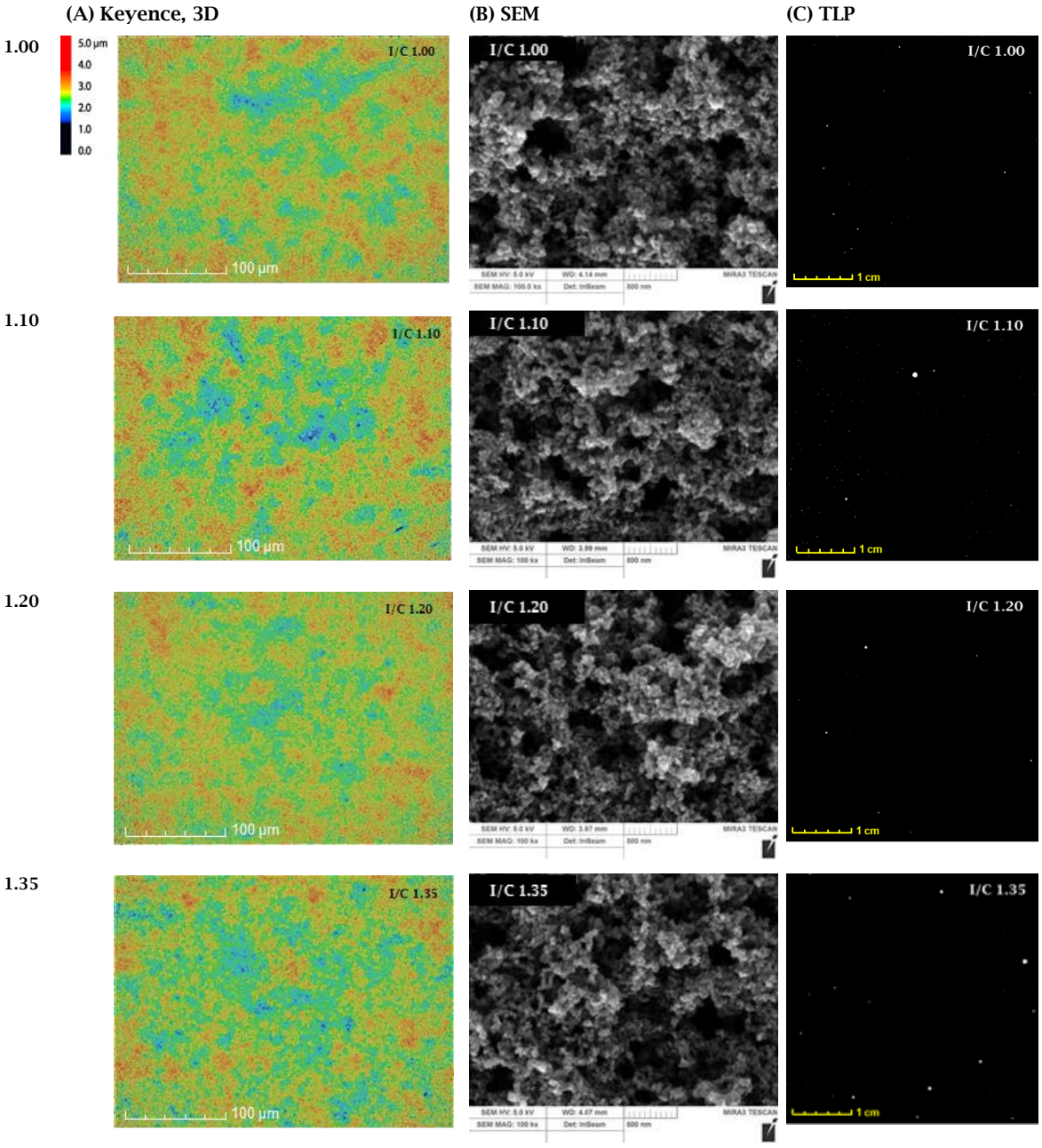

Fig. 5.18 Surface analysis results for four electrode designs obtained from diverse techniques: (**A**) laser confocal 3D and (**B**) SEM images. (**C**) show binary images of transmitted light photography.

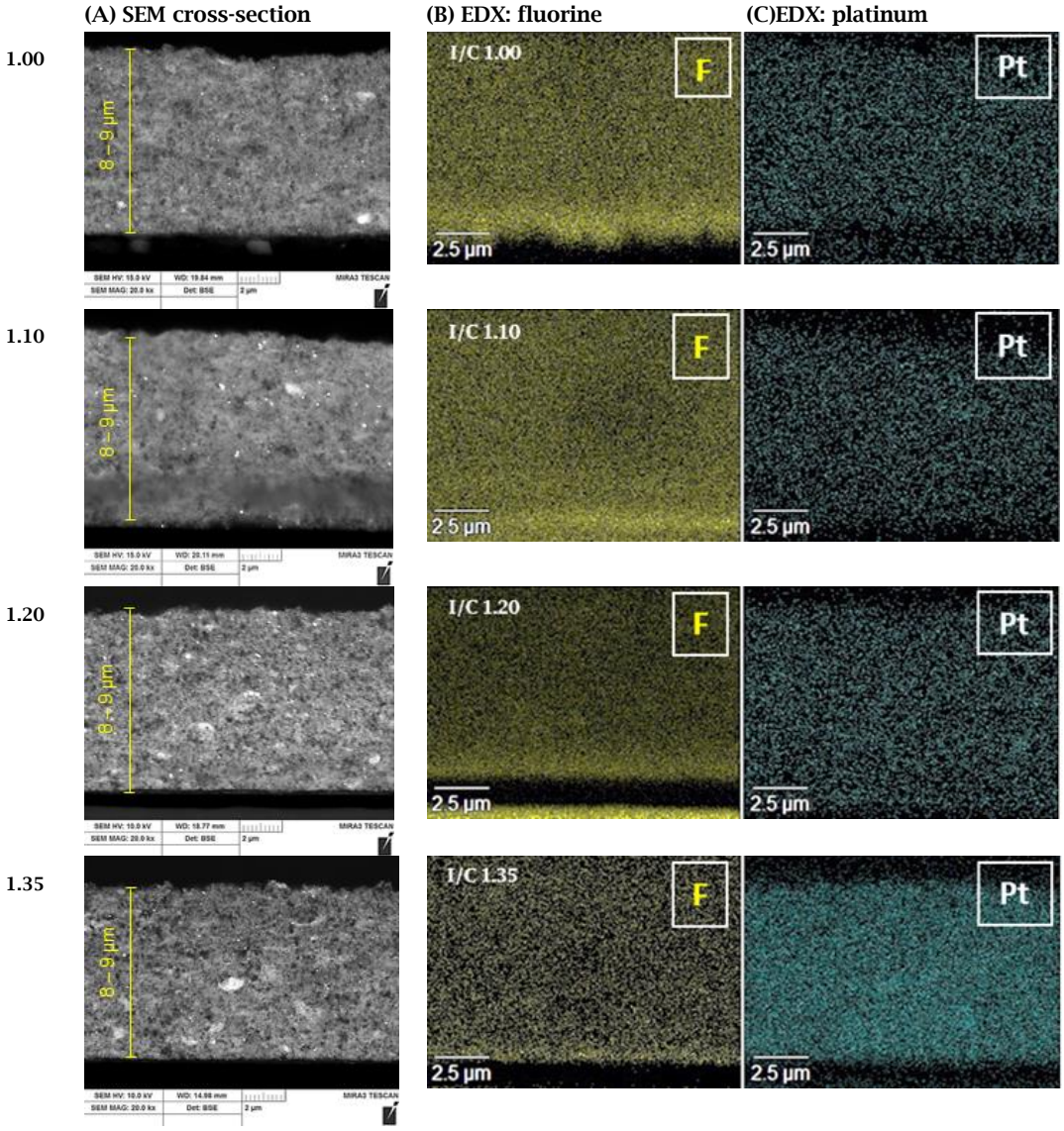

Fig. 5.19 Electrode lateral view images achieved from SEM cross-section images (**A**) for 4 designs. Additional elemental EDX mapping for fluorine (**B**) and platinum (**C**) illustrate material distribution. The platinum loading of the investigated catalyst layers is constant at 0.25 mg/cm².

5.2.2.3 Gas sorption analysis

Gas sorption experiments supplied more reliable data regarding morphological differences between the investigated catalyst layers. The obtained nitrogen adsorption–desorption cycles are depicted in Fig. 5.20 (A). According to the IUPAC sorption isotherm classification, all samples follow type IV isotherms corresponding to mesoporous material.[59] The characteristic hysteresis loops (zoom in Fig. 5.20, A) are indicated by H2 type according to IUPAC hysteresis loop classification and demonstrate the presence of pore networks.[59,72] The application of the advanced network model proposed by Seaton et al. allows the determination of the network characteristics, namely the mean coordination number, Z, and the linear dimension, L (Fig. 5.20, B).[81,91] Z and L present contrary trends: Z shrinks with increasing ionomer loadings while L demonstrates a maximal value of 7.8 for I/C 1.20 which feasibly indicates highly active regions. Furthermore, Z results can be categorized into two groups: low ionomer loadings (I/C 1.00, 1.10) with an averaged Z value of 3.35 and high ionomer loadings (I/C 1.20, 1.35) with 24 % reduced Z values of averaged 2.65 (Fig. 5.20, B). In order to achieve high pore connectivity, low ionomer loadings – resulting high pore connectivity – are recommended. In contrast, a high amount of active areas is created with high ionomer loadings. Hence, it is hypothesized that these two network characteristics could be used for cathodic fuel cell performance prediction. Considering the necessary trade-off decision

between sufficient ionomer network and pore network development these characteristics could also be used. But referring to the derived data in Fig. 5.20 (B) it is not clear which parameter is more important regarding fuel cell performance. Thus, medium ionomer loadings such as I/C 1.10 and 1.20 present promising candidates.

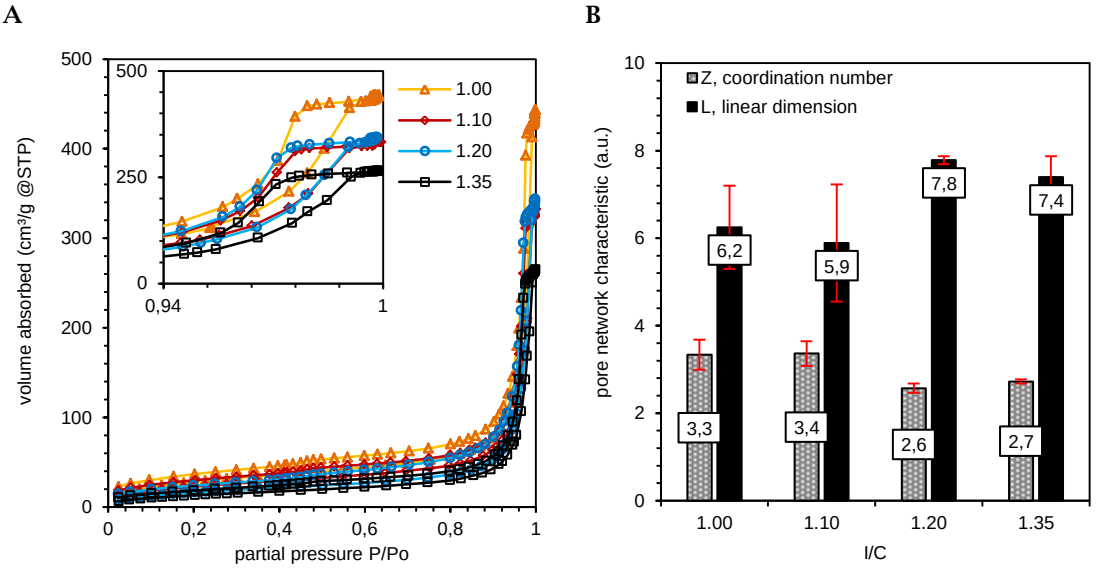

Fig. 5.20 (**A**) Nitrogen sorption isotherms obtained from electrodes coated on decal film. Zoom illustrates their hysteresis loops. (**B**) present the corresponding pore network characteristics using the advanced pore network model proposed by Seaton et al.[81]

BET analysis is performed by using the adsorption data within the range of 0.05 – 0.3 P/P_0 and applying Micropore BET Assistant offered by the instrument's software. As illustrated in Fig. 5.21 the catalyst powder surface area (SA) of 360 m^2/g was not reproduced for the catalyst layers due to the addition of ionomer which coats the catalyst powder particles. Thus, the lowest ionomer loading (I/C 1.00) yielded the highest surface area of 113 m^2/g while the highest loading (I/C 1.35) resulted only in 55 m^2/g which equals a difference of 55 %. Considering the total SA obtained from QSDFT calculation, a surface area drop in between I/C 1.00 and I/C 1.35 of 51 % was achieved. This finding can be interpreted as overall loss in pore volume rather than ionomer coating. Regarding the micropore region, an equal trend was discovered: both models – the classical (de Boer) and statistical (QSDFT) approach – present high micropore surface areas for low ionomer loading and 67 % or 50 % reduced surface area for the lowest ionomer loading of I/C 1.35 (Fig. 5.21).

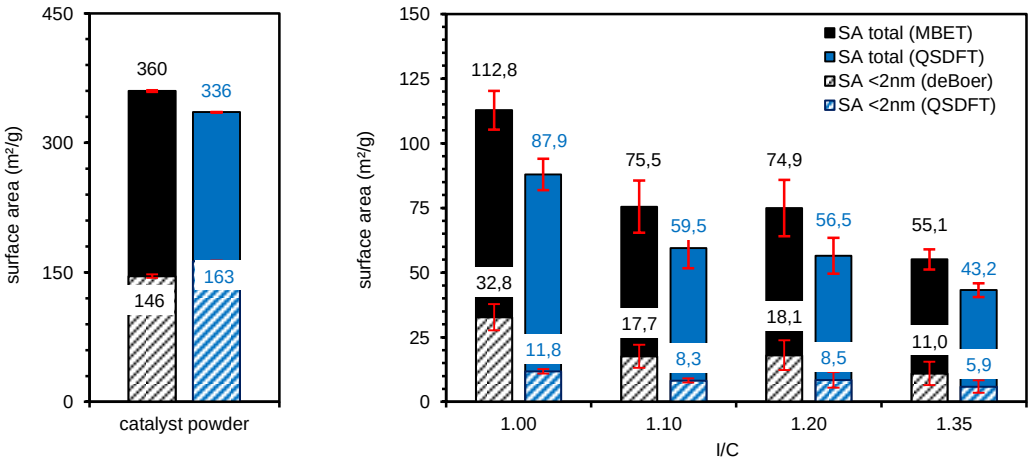

Fig. 5.21 BET surface area for a common fuel cell catalyst powder and manufactured catalyst layers containing approximately 60 % catalyst per g electrode.

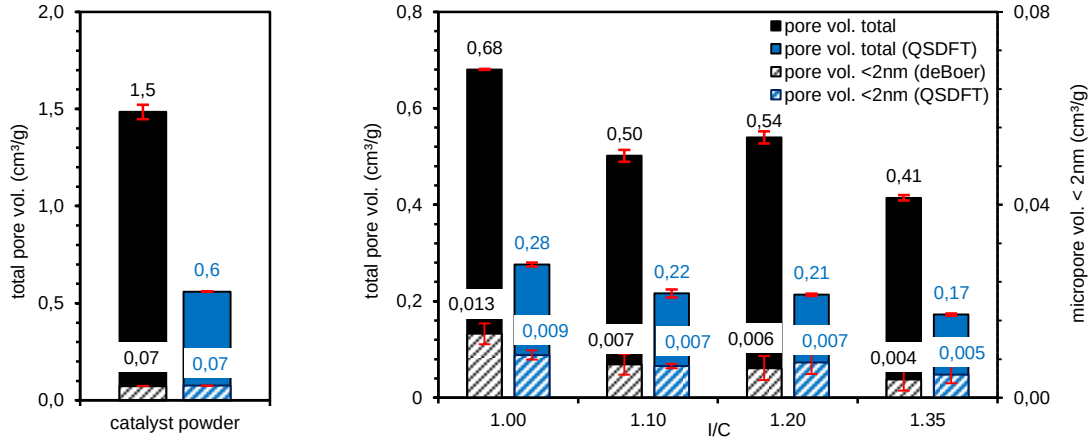

Fig. 5.22 Illustration of the total pore volume for the catalyst powder and the investigated catalyst layers applying a classical and statistical approach.

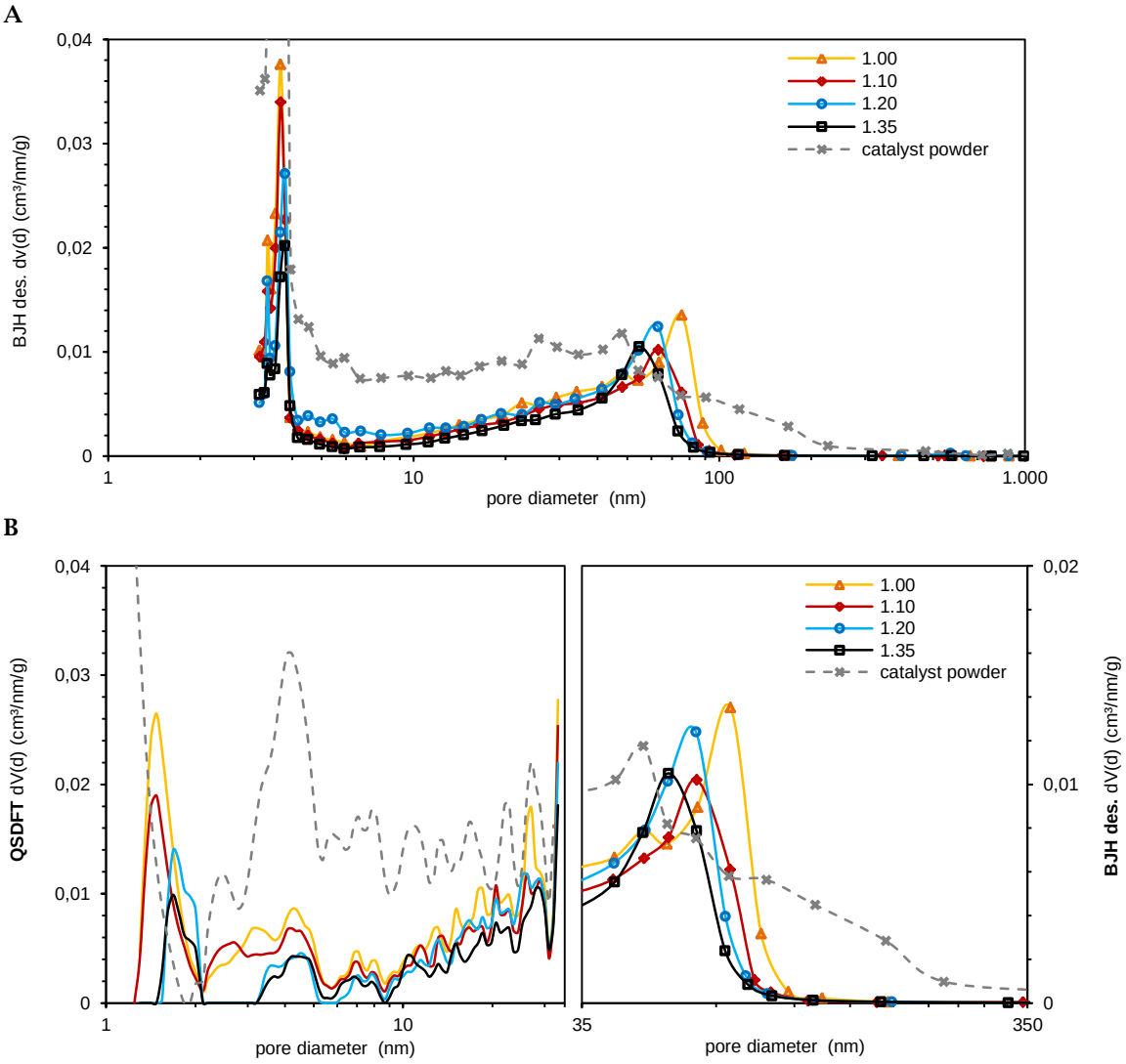

Fig. 5.23 Pore size distributions (PSDs) for four I/C designs and the initial catalyst powder obtained from desorption data using BJH method (**A**). The PSD plot obtained from a statistical QSDFT model (**B**, left) presents further details in between 1 - 30 nm pore diameter while meso- and macropores should be illustrated by the BJH model (**B**, right).

Additional pore volume analysis at 0.998 P/P_0 results also a difference of 40 % in between the lowest and highest ionomer loading for both classical and statistical approach (Fig. 5.22). Even the micropore volume decreases by 45 % for high ionomer loadings in comparison to low loadings (QSDFT model, Fig. 5.22). Concluding, as more ionomer is added to the catalyst ink, the less pore volume will be found in the resulting electrode microstructure regardless of the pore diameter. These findings are in good agreement with the postulations by Soboleva's group.[46] They reported ionomer existence within secondary pores (macropores) presumably distributed on agglomerate's surface when low ionomer loadings are applied. The illustrated pore size distribution results (Fig. 5.23, A) underline the findings of Soboleva et al.[46]: the more ionomer is loaded to the electrode as more the PSD width shrinks and shifts to smaller pore diameters. Further on, the second main peak at 75 nm for the low I/C 1.00 shifts to 55 nm for the highest ionomer loading of I/C 1.35 while all other peaks remain on constant position. As identified before, the pore volumes decrease also within the micropore and narrow mesopore region. This phenomenon can be linked to the fact that only surface areas of pores >20 nm are available for ionomer distribution which means in turn, the lower the SA available for ionomer distribution the thicker the created ionomer layer is.[46] However, the experimental sorption findings are supporting Soboleva et al. postulations which are noticed to be in contrast to the literature-known observations by Uchida et al. who reported that primary pore volume within agglomerate (mesopores) remains unchanged with increasing ionomer content whereas the volume of the secondary pores (macropores) decreas.[29,45]

Regarding the main influential parameter determining the cell performance, the total ionomer volume fraction was one of the identified characteristics.[20] The other two, platinum loading and catalyst layer thickness are known to remain unaffected during this study. Thus, as presented in Fig. 5.22 the ionomer loading strongly influence the surface area and total pore volume of a catalyst layer. The preliminary drawn picture for the need of a trade-off decision is further underlined: a suitable porosity containing both primary and secondary pores is the key for running the electrochemical reaction (Fig. 5.20 and Fig. 5.22). Simultaneously, the supplied ionomer network and its coating layer thickness need to guarantee the proton conductivity which leads to the recommendation of I/C design 1.10 or 1.20.

Concluding, the catalyst particle size distribution is the main cause for determining the internal electrode pore structure. The total pore volume and surface area can be adjusted by the supplied ionomer content: the higher the ionomer fraction the less the resulting total pore volume and surface area are. Due to the fact that the ionomer cannot fill pores of small diameter (estimated as smaller than 20 nm), increased ionomer loadings yield thicker ionomer layers coating the primary catalyst particles (Fig. 5.24). Further validation is found by applying the advanced network model characteristics which correlate the coordination of a network pore with the supplied ionomer content: the less ionomer is added the higher a network pore is coordinated with its surrounding pores (Fig. 5.20, B).

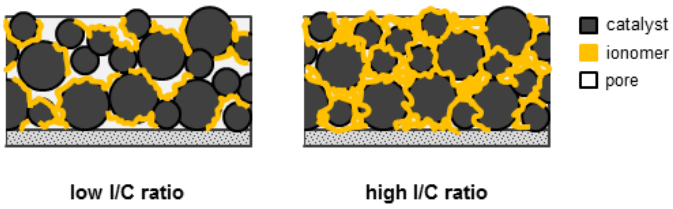

Fig. 5.24 Model description for low and high I/C ratios and their impact on the internal surface area and pore volume.

5.2.3 Electrochemical component testing

The previous obtained morphological results give contrary suggestions regarding an ideal catalyst layer ionomer loading. On the one hand, high surface area as well as a broad pore size distribution was obtained for the lowest investigated I/C of 1.00 whereas on the other side (I/C 1.35) ionomer accumulation was detected. Considering the advanced network model characteristic, Z, the ideal

ionomer loading for the given platinum loading (0.25 mg/cm²) and catalyst particle distribution is expected to be in the range of I/C 1.10 and 1.20. Hence, electrochemical testing should help in finding the ideal ionomer volume fraction.

Since all specimens contain similar catalyst particle diameters no differences are expected during normal condition operating state performance as illustrated in Fig. 5.25. Within the kinetic region (low current densities) no significant differences are detected for the polarization curve recording. Contrary, it seems that there is a slight trend for the high ionomer loading resulting in higher active area utilization (fast transient polarization (FTP) recording, Fig. 5.25 down left). Corresponding to the PSD curve for I/C 1.35 most catalyst surface is covered by ionomer which leads to increased catalytic active areas (Fig. 5.23). Moreover, the characteristic I–V curve obtained for I/C 1.35 differentiate most from all other designs with an averaged gap of 50 mV (Fig. 5.25, down right). At high current densities I/C 1.20 perform superior, followed by I/C 1.00 and 1.10. This observation is in good agreement with the previous obtained structural information which suggested I/C 1.10 or 1.20. It is crucial for ideal cell behavior to find a suitable design guaranteeing both mass transport (high electrode porosity) and proton conductivity through the ionomer network.

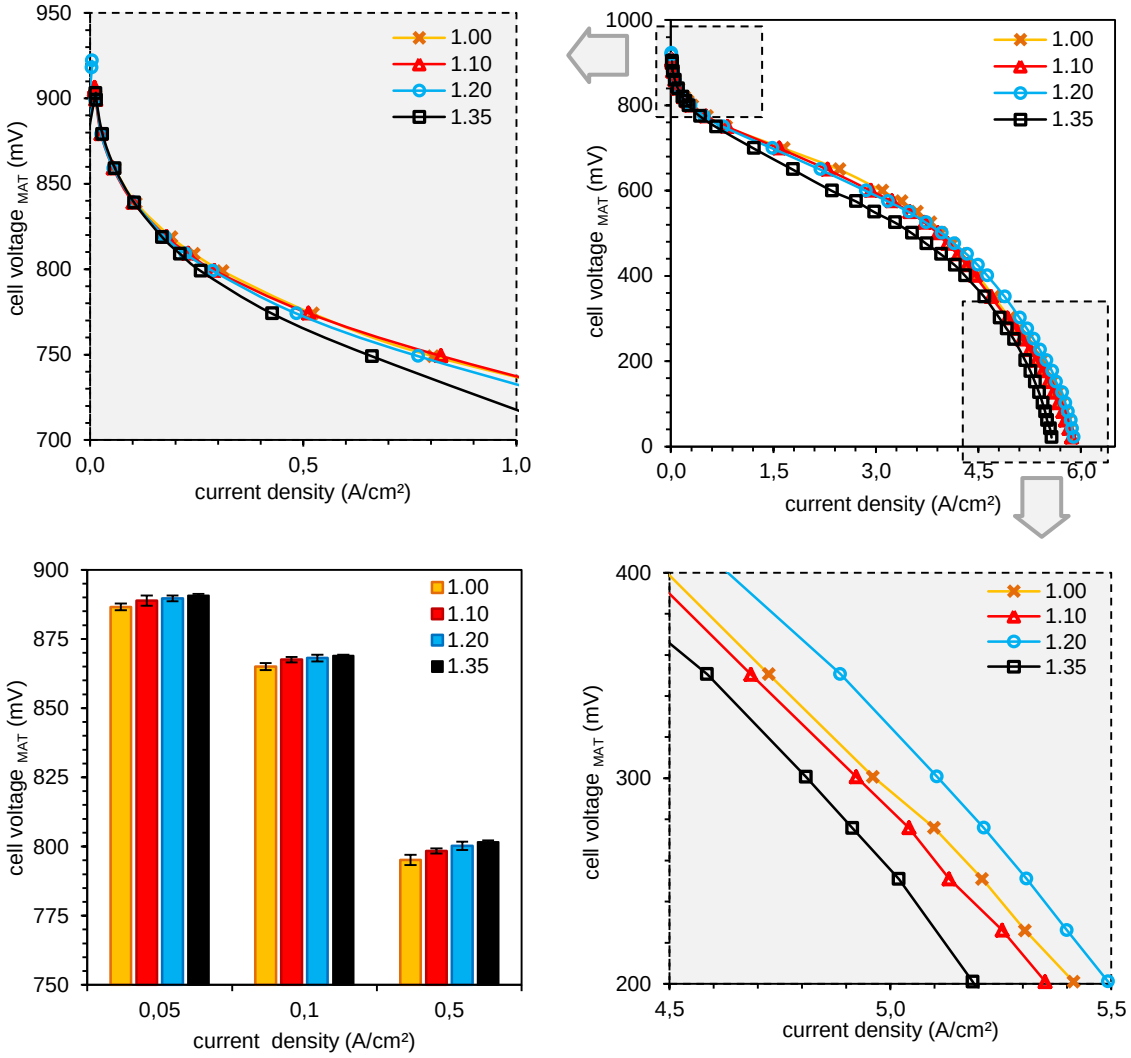

Fig. 5.25 Polarization curves obtained from applied voltages in the range of 0–1 V. Current densities were recorded at 68° C at 100 % RH. Additional OCV cleaning was performed in between the measurement points. Zoom 1 (top left) illustrate the kinetic area including the corresponding cell voltages at 0.05, 0.1, and 0.5 A/cm² whereas zoom 2 (down right) depict the mass transport area. Down left illustrates fast transient polarization (FTP) results for diverse current densities.

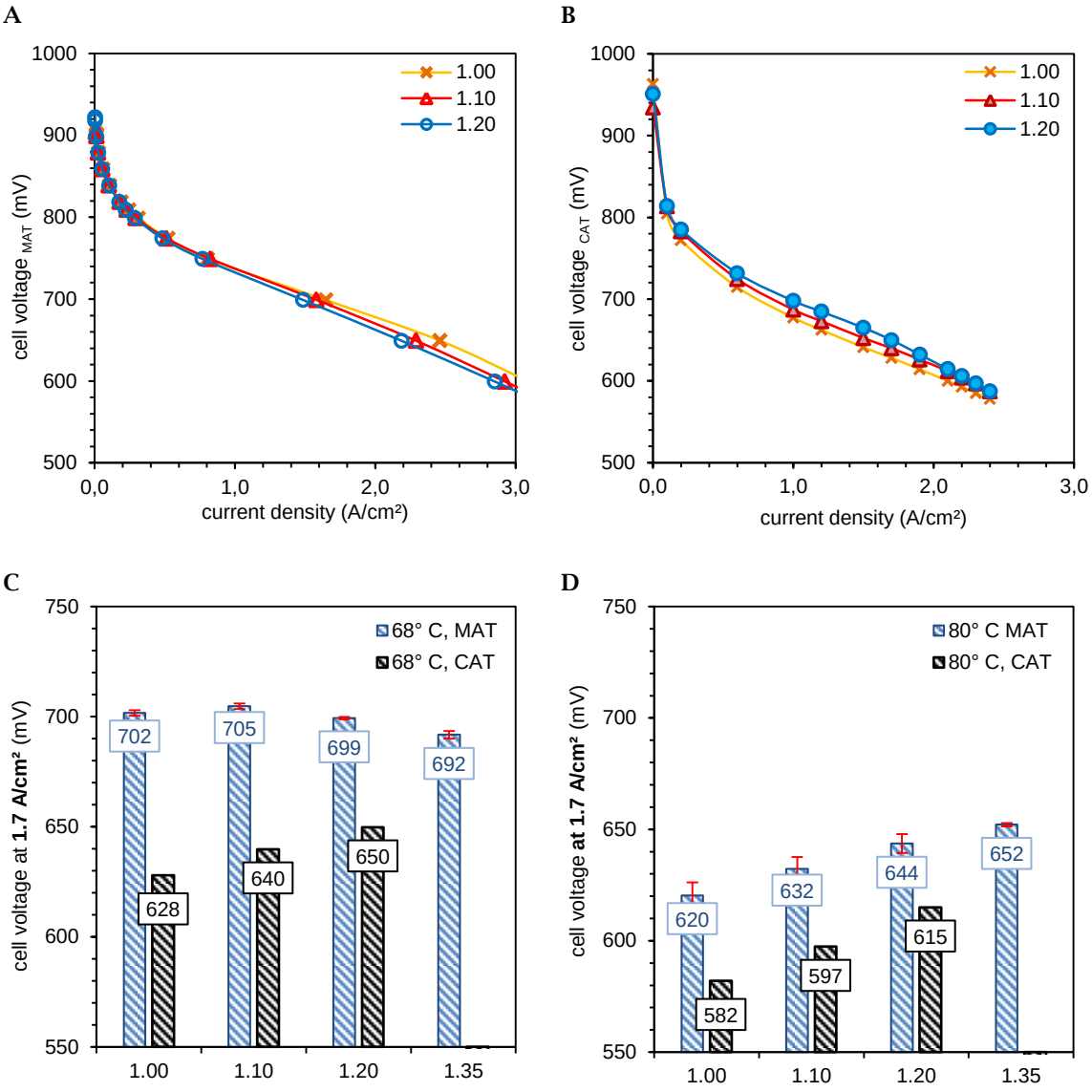

Fig. 5.26 Polarization curves obtained from MAT (**A**) using circular 3 cm² active area and CAT (**B**) operating with rectangular sampled active area of 40 cm². Cell performances are recorded at 68° C at 100 % RH. I/C 1.35 sample failed during CAT testing due to leakage issues caused by sample preparation. Steady state point results for normal and hot conditions are illustrated in (**C**) and (**D**), respectively.

In order to validate the recorded polarization curve with the MAT testing station, the four electrode designs were also tested using a CAT testing station (Fig. 5.26 A, B). The stations predominantly differ in investigation area: MAT testing works with circular 3 cm² active area whereas CAT testing samples require rectangular shape and 40 cm² of active area. It should be noted that CAT testing is more realistic and its results more reliable with respect to membrane electrode assembly (MEA) geometry and flow field application. However, the polarization curves received from CAT testing yield comparable results. Essentially here I/C 1.20 is identified as promising candidate demonstrating suitable performances over the whole range of current densities (Fig. 5.26, B). Diving into the steady state points achieved at 1.7 A/cm² for different operation conditions, allows more precise assumptions. First, at normal conditions (68° C, 100% RH) contrary results are obtained from MAT and CAT testing: cell performance at MAT decrease with increased ionomer content whereas the cell performance on CAT testing increase with increased ionomer loading (Fig. 5.26, C). It is expected that the cell performance at low relative humidity and high temperatures is increased with higher ionomer loadings due to sufficient proton conductivity. Hence, a valuable recommendation is impossible with respect to the confusing data. Since the specimens are obtained from one production charge, the testing protocol or station should be reviewed. Furthermore, CAT testing yields lower performance values compared to MAT testing

which could be correlated to the varying investigation areas. The second condition at 80° C and 50 % RH yielded for both stations, MAT and CAT, corresponding trends by performance increase with increased ionomer content as illustrated in Fig. 5.26 (D). Thus, the holy grail of fuel cell electrode design lies in high cell performance during normal condition and low losses during hot operating conditions. The electrode needs to adapt to the applied driving cycles including temperature variations owed to the surrounding climate conditions. Fig. 5.27 demonstrates a scatter diagram for both operating conditions in which the measurement results could be classified. The best case includes samples operating at high cell voltages for both applied conditions simultaneously meaning a low performance loss at hot conditions (green area). In turn, the worst case contain samples generating low performances for both conditions, normal and hot (red area). Respecting the confusing MAT data only the CAT testing results are taken into account for capability analysis. Thus, I/C 1.20 is identified as best scenario candidate which is in good agreement to the previous findings regarding microstructural analysis.

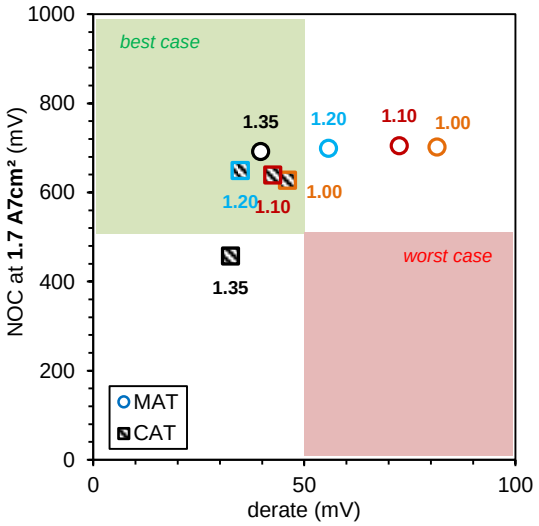

Fig. 5.27 The diagram illustrates suitable specimens fulfilling both required criteria of high cell performance at normal and low performance loss at hot condition.

5.2.4 Conclusion

Tuning the ionomer loading of catalyst layers faces two functional requirements: the ionomer itself coating the catalyst particles and simultaneously creating an interconnected network for proton transport and mechanical strength. Thereby, the ionomer fraction determines the void space volume. In order to obtain high cell performances, high surface area including sufficient pore volumes for mass transport, adequate catalyst particle coating, as well as high network connectivity are necessary. SLS analysis verifies constant particle size distribution for all four electrode designs containing diverse ionomer ratios ranging from I/C 1.00 to 1.35 (Fig. 5.17). Moreover, all catalytic inks show non-aggregated dispersion state resulting in smooth, crack-free, and homogeneous catalyst layer surface appearance (Fig. 5.17 and Fig. 5.18). Cross-sectional analysis yielded also similar CL thicknesses of averaged 8 µm. Homogeneous platinum distribution as well as a possibly decal-sided fluorine accumulation were detected by using cross-sectional elemental EDX mapping for all four designs (Fig. 5.19). Thus, the applied characterization techniques were not able to differentiate between the investigated specimens. Similarly, nitrogen sorption technique identified the resulting CL isotherms as H4 type and their corresponding hysteresis loops as H2 type, respectively (Fig. 5.20, A). In contrast, the application of the advanced network model proposed by Seaton et al. resulted in a differentiation between the samples: the mean coordination number, Z, and the linear dimension, L, demonstrate concurring trends. High ionomer loadings lead to a decrease in pore connectivity whereas L is increased so that only I/C 1.10 and 1.20

present possible candidates (Fig. 5.20, B). Respecting the BET SA and total pore volume results (both reduced by increased ionomer loadings), no clear I/C can be chosen. Of course, the highest BET SA and total pore volume were achieved with the lowest supplied ionomer loading I/C 1.00 which support mass transport mechanisms but disregard catalyst utilization. Referring to the linear dimension L, I/C 1.20 should preferably recommended. It is assumed, that this characteristic possibly provides insights about the amount of active areas within a pore. Considering the electrochemical testing results, I/C 1.20 actually demonstrates the highest cell performance over a broad range of current densities. Thus, it is obvious that the advanced pore network characteristics could help in cell performance prediction.

5.3 CL microstructure tuning by particle size distribution variation of catalytic inks

In order to follow the correlation of catalyst dispersion particle size distribution to the catalyst layer pore structure diverse catalyst dispersion designs were synthesized and further processed. All electrode types should be electrochemically tested focusing the validation of the cell performance determination by catalytic ink properties especially their catalyst particle size distribution. As shown in chapter 5.2 the catalyst particle diameter is claimed as main influential structure determining the overall pore structure. In contrast, the ionomer volume fraction was correlated to affect the created void space directly measurable as variance within the BET SA and total pore volume. As a result, corresponding cell performances do not differentiate significantly in between the investigated ionomer volume fractions. Thus, the particle size distribution variations are expected to yield measurable performance variations.

5.3.1 Catalyst dispersion analysis

Fig. 5.28 illustrates eight diverse cathodic catalytic ink designs created by solid content and batch volume variation affecting the mixing effectiveness resulting in different catalyst agglomerates and broader particle size distributions. Even though, a prolonged catalyst wetting time yielded distributed particle sizes. In general, all investigated samples depicted here run a seven day mixing process with equal energy input (except for sample #8 where a higher energy input was used in order to create a monomodal particle size distribution). Moreover, all samples are based on I/C ratio of 1.10 and were filtered through a 20 µm pore width membrane directly before coating. The created particle size distributions are classified into three designs: design 1 contains agglomerates lager than 10 µm diameters while design 2 is identified by particle size distributions ranging in between 1 and 10 µm diameters. In contrast, design 3 includes only particles smaller 1 µm diameter (Fig. 5.28, sample #8). Each design is represented by one specific sample: sample #1 for design 1, sample #3 for design 2, and sample #8 for design 3, respectively.

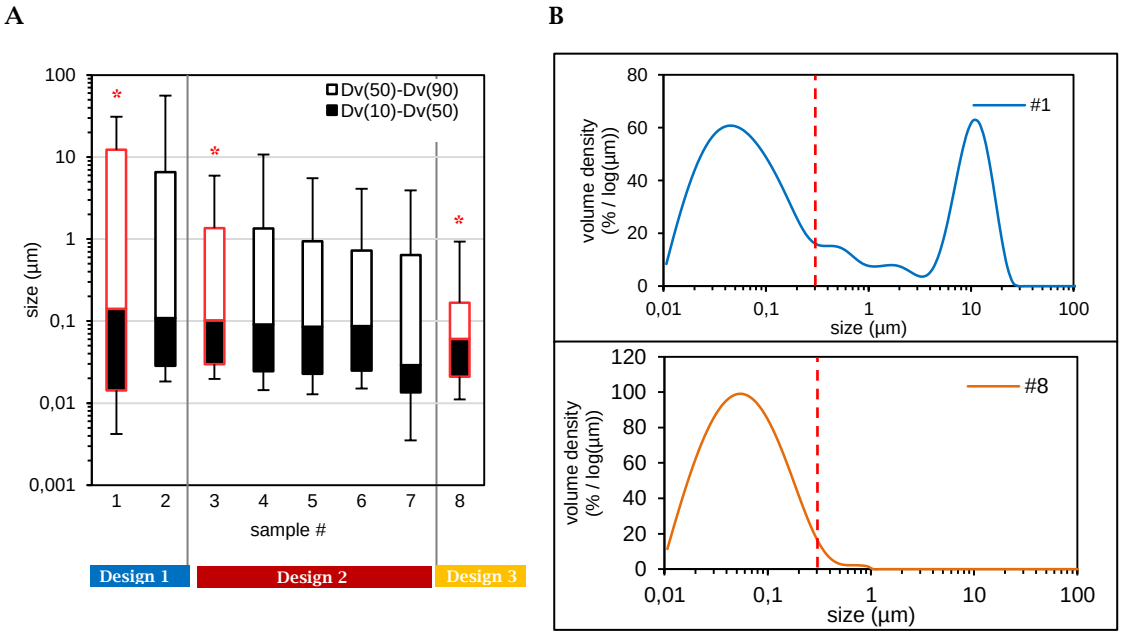

Fig. 5.28 (**A**) Particle size distributions for diverse variations categorized into three designs. The highlighted samples (*) represent their corresponding designs. The particle size distributions plotted in **B** illustrate the two extrema for the design range: sample #1 (bimodal) and #8 (monomodal).

The particle size characteristics obtained from SLS measurements are demonstrated in Fig. 5.29: all three characteristics – relative amount of small particles, volume-weighted mean diameter, and the fractal dimension of the catalyst dispersions – follow the design classification.

Fig. 5.29 (B) illustrates the relative amount of small particles which is increased by particle size distribution width shrinkage. Thus, small particles result from the loss of agglomerates. Design 3 contains a monomodal distribution including ~90 % of particles smaller than 0.3 µm diameter whereas polymodal distributions are found in all other seven samples yielding 20 – 30 % small particles for design 2 or only less than 4 % for design 1, respectively. Furthermore, the agglomerate sensitively volume-weighted mean diameter shows a contrary trend: the mean diameter decreases for particle size distribution width shrinkage. Moreover, the presence of agglomerates and in turn the amount of small particles, affects the development of microclusters measurable by using the fractal dimension. Here, the depicted D*f* values in Fig. 5.29 (D) obtained from the log-log plot in Fig. 5.29 (C) illustrates three cases according to the previous design classification: case 1 contain D*f* values greater than 1 referring to aggregated catalyst dispersions (design 1) while case 2 demonstrates non-aggregated dispersions with D*f* values below 1 (design 2). In contrast, design 3 presents a special condition where Mie scattering is observed (Fig. 5.29, D**). This phenomenon is correlated to monodispersed suspensions matching the monomodal particle size distribution. For this case, the mathematical D*f* value determination is invalid.[64]

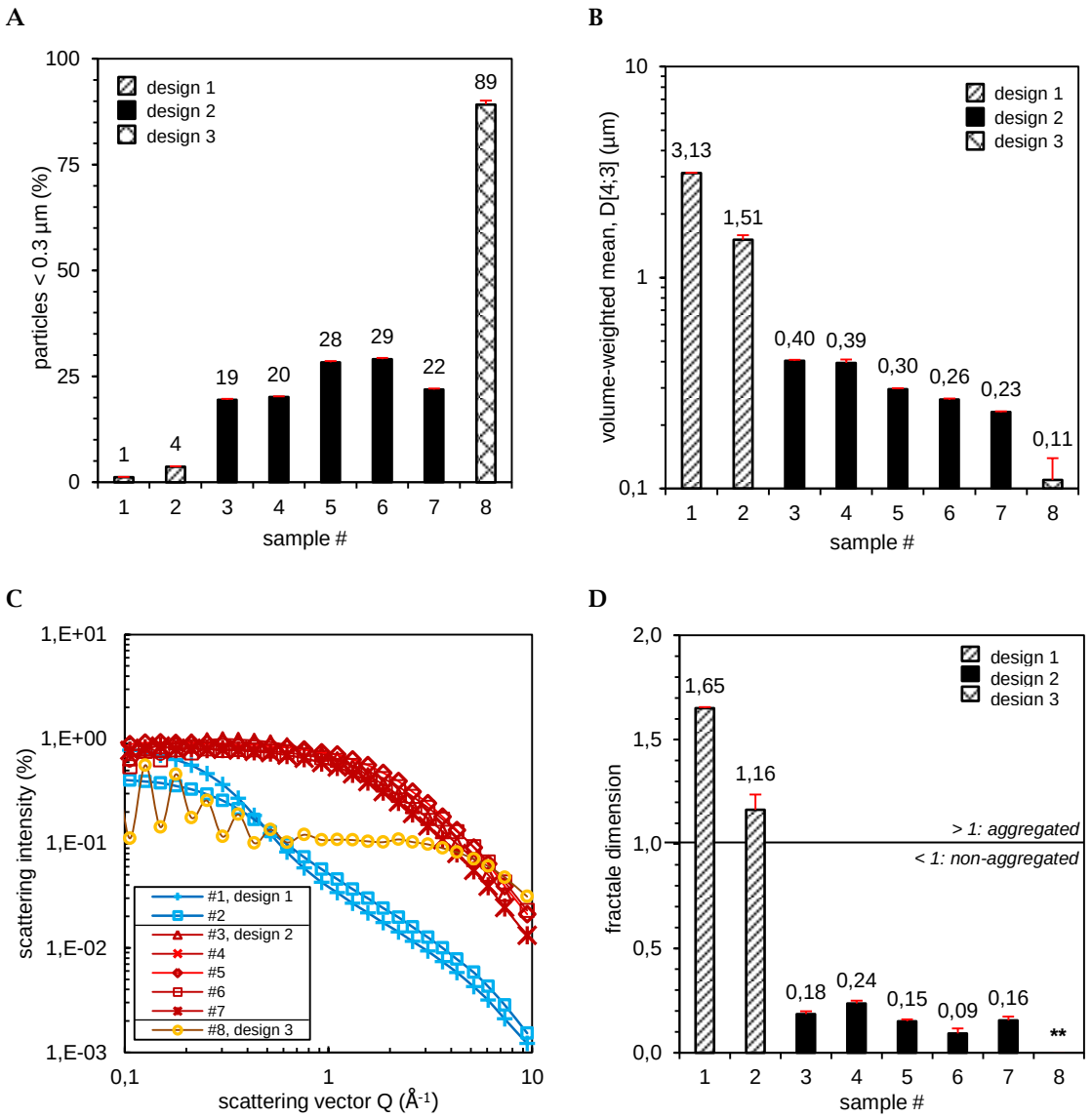

Fig. 5.29 Particle size characteristics obtained from SLS measurements for synthesized catalyst dispersions: (**A**) relative amount of particles smaller 0.3 µm, (**B**) volume-weighted mean D[4;3], and (**C**) internal aggregate structure plot and its corresponding D*f* values (**D**). **invalid calculation due to Mie scattering

5.3.2 Electrode analysis

The eight diverse catalyst dispersions were further processed in order to obtain coated catalyst layers also designated as cathodic electrodes. The aim is to correlate the catalyst dispersion properties directly to the electrode´s performance. Therefore, a comprehensive electrode investigation is crucial with respect to microstructural influences.

5.3.2.1 Surface analysis

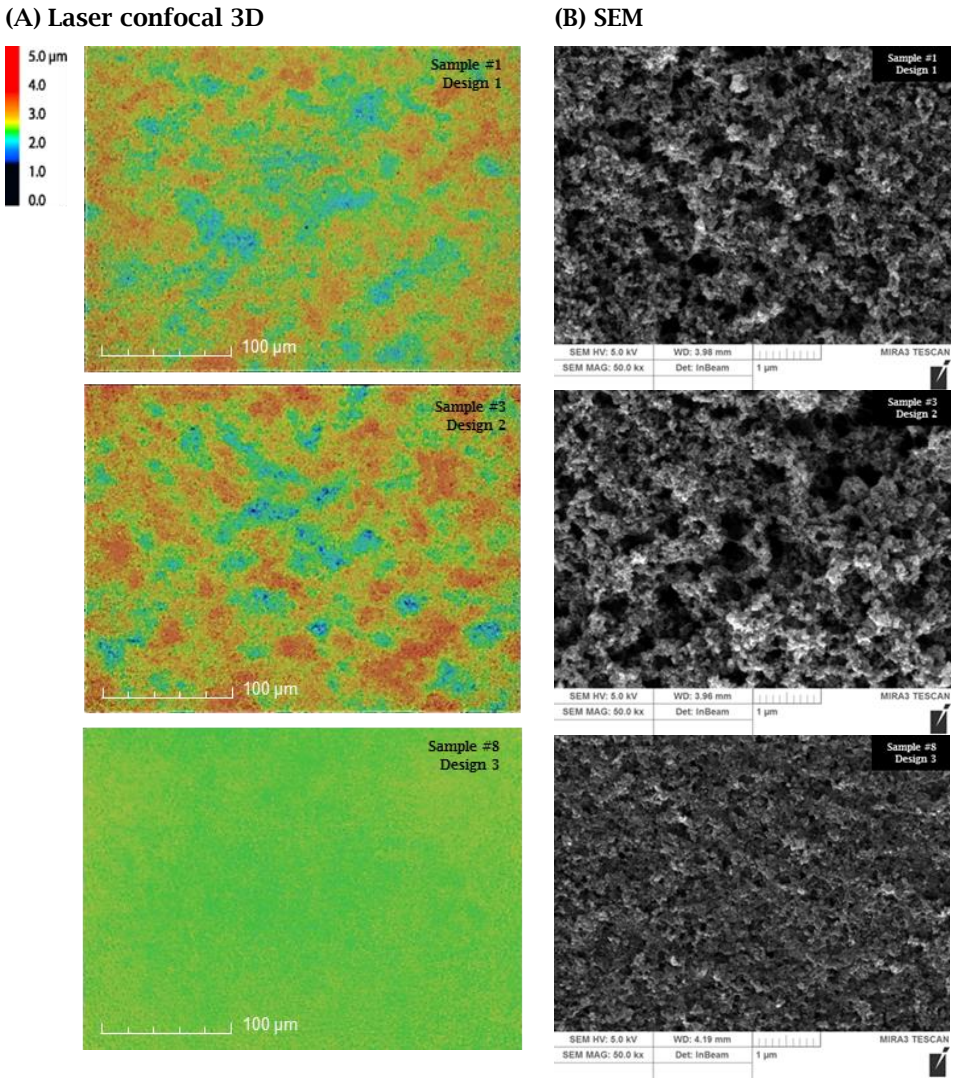

Fig. 5.30 Surface analysis images obtained from (**A**) laser confocal microscopy and (**B**) scanning electron microscopy. The illustrated samples represent their design.

Fig. 5.30 (A) illustrates electrode surface appearances obtained from laser confocal 3D imaging. All designs demonstrate crack–free and homogeneous film appearance. Moreover, design 1 and 2 display similar surfaces whereas design 3 differentiates from these two designs with extremely smooth surface appearance. According to Fig. 5.31 design 3 yields the smallest value for the averaged surface roughness with ~0.10 µm. Design 2 roughness range in between 0.22 and 0.52 µm whereas design 1 show averaged surface roughness of ~0.24 µm which is remarkable with respect to its large catalyst agglomerates within the catalyst dispersion. It is expected that coarse dispersions, additionally demonstrating an aggregated dispersion state, result in high surface roughness due to their low electrode packing density. Thus, it is assumed that the design 1 samples (#1, #2) present some resolution error obtained for laser confocal imaging. In contrast, SEM imaging yields equal surface appearance for design 1 and 2 and differentiation for design 3. Referring to the visible pore sizes in Fig. 5.30 (B) it is clear that design 3 demonstrate tiny pore widths compared to design 1 and 2.

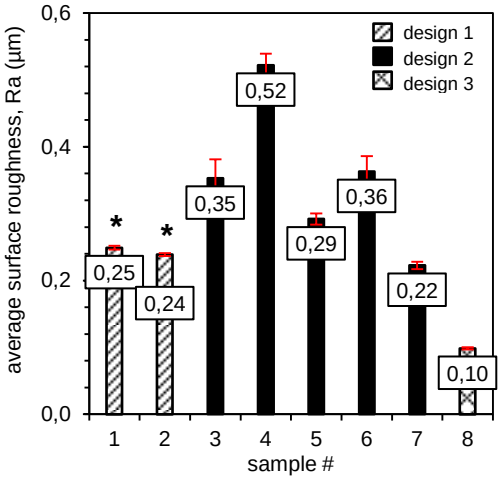

Fig. 5.31 Average surface roughness calculated from laser confocal measurements.

Additional cross-sectional analysis allows the catalyst layer thickness determination. As presented in Fig. 5.32 (A) the previously drawn picture of similarity for design 1 and 2 and differentiation of design 3 are further documented. Design 1 and 2 present similar thickness of ~8.5 µm and ~7.5 µm, respectively, whereas design 3 demonstrates a thickness reduction of 50 % resulting in ~3.5 µm.

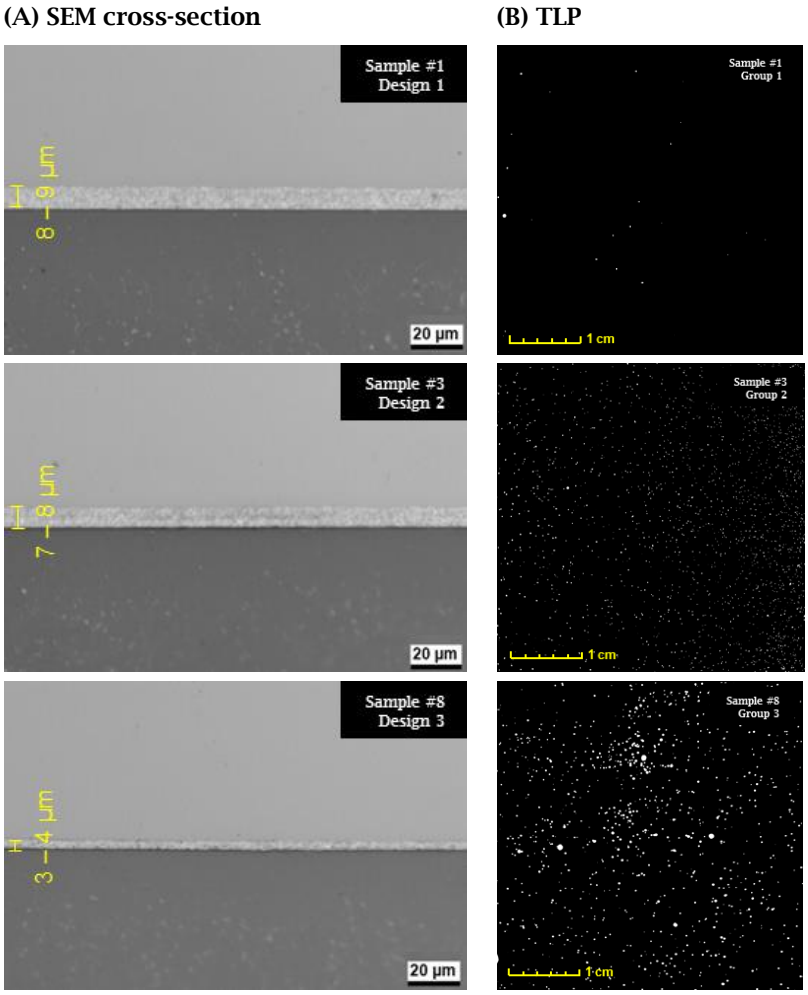

Fig. 5.32 Electrode lateral view images achieved from cross-sectional SEM investigation (**A**) and the corresponding surface view images obtained TLP analysis which is dependent from CL thickness (**B**).

This strong deviation is expected to yield a cell performance variation referring to Khajeh-Hosseini-Dalasm's group who identified the CL thickness as main influential parameter.[20] Furthermore, this work experimentally validate literature known particle packing density mechanisms even though a complex drying process takes place which is considered as negligible here. Thus, the CL thickness is directly tunable by catalyst agglomerate size adjustment within catalyst dispersion. According to the literature, the particle size distribution and the large to small particle ratio play a key role for the resulting film porosity.[96–98] The gained experimental findings underline the literature and equally validate their applicability to fuel cell electrode manufacturing processes. Thus, a monomodal catalyst particle size distribution below 1 µm as maximal particle diameter results in a thin catalyst layer containing a high particle packing density meaning in turn a less porous layer. In contrast, bi- or polymodal catalyst particle size distributions that contain larger agglomerates lead to thicker CLs with higher porosities and less particle packing densities. Concluding, the solid catalyst particle diameter created during catalyst dispersion preparation is responsible for the CL thickness determined by the particle packing density which affects in turn the CL porosity. Fig. 5.33 summarizes these experimental findings. Furthermore, it should be noted that all investigated catalyst layers are loaded with 0.25 mg/cm² platinum and ~30 % ionomer so that comparability is ensured.

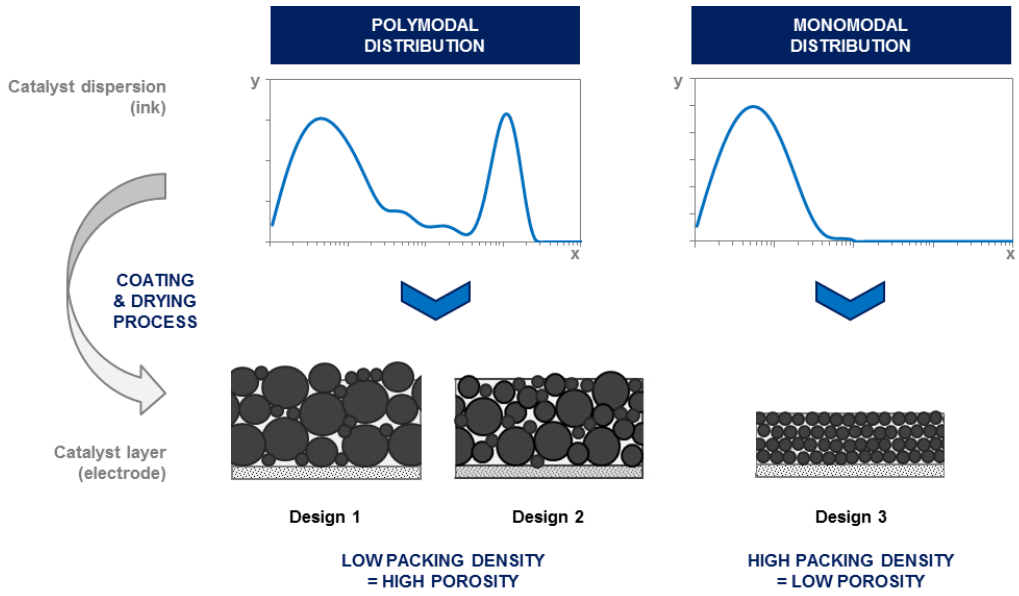

Fig. 5.33 Model description for dependence between particle size distribution modality and their resulting catalyst layer packing densities.

The transmitted light photography results in Fig. 5.32 (B) are not further considered due to the technique's CL thickness dependence: the design 3 sample presents more transmission which is correlated to the CL thickness. Thus, comparability of TLP results is only valid in between design 1 and 2 where no difference could be detected.

5.3.2.2 Pore size analysis using gas sorption technique

Fig. 5.34 illustrates typical adsorption–desorption cycles of nitrogen isotherms for a common fuel cell catalyst powder (A) and manufactured cathodic catalyst layers (B). Both isotherm types could be identified as type IV according to IUPAC classification. Their characteristic hysteresis loop demonstrate different types, meaning in detail H3 type for the catalyst powder (Fig. 5.34, zoom in A) and H2 type for the manufactured electrodes (Fig. 5.34, C) whereas electrode design 3 presents H4 type (Fig. 5.34, D).

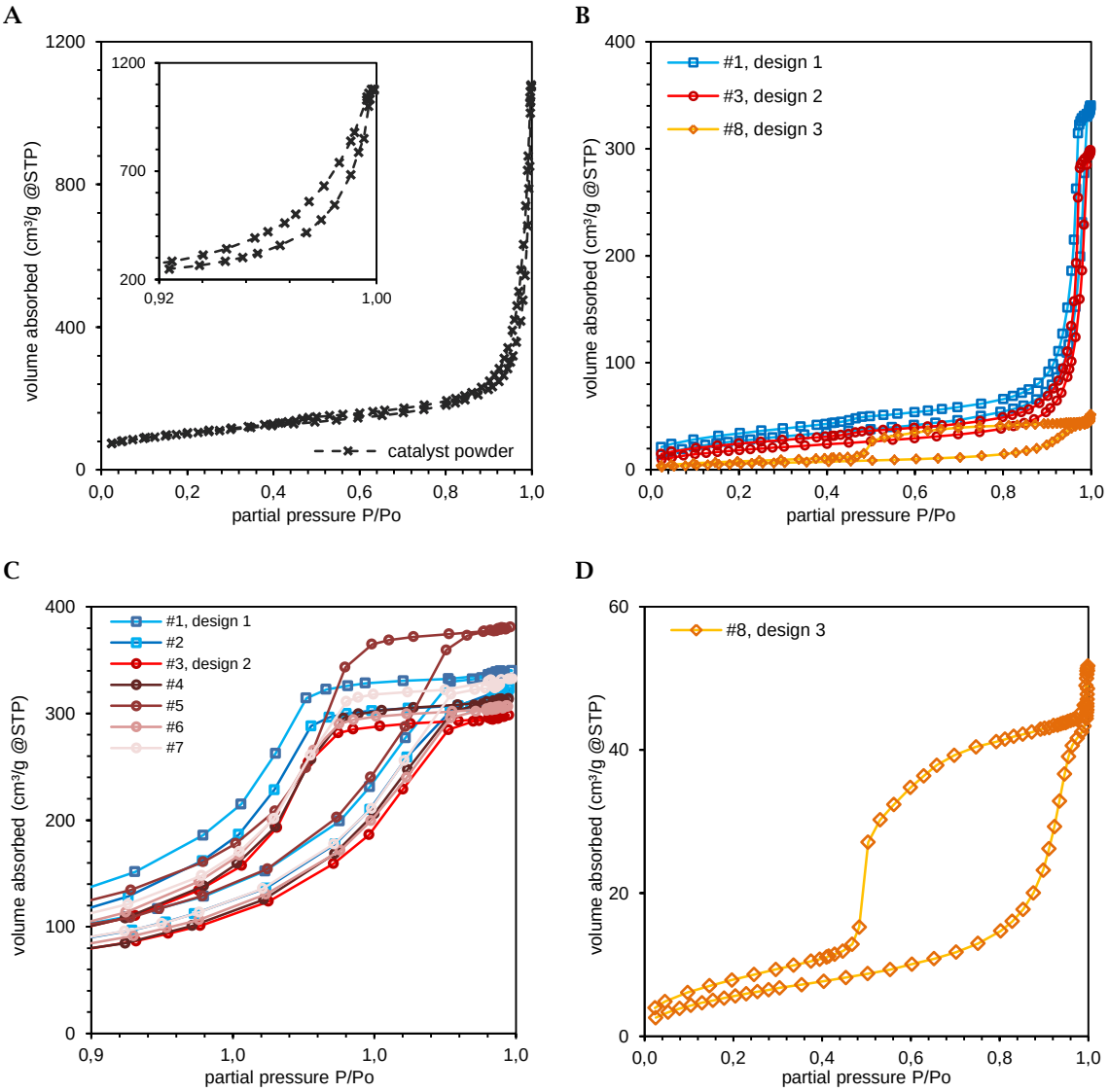

Fig. 5.34 Nitrogen sorption isotherm for catalyst powder (**A**) and manufactured electrodes (**B**). Plot **C** and **D** illustrate the corresponding hysteresis loops classified as H2 and H4 type, respectively.

H2 hysteresis loops are described by a linear range within high partial pressures indicating network pores which are causing pore blocking effects. Furthermore, the pore size distribution and pore shape are not clearly described. In contrast, H3 hysteresis loops demonstrate an absence of an adsorption limit which is correlated to slit-shaped pores.[72,78] Additionally, the H3 and H4 hysteresis loops present a steep region associated with a hysteresis loop closure resulting from the tensile strength effect in the range of 0.4 – 0.45 P/P_0 for nitrogen at 77 K whereas the H4 type also includes micropores.[72,99,100] Regarding the measured sorption isotherm in Fig. 5.34 (D) the hysteresis closure point is experimentally observed at 0.5 P/P_0 which is corresponding to the mentioned pore condensation effect. Usually within bottleneck pores the liquid evaporation depends on the pore neck diameter. In contrast, the tensile strength effect occurring within slit shaped pores depends on the nature of the adsorptive, the temperature, and the tensile strength of the capillary condensed liquid. When the mechanical stability is limited, below which the macroscopic meniscus cannot exist, a spontaneous evaporation of the liquid takes places – known as tensile strength effect.[72] Thus the steep region within the sorption isotherm does not represent a desorption phenomenon. As a result, the calculated PSD using the desorption data contains a measurement artefact. Hence, the adsorption data is recommended in order to calculate a PSD curve which is known to be more realistic when spontaneous evaporation effects appear.[72,99,100]

Moreover, the advanced pore network characteristics postulated by Seaton et al.[81] are illustrated in Fig. 5.35. Regarding the mean coordination number, Z, design 1 and 2 could not be

differentiated and the sample's values ranging in between 3.0 and 3.4 matching the preliminary result for a catalyst layer containing an I/C ratio of 1.10. Contrary, design 3 was insufficient for network characteristics calculation due to its hysteresis loop shaping. A similar picture is obtained from linear dimension analysis where a precise separation between design 1 and 2 is impossible. Hence, sample 4 shows the lowest linear dimension of 5.3 followed by sample 5 and 7 with 5.8 and 5.9, respectively. The samples 1–3 are ranging in between 6.5 until 6.9 while sample 6 presents the highest linear dimension of 7.9. A clear trend corresponding to their catalytic ink particle size distribution could not be identified.

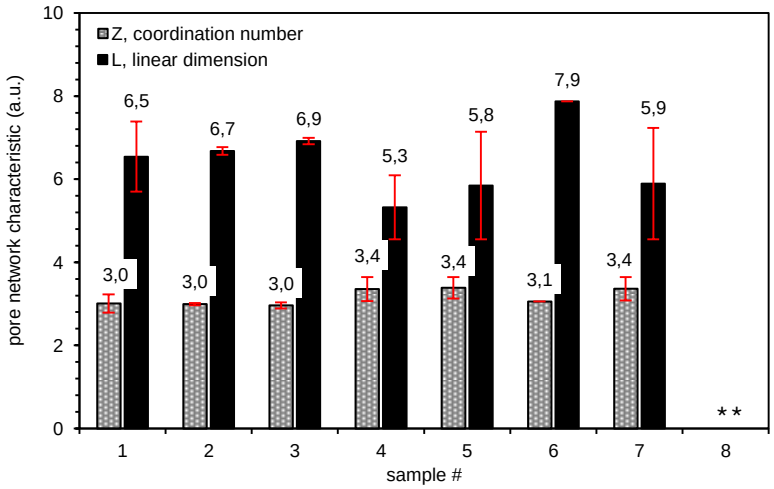

Fig. 5.35 Pore network characteristics obtained from the advanced pore network model proposed by Seaton et al.[81]

BET surface area analysis yielded averaged 76 m^2/g for design 1 and 2 (Fig. 5.36). Sample #1 and #5 show the highest values with 92.3 m^2/g and 92.6 m^2/g while sample #4 and #6 present significantly lower surface areas of 63.9 m^2/g and 61.7 m^2/g, respectively. Contrary, design 3 shows the lowest obtained surface area of only 20.4 m^2/g. Corresponding trends were observed also for QSDFT analysis (Fig. 5.36). The prior sample categorization based on the catalytic ink particle size distributions could not be verified for the resulting electrodes. This can be an indicator that some additional factors could influence the drying process and therefore the microstructure composition. Referring to the optical characterization results no significant differences could be detected: even the catalytic ink particle size distributions did not provide any explanation (Fig. 5.37). It is hypothesized that the ionomer itself – meaning the catalyst coating thickness – or its rheology are responsible for diverse film formation which could not be verified with the applied characterization techniques here.

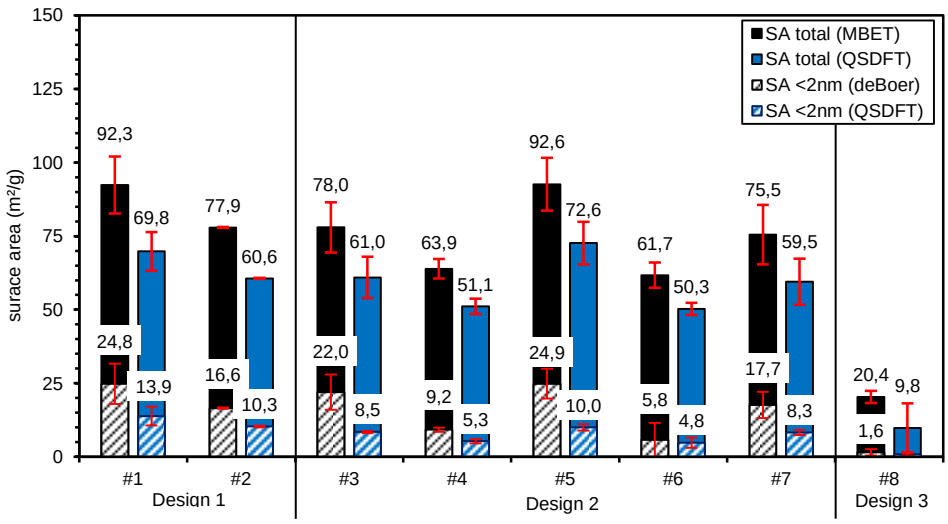

Fig. 5.36 BET surface area for manufactured catalyst layers clustered by their corresponding catalytic ink particle size distribution.

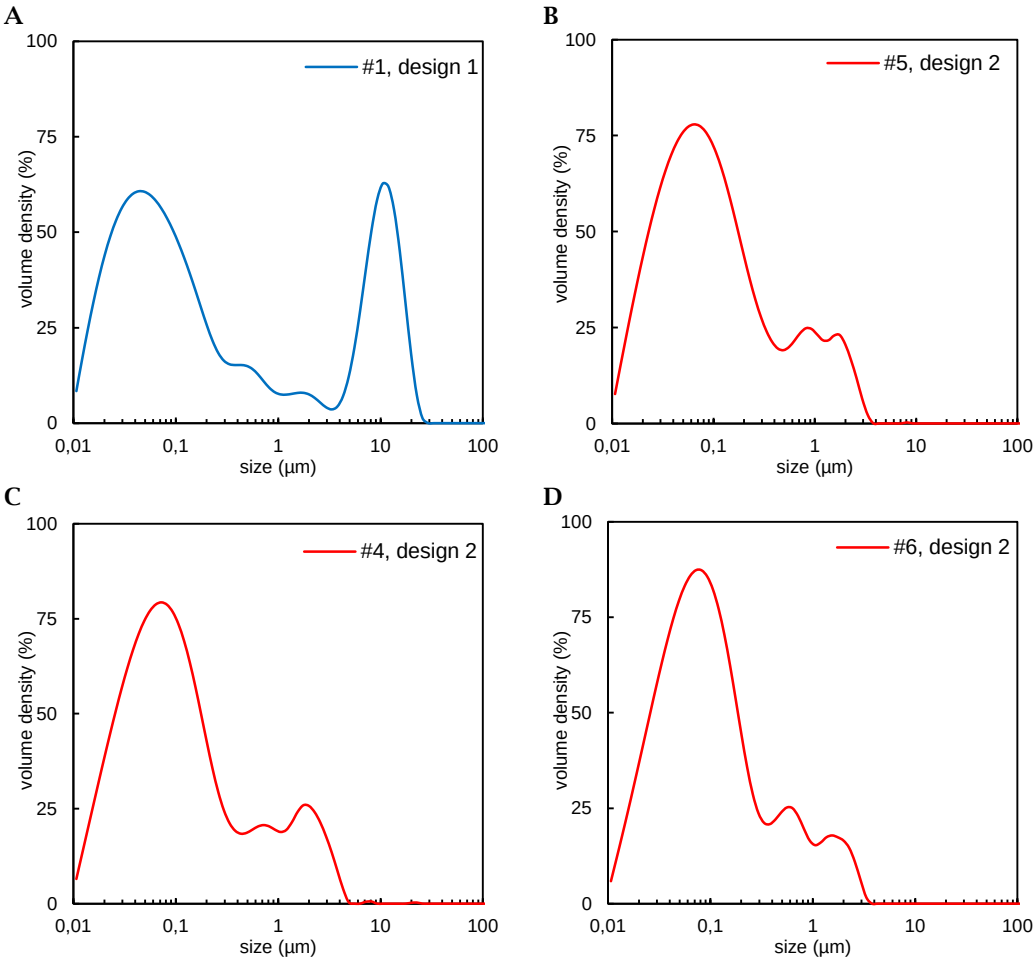

Fig. 5.37 Particle size distribution diagrams for noticeable samples: #1 and #5 indicating higher BET SAs (**A, B**) and lower BET SAs obtained for samples #4 and #6 (**C, D**).

A
high BET SA samples:

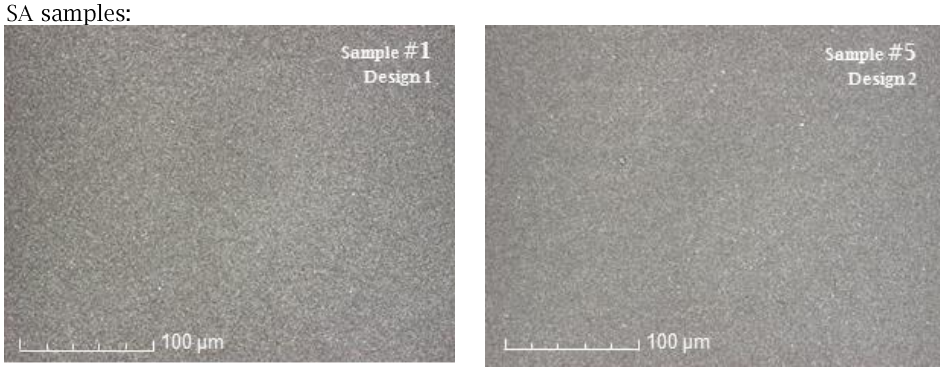

B
low BET SA samples:

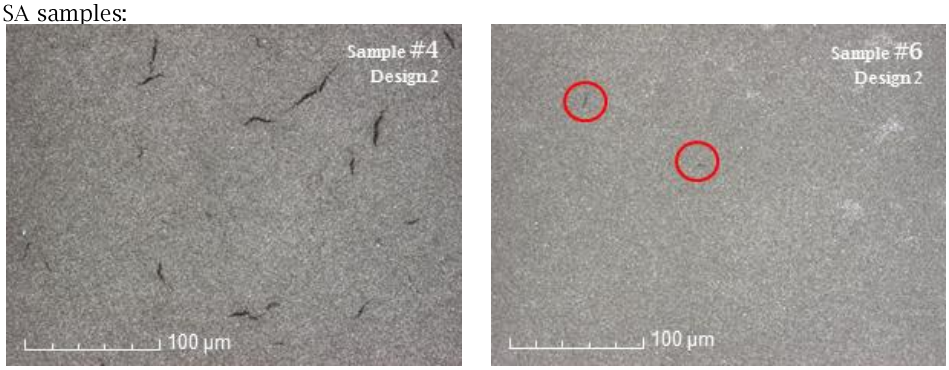

Fig. 5.38 2D laser confocal images for electrode samples #1, #4, #5, and #6, categorized into their corresponding BET surface areas high (**A**) and low (**B**).

Regarding sample #4 and #6, which present a ~30 % reduced BET surface area compared to sample #1 and #5, a particle size distribution based explanation is not feasible. The distribution shapes follow the prior sample categorization so that only sample #1 was expected to yield a higher BET SA (Fig. 5.37). Regarding the optical characterization results, catalyst layer defects are detected: Fig. 5.38 demonstrates cracks for the electrode samples #4 and #6. These results match the prior mentioned high surface roughness for both samples of 0.52 µm and 0.36 µm for sample #4 and #6, respectively (s. Fig. 5.31). However, the causes of crack evolution during catalytic ink coating could not be fully understood by using the applied characterization techniques. Even though, their particle size distributions yielded no indication for explanation. Thus, film formation affects such as catalyst ink rheology or solvent system evaporation effects are feasibly responsible for this phenomenon.

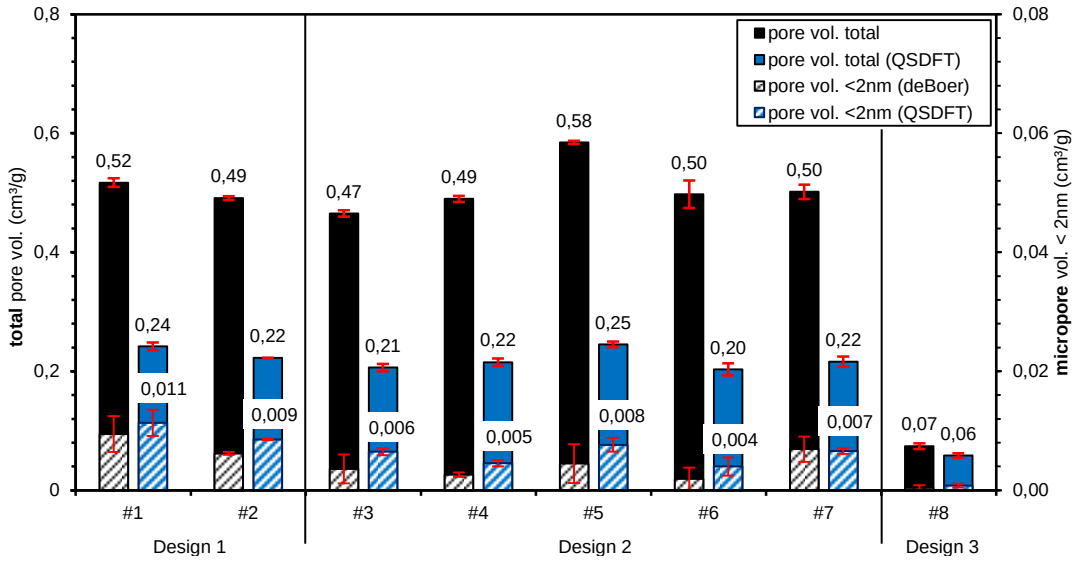

Fig. 5.39 Total pore volumes for manufactured catalyst layers obtained at 0.998 P/P_0 and using the QSDFT model.

Total pore volume analysis at 0.998 partial pressure follow the previous drawn picture: design 1 and 2 present equal total pore volumes with averaged 0.51 cm^3/g while design 3 is characterized by the lowest obtained pore volume of 0.07 cm^3/g. Here, sample #5 showed also the highest pore volume which could be reproduced by applying a second analysis model (QSDFT; Fig. 5.39). Furthermore, the statistical QSDFT approach allowed some more detailed analysis with respect to the micropore volume (pores < 2nm) which is more accurate than the classical method postulated by de Boer. However, design 1 presents the highest micropore volume with averaged 0.010 cm^3/g for sample #1 and #2 while design 2 samples (#3–#7) show an averaged pore volume of 0.006 cm^3/g. The micropore volume obtained from QSDFT analysis for design 3 (sample #8) is negligible and even its total pore volume is significant smaller compared to all other designs. Concluding, the micropore analysis allows the sample classification into the 3 designs extracted from their initial particle size distribution shapes.

For pore size distribution (PSD) analysis, BJH method was applied and yielded a sensitive differentiation between all three designs. Regarding the desorption data plot in Fig. 5.40 A, design 1 samples (#1, #2) present a more catalyst powder like PSD indicated by the development of peak 2 (~30 nm) which is also found within the catalyst powder distribution. Design 2 demonstrates only two main peaks within micro/mesopore (peak 1: ~3 nm) and macropore region (peak 3: ~60 nm). An outlier within design 2 is observed for sample #5 whose peak 2 is shifted towards greater pore diameters so that the peak's maximum can be found at 75 nm pore diameter (Fig. 5.40, B right). This finding covers the highest BET SA and pore volume values for sample #5. However, the desorption data set of design 3 is not analyzable with the BJH method due to measurement artefacts owed by the tensile strength effect.

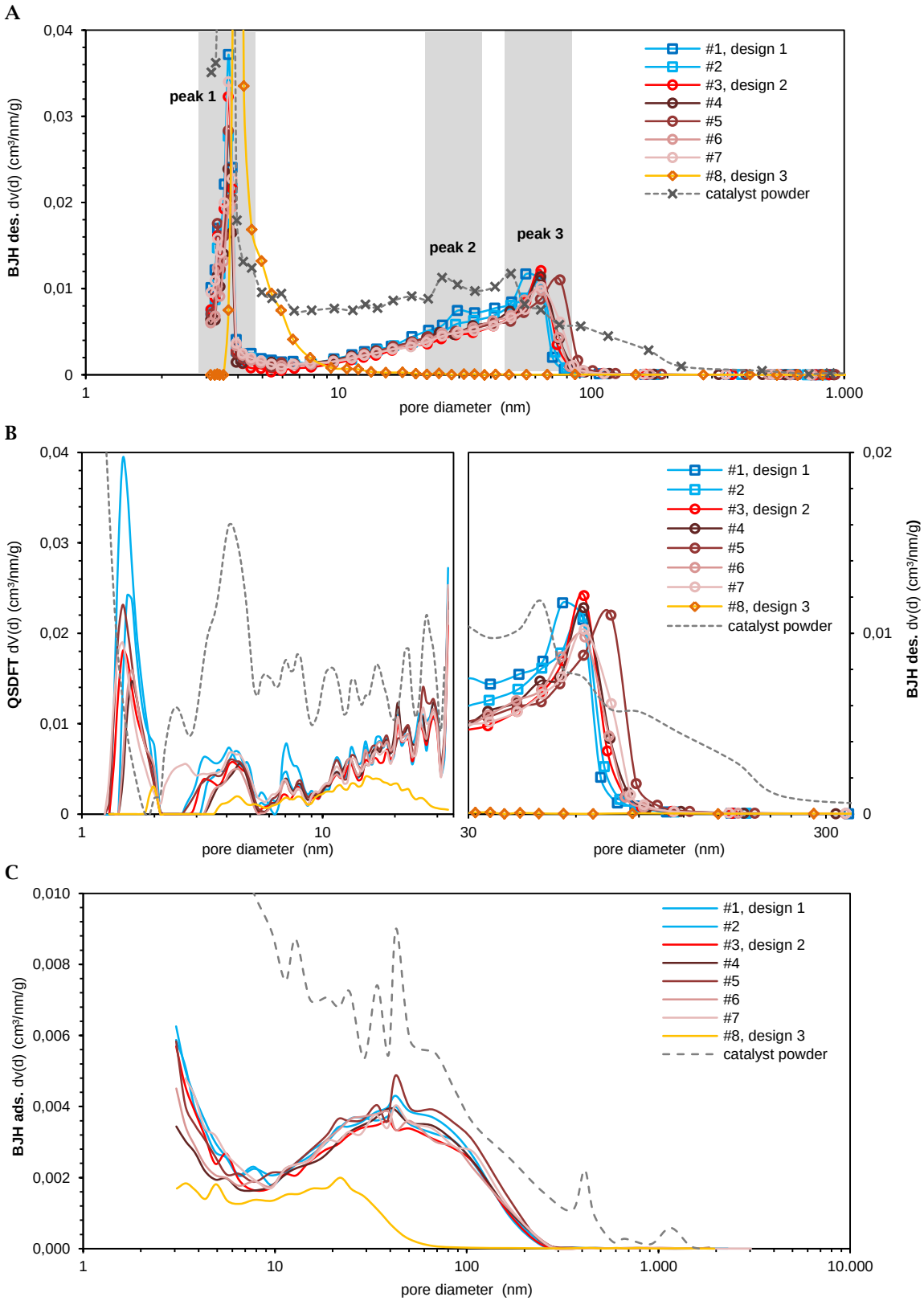

Fig. 5.40 Pore size distribution for manufactured catalyst layers obtained from BJH analysis using desorption data (**A**). The PSD plot obtained from QSDFT analysis (**B**, left) presents further details in between 1–30 nm pore diameter while meso- and macropores should be illustrated by the BJH model (**B**, right). An additional PSD plot obtained from the adsorption data set provide pore size information for sample #8 which contains mainly slit shaped pores.

Additional QSDFT analysis allowed some deeper understanding of the micropore region: as mentioned before the manufactured electrode PSD shapes follow mostly that of the initial catalyst powder (Fig. 5.40, B). Moreover, the design 1 samples (blue lines, #1 and #2) present higher adsorption values for pores <2 nm and for the peaks in between 3–5 nm and 7–9 nm. But these differences are not strongly significant and more valid for the BJH desorption plot as illustrated in Fig. 5.40, B right plot. Furthermore, the QSDFT analysis yielded a usable PSD shape for sample #8 which significantly differs from all other samples. Design 3 presents a very small pore size distribution with a maximal pore diameter of ~30 nm. All other pore size distributions show at least maximal pore diameters of ~85 nm (design 1 and 2). This finding is also in good agreement with the optical analysis for design 3 which yielded a 50 % reduced electrode thickness in comparison to design 1 and 2 electrodes. Thus, the design 3 electrode is less porous and presents a more compact microstructure. The BJH adsorption plot in Fig. 5.40 C underlines these findings so that both models – the classical and the statistical – report consistent results.

Considering optical surface appearance (Fig. 5.38, B), the presence of cracks within the catalyst layers #4 and #6 are not directly seen in the PSD plots (Fig. 5.40). Thus, the BJH plots are recalculated for a PSD log–log plot. This kind of illustration brings the advantage of direct proportionality between the peak area and the pore volume so that the relative distribution of the pore volume correlates with the single pore sizes.[74,101] As demonstrated in Fig. 5.41 additional peak maxima are obtained at ~300 nm for most samples. In contrast to a linear plot (Fig. 5.40), the logarithmic plot produces peaks which are usually overlaid by the high amount of micropores. Thus, sample #4 presents a relative pore volume fraction within the pore size of approximately 300 nm. Referring to the optical analysis, cracks were detected with average sizes of 100 µm up to 400 µm. In general, the gas sorption analysis range detects pores within 0.35 – 300 nm.[72] Hence, the optical detected cracks are not analyzable with gas sorption technique but at least the gas sorption results indicate a presence of larger macropores (> 100 nm).

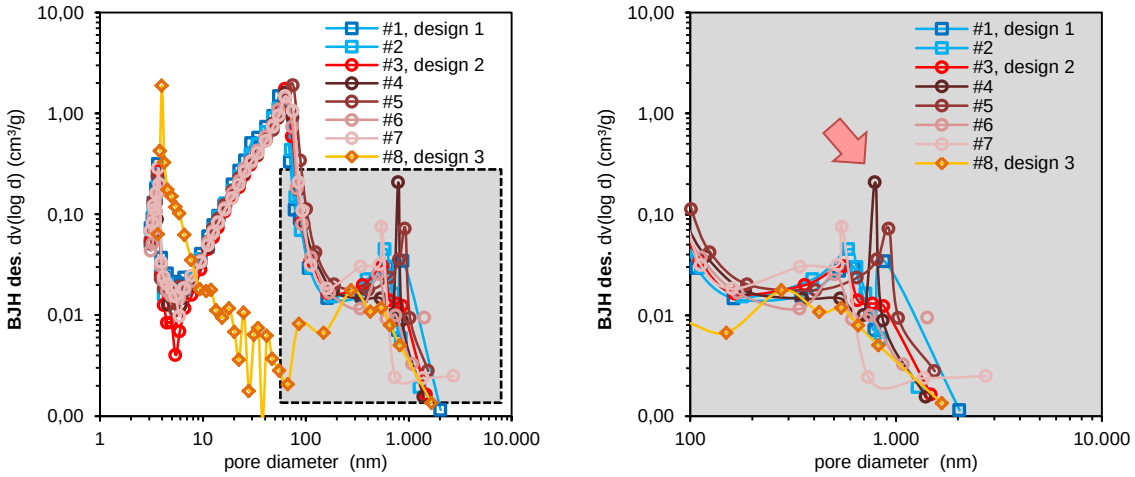

Fig. 5.41 PSD chart plotted as log–log plot for the desorption data set analyzed with the BJH model (left). The arrow within the zoom plot (right) indicates the striking peak for sample #4 which is correlated to optically detected cracks on the electrode surface.

5.3.3 Electrochemical component testing

The previously collected morphological results yielded a significant differentiation for design 3 compared to design 1 and 2. In contrast, in between design 1 and 2 a clear differentiation was not possible with the applied characterization techniques. Only the nitrogen physisorption method demonstrated different PSD shapes for all three designs. Thus, electrochemical component testing should support the decision for identification of the most sufficient catalyst layer design for normal operation condition.

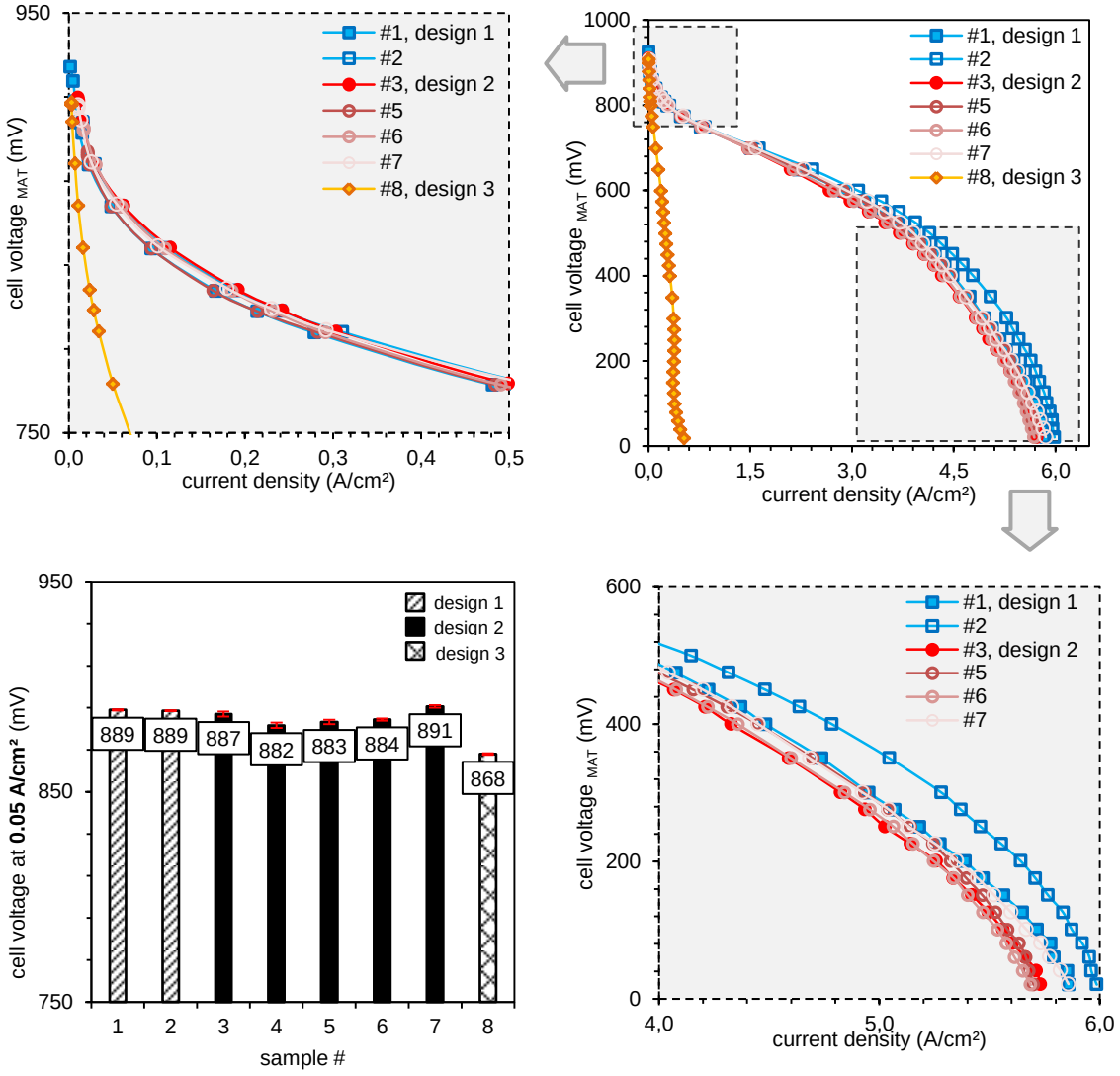

Fig. 5.42 Polarization curves obtained from applied voltages in the range of 0–1 V. Current densities were recorded at 68° C at 100 % RH. Additional OCV cleaning was performed in between the measurement points. Zoom 1 (top left) illustrate the kinetic area including corresponding cell voltages at 0.05, 0.1, and 0.5 A/cm² whereas zoom 2 (down right) depict the mass transport region.

Fig. 5.42 presents polarization curves obtained from MAT testing. It is clear, that design 1 shows higher cell performances at high current densities within the mass transport region. Referring to the morphological insights, design 1 is characterized by relative high catalyst layer porosity caused by low catalyst particle packing density which is a result from the polymodal catalyst particle distribution for the catalytic ink. These assumptions are experimentally validated by surface area and pore size distribution analysis using gas sorption technique. Thus, the catalyst layer performance seems to be directly tunable by the catalytic ink particle size distribution modality and its resulting particle packing density. Fig. 5.43 illustrates representative particle size distributions for all three prepared catalytic ink designs. Moreover, design 2 samples reflect slightly lower cell performances within the range of 3.0 – 6.0 A/cm² (Fig. 5.42). In contrast, design 3 is electro-

chemically active but respecting the low cathodic catalyst layer porosity its performance demonstrates a straight breakdown. Several characteristics are responsible for this cell behavior: first the prior mentioned low catalyst layer porosity which causes dramatic mass transport issues. On the other hand, the slit shaped pores produce spontaneous evaporation phenomena so that liquid oxygen is inhibited and forced to stay within the pores so that in turn the mass transport issue is enhanced. Finally, the cathodic catalyst layer is completely blocked and cell operating breaks down. Thus, design 3 is not recommended as sufficient cathodic catalyst layer design for normal cell operation. Design 2 and 1 present sufficient cell performances whereas design 1 catalyst layers should be superior used. But it should be further noted that higher porous CLs tend to react sensitive to degradation mechanism.[102] Degradation studies are not included here but it is recommended to include them for final decision between design 1 or 2.

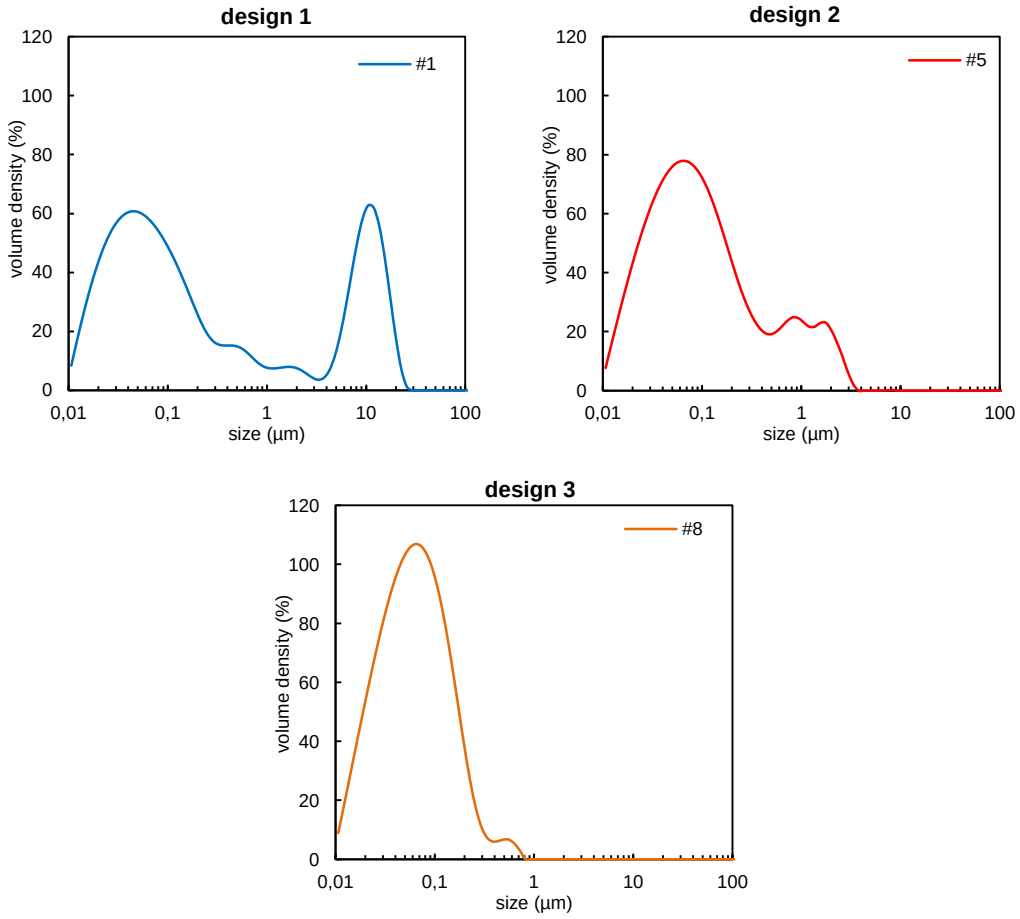

Fig. 5.43 Representative particle size distributions for catalytic inks after terminating the mixing process.

Moreover, differences between design 1 and 2 within the kinetic region are not measureable here. Both, the polarization curve recording as well as the fast transient polarization (FTP) data recorded at 0.05 A/cm² yielded no significant difference. Only design 3 differs significantly from the other designs (Fig. 5.42, top left and down left).

Further validation for design 1 cell performance superiority was achieved by CAT testing application. The selected representative samples follow the previously drawn picture as illustrated in Fig. 5.44: within higher current densities (at 2.4 A/cm²) the difference becomes more significant with approximately 21 mV in between design 1 and 2. Regarding the steady state point measurements at 1.7 A/cm² the design differences become minimized for both MAT and CAT testing (Fig. 5.45). In general, the CAT testing results present 9 % lower cell voltages for normal conditions (NOC) and 6 % lower cell performances for hot conditions compared to MAT results. Considering stack estimation at least CAT testing results should be taken into account due to their more realistic geometry and flow field.

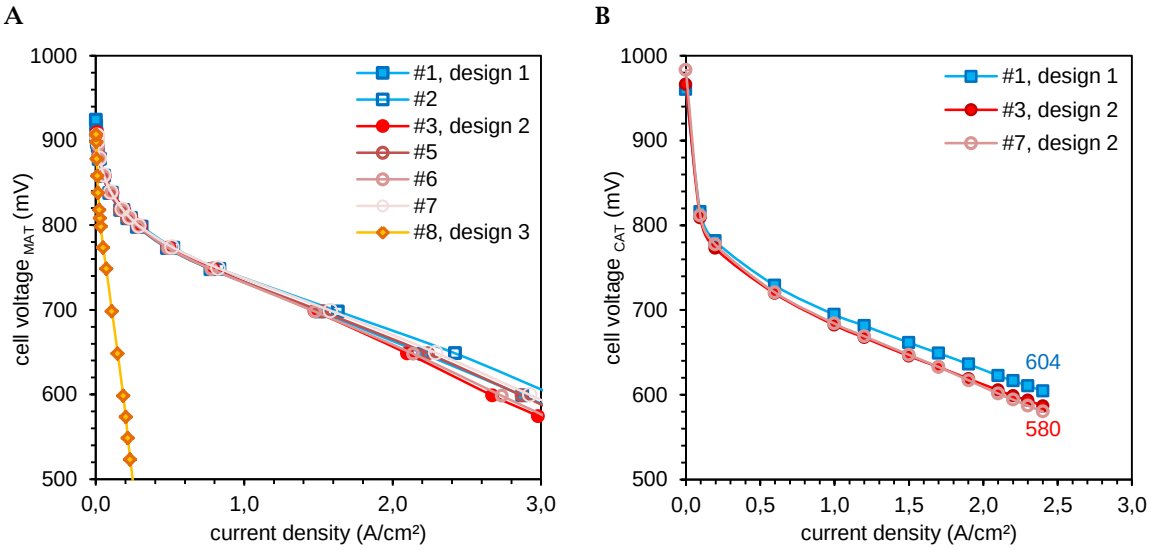

Fig. 5.44 Polarization curves obtained from **(A)** MAT testing station using circular 3 cm² active area and **(B)** CAT testing station operating with rectangular sampled active area of 40 cm². Cell performances are recorded at 68° C at 100 % RH.

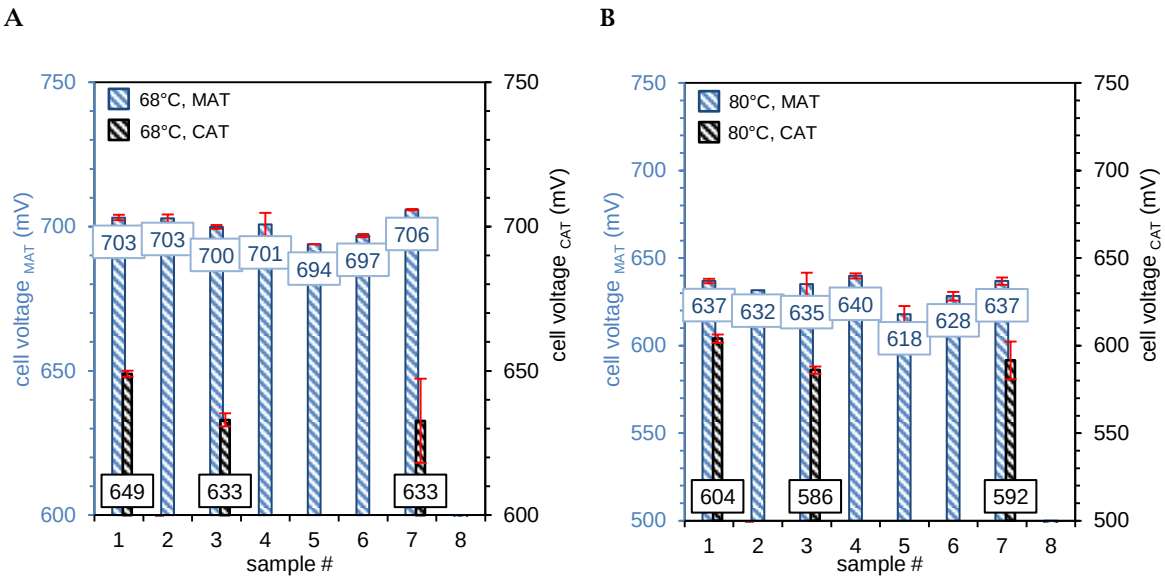

Fig. 5.45 Steady state results for normal **(A)** and hot **(B)** conditions recorded with MAT and CAT at 1.7 A/cm².

In order to differentiate more precisely an ANOVA analysis for the MAT mean values was performed. The results are presented in Table 5.2. For both operation conditions, NOC and HOT, design 3 is significantly different from the other designs presenting its own group number (D for NOC and B for HOT). The grouping within NOC mean values is non consistent: on the one hand both design 1 samples (#1, #2) present similar grouping (AB) but on the other hand sample #4 of design 2 also belongs to group AB. Referring to the morphological analysis results, sample #4 contains cracks within its catalyst layer surface as well as presenting a relatively low surface are of 64 m²/g. Thus, the cause for the relatively high cell performance of sample #4 could not be identified but it could be assumed that the presence of cracks could rise the cell performance.[20] It should be also noted that the cell performances generally not differ significantly. Contrary, the ANOVA grouping for the hot operation condition for design 1 and 2 are consistent. Thus, MAT and CAT testing are not able to demonstrate verified identification for the most sufficient cathodic catalyst layer design for normal and hot operating conditions so that further electrochemical

testing is recommended. Due to constant raw materials and only process related variations slight changes are expected and experimentally achieved. Small differences in between the catalytic ink properties and their corresponding electrodes are challenging for detection. In contrast, a change within the catalytic ink particle size distribution modality, for example from polymodal to monomodal, and its resulting morphological impact during the layer formation process is clearly measureable by the applied characterization techniques. Thus, a lower limit for cathodic catalyst layer functionality is found with design 3 which leads to rapid cell performance breakdown which is not sufficient for automotive fuel cell application and therefore not recommended for usage within the catalyst layer design process.

Table 5.2 Characteristics obtained from ANOVA analysis of the means for MAT.

Sample #	design	mean (NOC)	ANOVA grouping (NOC)	mean (HOT)	ANOVA grouping (HOT)
1	1	703	A B	637	A
2	1	703	A B	632	A
3	2	700	B	635	A
4	2	701	A B	640	A
5	2	649	C	618	A
6	2	697	B C	628	A
7	2	706	A	637	A
8	3	−2	D	312	B

5.3.4 Conclusion

In the literature the catalyst agglomerate diameter is identified as one of the main influential parameter for the cell performance.[20] During this work it is hypothesized that there is a direct correlation in between the catalytic ink particle size distribution and the cell performance. In order to validate this hypothesis, diverse catalytic inks were synthesized which contain different particle size distribution shapes and a wide range of distribution widths. The complete cathodic CL production process from catalytic ink over catalyst layer and finally the CCM was analyzed by application of a range of characterization techniques. First, all catalytic inks were classified into the intended designs of which each is presenting specific properties such as polymodal particle size distribution equally illustrating aggregated dispersion state (design 1) or contrary completely monodispersed particles demonstrating Mie scattering and monomodal size distribution (design 3). Second, the next processed product, the catalyst layer (CL), could not be categorized into the three designs by application of optical surface analysis techniques and BET SA analysis including total pore volume analysis except for the statistical QSDFT approach which is able to analysis the micropore region. However, most characterization methods yielded similar results for design 1 and 2 while design 3 was clearly identified as significantly different. These findings could be correlated to its monomodal catalytic ink particle size distribution resulting in a high particle packing density which in turn presents low CL porosity directly measurable with nitrogen physisorption method. Furthermore, a 50 % CL thickness reduction was detected in comparison to design 1 and 2. Thus, it could be concluded that the catalytic ink particle size distribution modality determines the solid skeleton of the CL during catalytic ink drying process. It is not only the solid catalyst agglomerate diameter but also the distribution of particles/agglomerates and the ratio of small to large particles which determine the CL microstructure. The solid CL skeleton is directly tunable by catalyst particle size distribution adjustment. The created void space is then further penetrated by the ionomer itself or its catalyst coating thickness which also depends on the solid catalyst agglomerate diameter and the created pore sizes. It is literature known that only pores greater than 20 nm are available for ionomer distribution and the less surface area is available the thicker the ionomer coating layer is created.[17,46] Hence, design 3 presents a highly compact CL structure which is favored for diffusion pathways but simultaneously bear the risk of mass transport issues. Gas sorption experiments yielded a H4 type hysteresis loops which is characterized by a hysteresis closure caused by spontaneous evaporation – literature known as the tensile strength effect of capillary condensed liquid.[99,100] Moreover, the presence of slit shaped pores is responsible for a rapid cell performance breakdown so that this microstructure design 3 for ca-

thodic catalyst layers is not recommended. In contrast, design 1 and 2 demonstrate similar cell performances whereby design 1 presents slightly higher cell performances especially during high current densities within the mass transport region. Considering the BJH analysis results obtained from gas sorption experiments, a feasible explanation is found: only the design 1 samples show a more catalyst like PSD curve by containing three main peaks which were also found within the catalyst powder PSD curve. This difference could be correlated to an aggregated dispersion state because both design 1 samples (#1, #2) are indicated by a D*f* value greater than 1 which was induced by a prolonged catalyst wetting time so that the solvent system can penetrate the catalyst powder more intense. But still, design 1 yielded H2 type hysteresis loops which are identified as typical characteristic for manufactured catalyst layers presenting mesoporous material. Referring to the reduced cell performance for design 3 – which mostly contains micropores and narrow mesopores – it could be assumed that greater mesopores (> 30 nm) are crucially essential for sufficient fuel cell performance. Comparing design 1 and 2, the pore structure of design 1 must be more efficient for mass transport which is not fully validated with the applied characterization techniques. The lacking detection range in between gas sorption and optical analysis (>300 nm up to several microns) is recommended for investigation within future experiments. Concluding, the main identified characteristics influencing the cell performance are the particle size distribution modality, the D*f* value for the catalytic ink, and the hysteresis loop of the gas sorption isotherm for catalyst layers. All other findings could be correlated to those characteristics. Thus, the main differences are achieved between mono– and polymodal catalytic ink particle size distributions, aggregated or non–aggregated dispersion states, and hysteresis loop classes such as H2 (mesoporous, manufactured CL), H3 (microporous, catalyst powder), and H4 (microporous with capillary evaporation effect). In order to design a sufficient cathodic catalyst layer, polymodal catalyst particle size distribution including a D*f* value slightly greater than 1 (aggregated) and a H2 type hysteresis loop for a type IV isotherm for the catalyst layer are recommended as typical morphological properties.

5.4 Discussion: Do the ink property settings determine the electrode microstructure independent of the deployed mixing technology?

The previously collected results draw a clear picture for the correlation between the catalytic ink mixing properties and the resulting cell performances of the manufactured catalyst layers. Therefore the process mixing time, the applied I/C ratio, as well as diverse CL designs were consecutively varied and synthesized. Here, the catalytic ink particle size distribution modality as well as the D*f* value and the catalyst layer hysteresis loop obtained from nitrogen sorption experiments were identified as main influential parameter determining the CL microstructure. Thus, a diverse mixing technology supplying higher energy inputs should be applied in order to produce a catalytic ink with similar or at least comparable ink properties. The I/C ratio (1.10), mixing time (7 days), and solid content (9.0 %) are kept identical. The goal is set to create a particle size distribution below 2 µm as maximal diameter. As illustrated in Fig. 5.46 the goal is reached for both applied technologies (Tech 1 versus Tech 2) for all SLS characteristics: the volume-weighted mean is found to be equal with ~0.23 µm and the relative amount of small particles presented 22 % for Tech 1 and 29 % for Tech 2, respectively. Even the internal structure analysis results match each other and demonstrate non-aggregated dispersion states with D*f* values of 0.16 and 0.15.

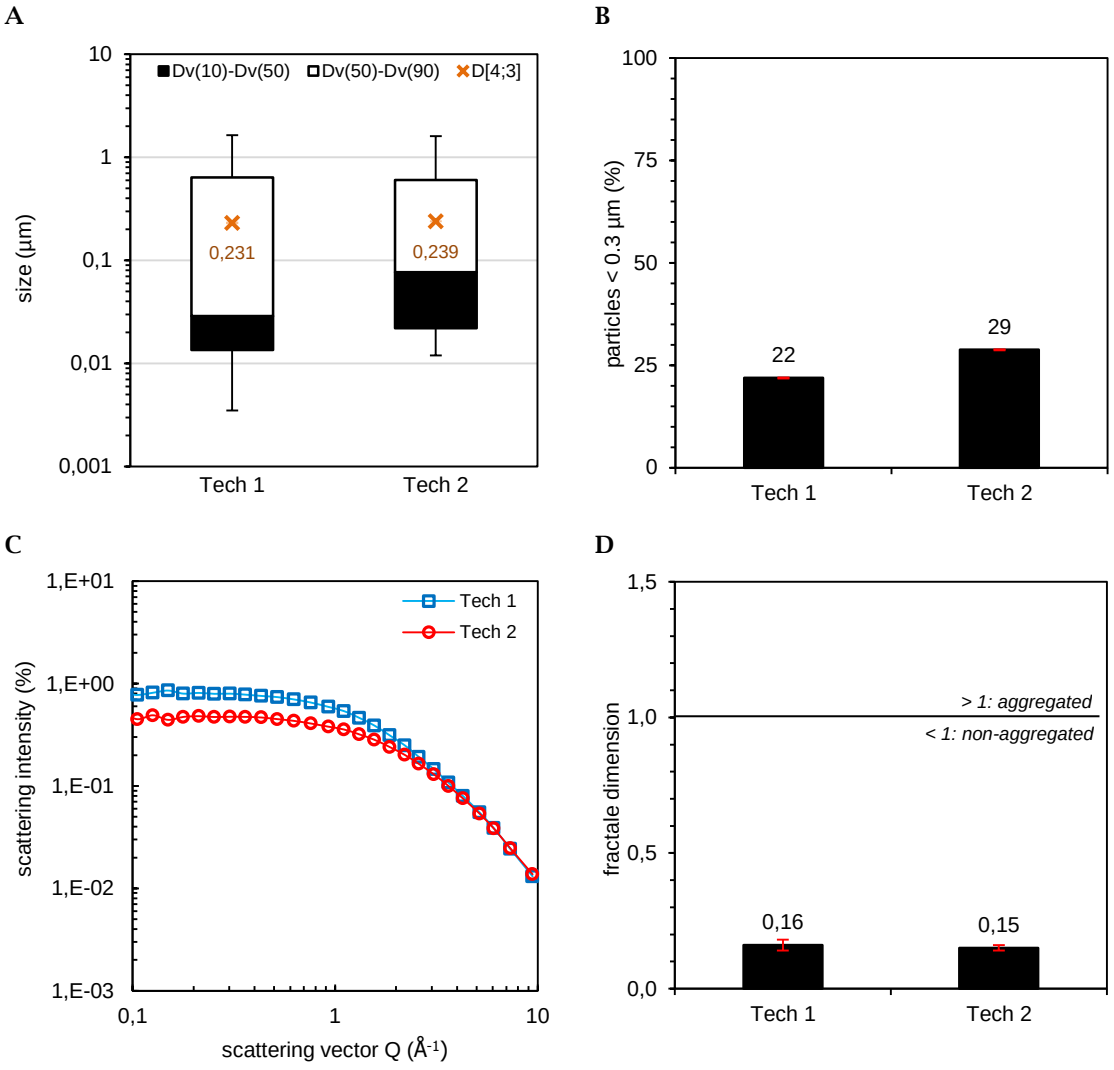

Fig. 5.46 Catalytic ink particle size distribution characteristics obtained from SLS analysis: **(A)** boxplot of the particle size distribution, **(B)** relative amount of small particles, **(C)** log-log plot of the internal structure analysis and its corresponding D*f* values indicating the dispersion state **(D)**.

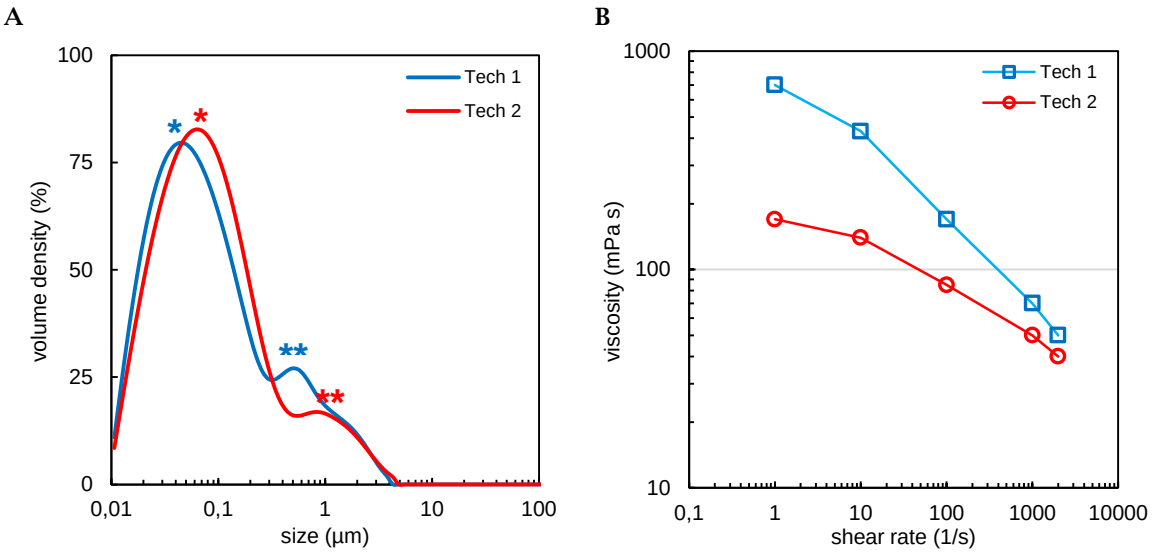

Fig. 5.47 (A) Particle size distribution for catalytic inks prepared with Tech 1 and Tech 2. **(B)** illustrates the rheological properties of the two catalytic inks.

Although the characteristics obtained from SLS analysis present comparable catalytic inks a detailed look on the particle size distribution demonstrates some significant differences (Fig. 5.47). The Tech 1 particle size distribution curve contains two peaks and a shoulder whereas the size distribution curve of Tech 2 contains only one distinct peak and another shoulder which overlays the one of Tech 1. The first peaks (*) of both distributions are not matching so that Tech 1's first peak maximum is found at 0.05 µm whereas the Tech 2 peak maximum resulted 0.07 µm. Furthermore, Tech 1's second peak maximum (**) is found at 0.05 µm which is extended by a peak shoulder. In contrast, Tech 2 does not develop a clear second peak maximum but instead a peak shoulder which follows Tech 1's course. Both distributions find their maximal agglomerate size at ~4 µm. Thus, both particle size distributions seem to be similar but there are some slight differences. An additional essential difference is detected by rheological catalytic ink analysis: Tech 1 catalytic ink presents a viscosity of 700 mPas at shear rate 1 s^{-1} whereas Tech 2 demonstrates a 76 % reduced viscosity of 170 mPas. For higher shear rates the difference decrease but still leave a 20 % gap. It could be assumed that the slight difference within the particle size distribution could cause the rheological property differences or if possibly the applied mixing technology and its energy input influence the catalytic ink's viscosity meaning precisely an ionomer network influence which is responded as viscosity variation.

Optical catalyst layer analysis (Fig. 5.48, A) resulted similar surface appearance for both Tech 1 and Tech 2 CLs whereas Tech 2 CL presents a slightly higher surface roughness of 0.278 µm compared to Tech 1 with 0.223 µm. Moreover, cross-sectional SEM investigations (Fig. 5.48, B) demonstrated a CL thickness difference of 1 µm in between Tech 1 CL and Tech 2 CL. Thus, Tech 1 CL is slightly thicker which is in good agreement with its particle size distribution that included a higher amount of larger particles (peak 2;**). A less particle packing density and therefore a higher CL porosity for Tech 1 CL could explain the overall higher CL thickness. Fig. 5.49 is summarizing the hypothesis of catalyst layer formation depending on the particle size distribution of the catalytic ink. The drawn scenarios resemble the previous scenario for design 1 and 2 catalyst layer formation whereas differences within the catalytic ink particle size distribution causes diverse film building. Here, it is expected that Tech 1 CL presents higher total pore volumes due to low particle packing density which should result in meso- or even macropores. In contrast, Tech 2 CL is expected to yield low electrode porosity which should be measurable by applying gas sorption experiments.

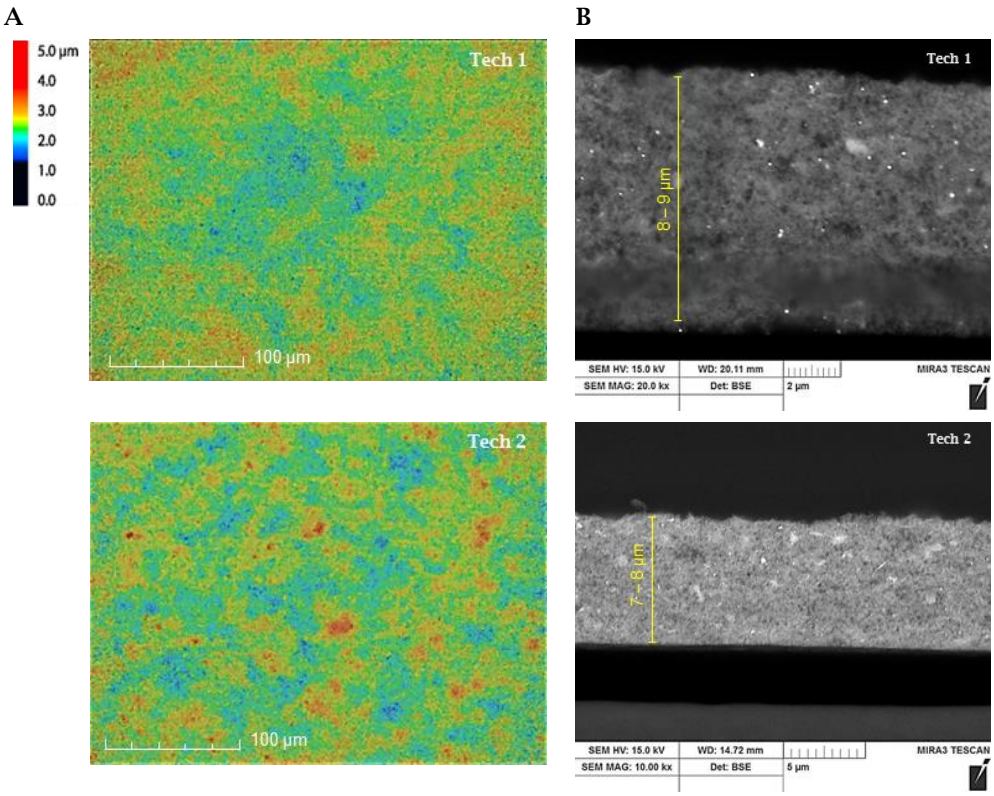

Fig. 5.48 Optical surface analysis using laser confocal microscopy and 3D imaging **(A).** SEM cross-sectional analysis yielded CL thickness and general visualization of the lateral CL texture **(B).**

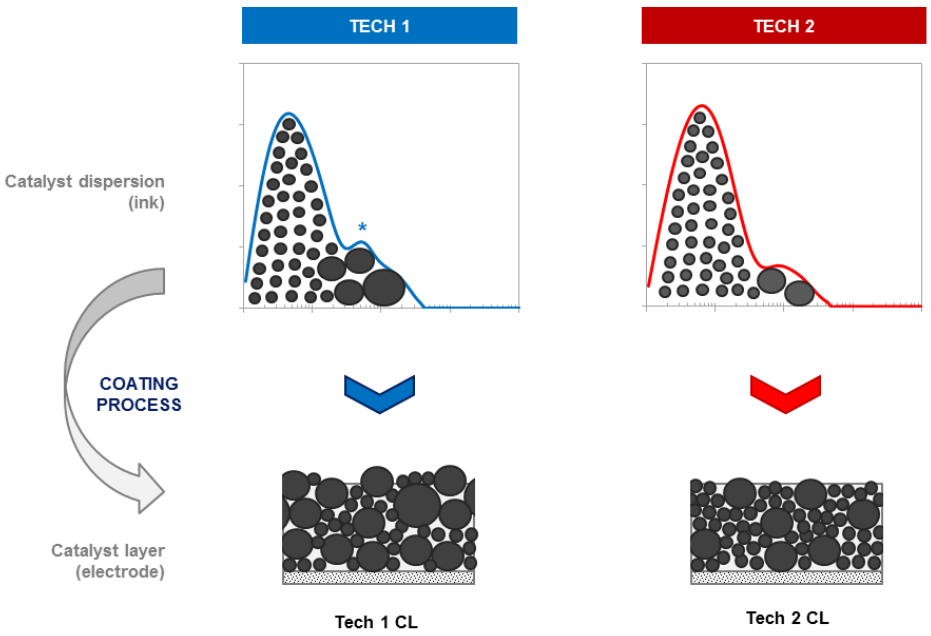

Fig. 5.49 Model description for catalyst layer formation based on the catalytic ink particle size distribution.

As illustrated in Fig. 5.50 typical nitrogen sorption isotherms are achieved for Tech 1 and Tech 2 catalyst layers. The isotherms follow IUPAC classification for isotherm shapes by demonstrating type IV and hysteresis loop type H2 (zoom in Fig. 5.50). These characteristics are literature-known for mesoporous materials and bottleneck-network pores.[72] Thus, both catalyst layers contain similar pore network structures. But as assumed by the model description for the catalyst layer formation (Fig. 5.49), Tech 1 CL presents a 12 % higher total pore volume of 0.50 cm^3/g compared to Tech 2 CL with 0.44 cm^3/g. Equally, the multipoint BET analysis resulted a 35 % higher BET SA for the Tech 1 CL of 75.5 m^2/g compared to Tech 2 CL with 48.7 m^2/g (Fig. 5.51).

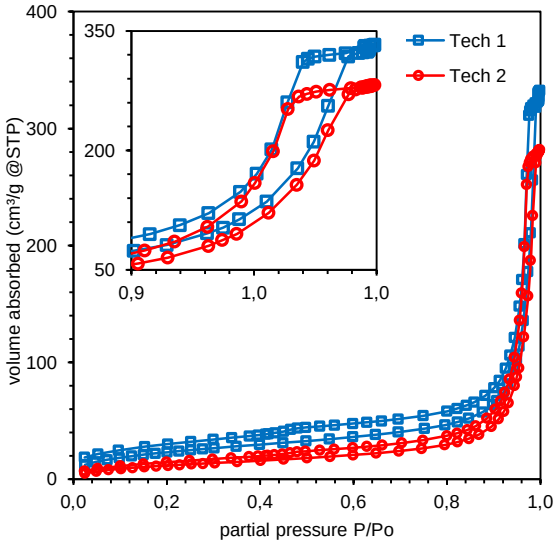

Fig. 5.50 Nitrogen adsorption-desorption cycles for Tech 1 and Tech 2 CLs. The zoom presents their hysteresis loops which follow IUPAC classification for type H2.

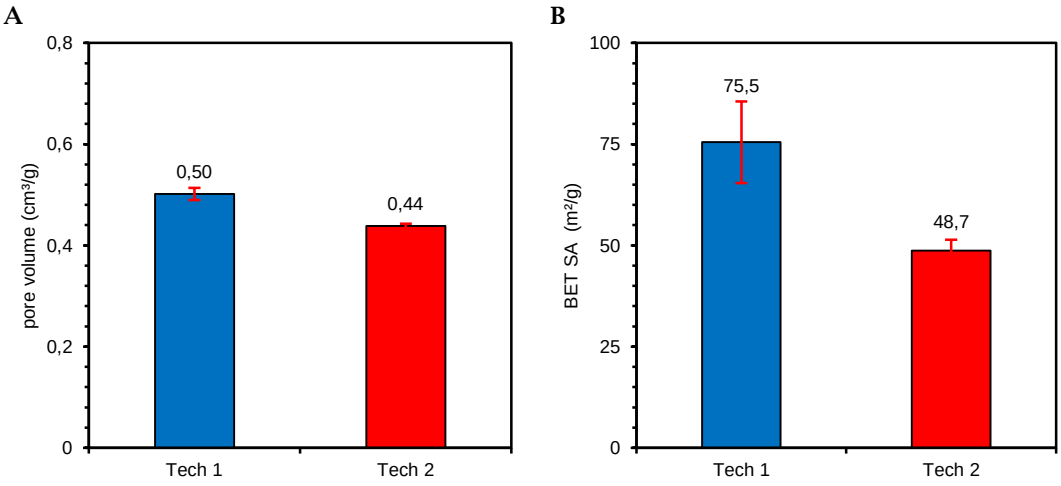

Fig. 5.51 Total pore volumes recorded at 0.998 partial pressure **(A)** and corresponding surface areas calculated from BET analysis **(B)** for Tech 1 and Tech 2 CLs.

Additional pore size distribution analysis yielded further differentiation between Tech 1 and Tech 2 CLs as illustrated in Fig. 5.52: both plots, the linear (A) and logarithmic (B) illustrate differences within the meso- and macropore region. The pore number of the corresponding pore sizes can be derived from the linear plot while the relative distribution of the pore volume to its corresponding pore sizes can be deduced from the log-log PSD plot. Hence, Tech 2 catalyst layer presents a larger number of mesopores with a peak maximum at 32 nm. Tech 1 CLs also demonstrate a peak maximum at 32 nm but also a significant lower number of corresponding meso-

pores. Recalculating the linear PSD plot into a log–log plot, produces a third peak at a pore diameter of approximately 300 nm which represents a considerably pore volume fraction. This peak (*) is only clearly developed for the Tech 1 catalyst layer (Fig. 5.52, B) which indicates the presence of larger macropores (> 100 nm). Due to the gas sorption limited detection range a further quantification is not feasible. Regarding the SEM surface images, Tech 1 CL seems to be more porous than Tech 2 CL. Combining the gas sorption and optical analysis results the proposed model for catalyst layer formation becomes more possible. As illustrated in the model description (Fig. 5.49) a higher pore volume fraction is related to macropores within Tech 1 CL compared to Tech 2 CL. Thus, the higher amount of larger agglomerates creates a porous catalyst particle skeleton which generates measureable high total pore volumes. On the other hand, Tech 2 CL is more compact yielding a lower total pore volume and an absence of (detectable) macropores which simultaneously result in a larger number of mesopores created between the solid catalyst particles. Thus, experimental data verify the theoretical assumptions.

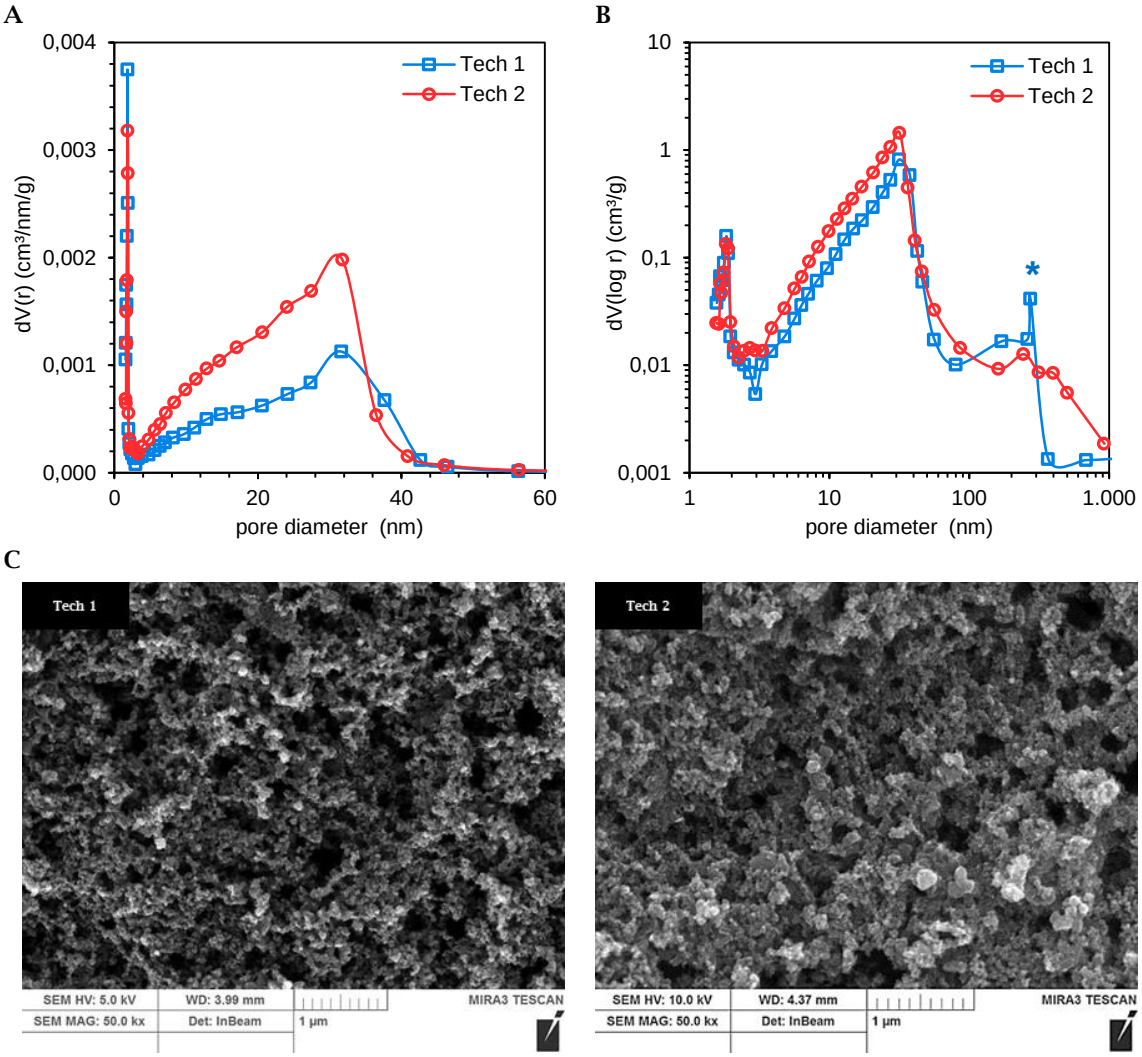

Fig. 5.52 Linear PSD plot **(A)** and log–log plot **(B)** obtained from BJH analysis using desorption data. **(C)** presents the corresponding SEM surface images for Tech 1 and Tech 2 CLs.

But another scenario is also feasible when taking the catalytic ink rheology into account: Tech 1 ink is much more viscose than the Tech 2 ink which could influence the drying process by capturing air within the solvent system leading to pore creation within the catalyst layer. Hence, a thicker catalyst layer is created. Furthermore, the network structure of the ionomer could be influenced by the applied mixing technology and its corresponding energy input so that the ionomer itself could influence the pore network development. However, the ionomer fraction constitutes only ~34 % of the solid contents whereas the catalyst held the main shares of 67 %. Thus,

the probability of solid skeleton formation determined by the catalyst particles/agglomerates is much higher than a main influence by the ionomer characteristic.

Regarding the polarization curves obtained from MAT and CAT testing (Fig. 5.53) similar results are obtained. It seems that Tech 2 CL slightly performs better than Tech 1 CL but the curves present a crossing point within higher current densities which equals the cell performances. In contrast, the CAT polarization curves demonstrate a superior performing of the Tech 1 CL. But, a clear trend is not deducible due to the small differences possibly owed to the manufacturing process or materials such as the proton exchange membrane (PEM).

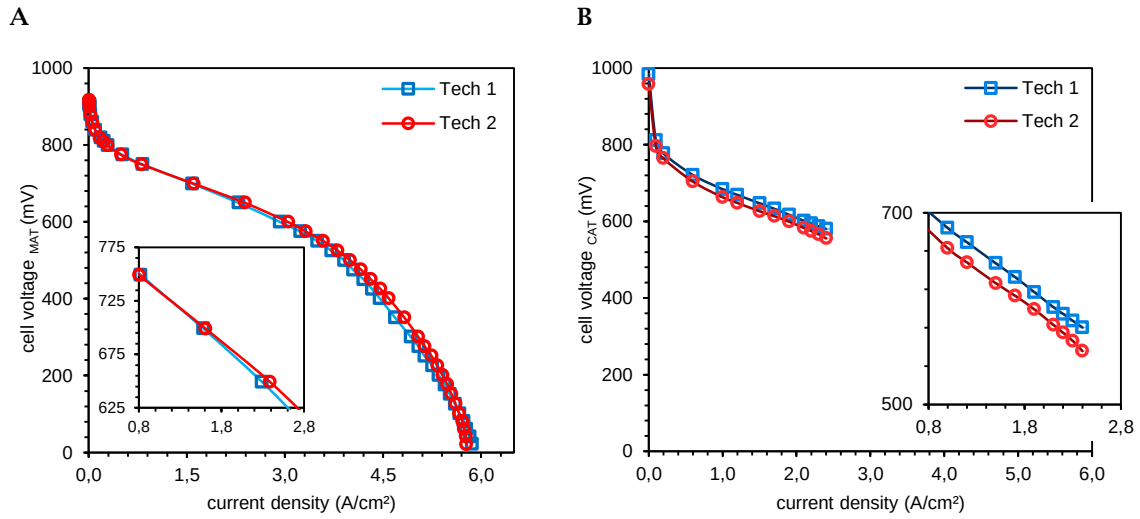

Fig. 5.53 Polarization curves recorded at normal conditions (68° C, 100 % RH) obtained from MAT **(A)** and CAT **(B)** testing.

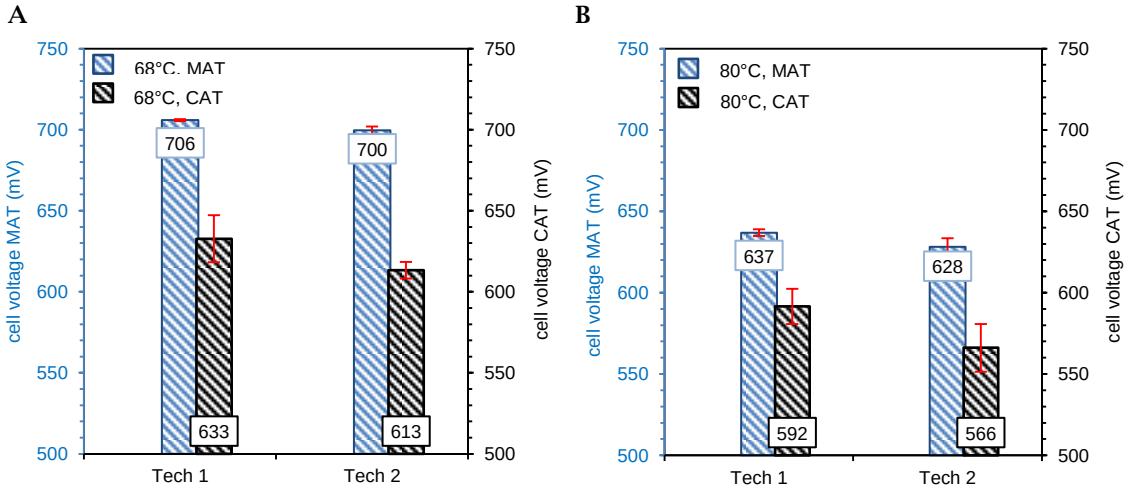

Fig. 5.54 Steady state measurement points for MAT and CAT testing recorded at 1.7 A/cm² for normal **(A)** and hot **(B)** conditions.

Taking the steady state measurement results into account more valuable information is revealed. Fig. 5.54 illustrates normal (A) and hot (B) conditions whereby in both conditions CAT testing presents 11 % and 8.5 % lower results, respectively. But still, as well as for MAT and CAT testing and normal and hot condition, Tech 2 CL yielded lower cell voltages: at normal conditions MAT testing presents a cell performance reduction of 1 % (6 mV) in between Tech 1 and Tech 2 CL while a 3 % reduction (20 mV) for CAT testing was achieved. The MAT gap matches the measurement tool error of ± 15 mV which indicates a non-significant difference. Furthermore, the MAT

testing difference at hot condition is also negligible (1 %) but also the CAT testing differences for Tech 1 and Tech 2 CL demonstrated a 26 mV difference (Fig. 5.54, B). Considering CAT testing as more realistic testing method, it could be assumed that the Tech 1 CL performs slightly but significantly better than the Tech 2 CL. Referring to the morphological analysis results, a higher CL thickness, porosity as well as the indication for the presence of larger macropores could be identified as responsible characteristics. All these findings are hypothesized to be determined by the catalyst particle skeleton which is build up from the catalytic ink during catalyst layer formation. The detection of the small differences is challenging using the applied optical characterization techniques so that more precise methods are recommended. Even the electrochemical testing should be repeated and extended with measurements focusing the mass transport region cell performance. Thus, the initial question of catalytic ink equality independent of the deployed mixing technology could not be precisely answered due to the fact that the processed catalytic inks do not presented absolute comparability: Tech 1 catalytic ink demonstrated a more polymodal related particle size distribution whereas the Tech 2 ink presented a bimodal particle size distribution (Fig. 5.47, A). The Tech 2 distribution is missing a clearly developed peak of approximately 0.5 µm possibly reduced in benefit for a higher amount of smaller particles (< 0.3 µm). Thus, the applied energy input is higher which means in turn a more efficient particle size reduction. The presented investigation validates the previously drawn model for catalyst layer microstructure formation. Furthermore, the experimental results give some further insight into unknown characteristics such as the catalytic ink rheology. Usually, at constant volume fractions a decrease in particle size reduction leads to an increase in viscosity. But here, the particle size distribution containing a higher fraction of small particles demonstrates a 76 % reduced viscosity in comparison to Tech 1 ink which was processed with a mild grinding technology. Furthermore, it is literature–known that the particle size distribution width plays a key role for the viscosity expression: broad widths including high polydispersity result low viscosity whereas narrow particle size distributions with low polydispersity yield high viscosities respecting the particle mobility.[103,104] Here, the typically known correlation between particle sizes, distribution widths, and viscosity could not be clearly interpreted so that a unknown characteristic is identified as responsible parameter which should be further investigated.

6 CONCLUSION

Several studies present clear correlations between the CL microstructure and its corresponding cell performance.[17,20,29] Especially the correlation of the ionomer loading and the resulting pore structure is well understood.[17,29,45,46,105] It is also known that the CL thickness is determined by the carbon content while its porosity is mainly affected by the supplied ionomer content.[105] The open question is still how these microstructural CL parameters are influenced by the manufacturing process of the catalytic ink and how the catalytic ink itself determines the resulting CL. Hence, this study presents catalytic ink particle size distribution analysis in great detail. Furthermore, characterization methods such as the dispersion state analysis and analytical centrifugation were applied to fuel cell materials for the first time. Moreover, porosimetry analysis was applied and complemented by the implementation of Seaton's advanced pore network characteristics.[91,81] Finally, specific parameters are identified which allow assumptions about the resulting cell performance. These parameters include the aggregation state of the catalyst dispersion D*f*, the modality of the particle size distribution of the ink, the maximal particle size of the distribution x_{max}, the hysteresis loop of the resulting CL, and the specific surface area of the CL. The depicted characteristics for the components ink and CL could also be used for maturity level analysis which is tremendously important for production process optimization which is directly linked to cost reduction. Due to one of the market entry hurdles of high production costs for PEM fuel cells as alternative drive technology, the automotive industry is highly interested in cost reduction which can be achieved by production process efficiency increase or platinum amount reduction (combined with higher platinum utilization).

The prior formulated hypothesis that the fuel cell performance is tunable by the catalytic ink properties, when raw materials and applied production process are fixed, could be confirmed. In order to identify suitable characterization methods the manufacturing process of cathodic electrodes was investigated. Here, static light scattering (SLS) technique was the method of choice for particle size analysis and considered as sensitive to agglomerate/aggregate detection. In order to create diverse catalyst layers, the catalyst ink was processed after 1h, 1d, and 7d of mixing. Further on, the samples were categorized into two groups (Fig. 5.5). Group 1 contains the 1h sample which presented large aggregates of about 10 µm diameter, leading to an aggregated dispersion state and low dispersion stability. Moreover, its resulting catalyst layer was characterized by rough and cracky surface appearance and inhomogeneous material distribution (platinum accumulation; Fig. 5.6 and Fig. 5.8). Additionally, the nitrogen sorption experiments yielded catalyst powder–like sorption behavior indicated by a hysteresis loop type H3 and the presence of macropores (greater 50 nm; Fig. 5.9). This cathodic CL demonstrated low cell performance during electrochemical single cell measurements at 68° C and 100 % RH in comparison to the group 2 samples (1d, 7d electrode; Fig. 5.14). It is assumed that although large macropores are present, which support gas transport, an insufficient primary pore ionomer filling results in low platinum utilization. Thus, the ionomer penetration on the catalyst surface is incomplete so that the accessible catalytic areas are insufficient for adequate cell performance. In contrast, the longer processed catalyst inks yielded catalyst layers whose cell performance is acceptable (Fig. 5.14). Concluding, the mixing time of the catalyst ink is a control lever to influence the resulting CL microstructure. Additionally, the sorption hysteresis of the manufactured catalyst layer can be used as maturity assessment parameter: Catalyst powder–like behavior (H3 type) will yield insufficient cell performance due to lacking catalytic active areas which were only achieved when the ionomer is completely penetrated into the primary pores of the carbon support.

An ionomer study was performed in order to understand the development of primary and secondary pores during manufacturing process. Micropores (< 2 nm) are existent within the primary carbon, while mesopores (2> x< 20 nm, primary pores) exists inside carbon agglomerates and macropores (>20 nm, secondary pores) in between carbon agglomerates.[17,46,59] Primary and secondary pores play a key role during electrochemical reaction: primary pores are usually filled with ionomer and allow dissolved oxygen diffusion and proton migration while secondary pores support gas diffusion and reaction water transport.[20] Thus, a precise ionomer loading adjustment is crucial for ideal cell performance. Hence, the present ionomer study depicted an overall pore volume and specific surface area decrease when ionomer loading is increased (Fig. 5.22). Furthermore, the pore volume fractions for the different types of pores (micro–, meso–, macropore) remains unchanged by ionomer loading variation of 20 % (Fig. 5.23). This means that mainly the catalyst particles and their size distribution are responsible for the CL microstructure. All manufactured catalyst dispersions contributed of similar particles size distributions with a maximal aggregate size less than 10 µm (Fig. 5.17). Only their ionomer loading was varied so that ionomer to carbon ratios of 1.00, 1.10, 1.20, and 1.35 were obtained. The application of Seaton's advanced pore network model contributed to suitable ionomer loading selection.[81,91] Especially the mean coordination number Z results provided additional microstructural insights and are in good agreement with electrochemical single cell testing (Fig. 5.25 and Fig. 5.26).

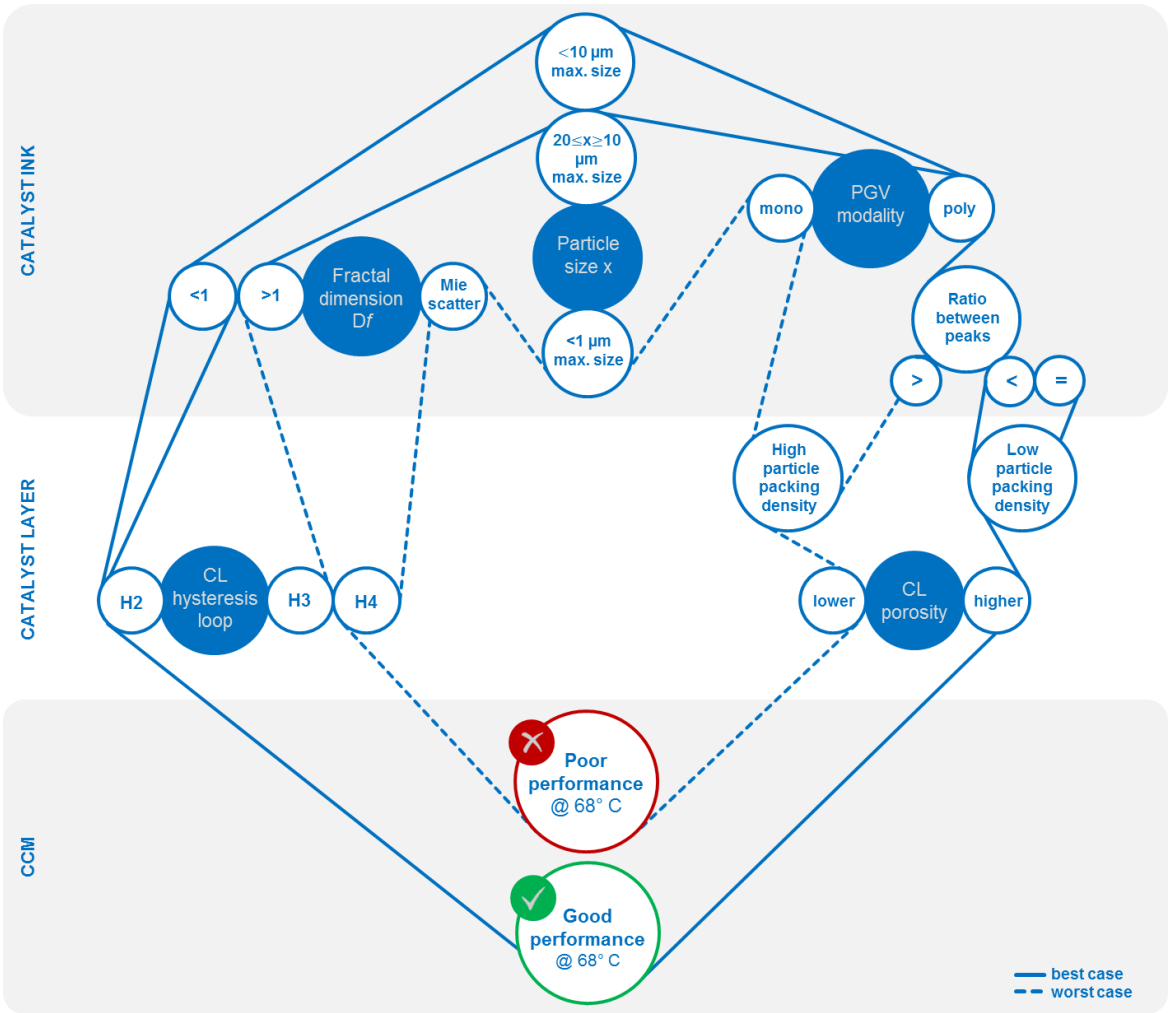

Fig. 6.1 Sketch illustrating the identified component characteristics within the cathodic electrode production and its resulting cell performance. PGV means particle size distribution for the catalyst dispersion. CL hysteresis loops are obtained by nitrogen sorption experiments at 77 K and CL porosity includes both BET surface area and total pore volumes.

All previous experimental findings gave confidence that mainly the catalyst dispersion particle size distribution (PGV) determines the CL microstructure. Fig. 6.1 illustrates the identified characteristics which can be used to predict the resulting cell performance. Five main characteristics are titled but naturally they are influencing related characteristics such as the CL porosity correlates with the CL thickness. Thus, within the catalytic ink, this study depicts the maximum particle size of a particle distribution x_{max}, the fractal dimension D*f* (aggregation state of the dispersion), and the particle size distribution modality as influential parameter. Hence, three distribution designs were created whose characterization reveals the following correlations:

- If the particle size distribution contains aggregates larger or equal 10 µm diameter the catalyst dispersion shows an aggregated dispersion state (D*f* >1). The resulting catalyst layer need to present H2 nitrogen sorption hysteresis loop, equaling mesoporous material, in order to yield acceptable cell performance at normal conditions (68° C, 100 % RH). This parameter is in good agreement with maturity level analysis for the development of catalytic active sites: if the microporous catalyst powder primary pores are sufficiently penetrated with ionomer, the material is transformed into a mesoporous material (H2 type loop). Moreover, catalyst dispersions containing large aggregates usually demonstrate polymodal size distributions: the platinum nanoparticles ranging from 2–5 nm which are attached to primary particles of the catalyst support (carbon), Pt/C particles continue to form agglomerates of approximately 100 nm diameter and form further aggregates of several microns.[17,46] The ratio in between these distribution peaks plays a key role for the particle packing density during drying process. Equal or low volume fractions of the corresponding particle diameter lead to low particle packing density which means in turn a high CL porosity. Thus, this creation of secondary pores determined by the Pt/C skeleton enables suitable diffusion pathways for the reactant gases which directly lead to good cell performance. All this correlated parameters connected by dotted lines demonstrate a best case.

- The same conditions as in the best case scenario are valid but instead of H2 type hysteresis loop a H3 type is present within the investigated electrode. As mentioned before, H3 type demonstrates uncoated catalyst particles which mean in turn less catalytic active sites. Here, the process time of the catalyst dispersion mixing step was too short. Naturally, this type of catalyst layer is coupled with poor CL appearance – cracks, high roughness, and inhomogeneities – and is categorized as worst case.

- Another worse case is a monomodal dispersion whose size distribution is completely below 1 µm. The dispersion state is not analyzable due to occurring Mie scattering which is an indication for monodispersed small particles.[64] Thus, this monomodal distribution leads to extreme high particle packing density and marginally CL porosity, measurable with 50 % reduced CL thickness in comparison to the reference CL. Additional H4 type sorption hysteresis loop underlines the low CL porosity with the presence of the tensile strength effect and slit shaped pores instead of bottleneck pore networks.[59] It is expected that those tiny pores rigorously prevent gaseous transport through the CL.

- Another best case is drawn when the catalyst dispersion particle size distribution is below 10 µm diameter. Here, the dispersion state is depicted as non–aggregated and measurable with D*f* below 1. All other parameters follow the first best case (constant lines in Fig. 6.1). The D*f* characteristic is a great parameter for the overall dispersion state and usually applied to polymeric microcluster analysis.[64,66,67] Within this study it is firstly transferred to fuel cell materials and usable as maturity level for the catalyst dispersion: if D*f* is greater 1, the particle size distribution is larger than 10 µm which also could bear the risk of high dispersion viscosity. Considering a low–risk approach, catalyst dispersions with non–aggregated states (D*f* below 1) should be preferentially be used due to their low viscosity and therefore simple handling during the subsequent coating process. Some observations give an indication that the D*f* value could also bear insight into the ionomer state (relaxed, gelled, etc.) but these assumptions need further examination.

7 OUTLOOK

This chapter includes additional collected results from newly integrated characterization methods. Their interpretation for the production process optimization is not yet completely understood. Thus, the following discussion should be tempting to initiate further research on these topics.

7.1 Hg-intrusion

The standard nitrogen sorption detection range includes 0.35 – 300 nm whereas also macropores of 300 or 400 nm size are detectable (Fig. 7.1, ††).[72,106] But confidence about the existence of macropores could only be gained by applying a method including a larger detection range of several microns. Therefore, mercury intrusion is the method of choice. The mercury intrusion results in Fig. 7.1 (A) cover a measurement range of 3.6 nm to 150 µm whereby the range in between 3 to 20 nm constitutes to primary pores and the range greater than 20 nm includes secondary pores.[17,46] All three electrode designs (1, 2, and 3) clearly differentiate from each other: design 1 CL demonstrate mainly primary pores and a tendency for the presence of micropores (< 2 nm) while design 2 CLs (#3, #4) equally present primary pores and additional secondary pores with a maximum diameter of approximately 100 nm. Their pore size distribution maximal height is found at a diameter of ~55 nm (*). Design 3 CL (#8) is characterized by low pore volumes and demonstrates also a maximal pore diameter of 100 nm. In general, all three designs show related size distribution shaping within the primary pore range. Furthermore, all pores of the three CL designs are located in the nitrogen sorption measurement range except one peak of CL #4 (design 2) which was previously identified as outlier due to the existence of cracks within its CL surface. Hence, this peak at 0.89 µm (Fig. 7.1,**) correlates well with the laser confocal images in Fig. 5.38 (A) although some of the depicted cracks achieve lengths of several microns.

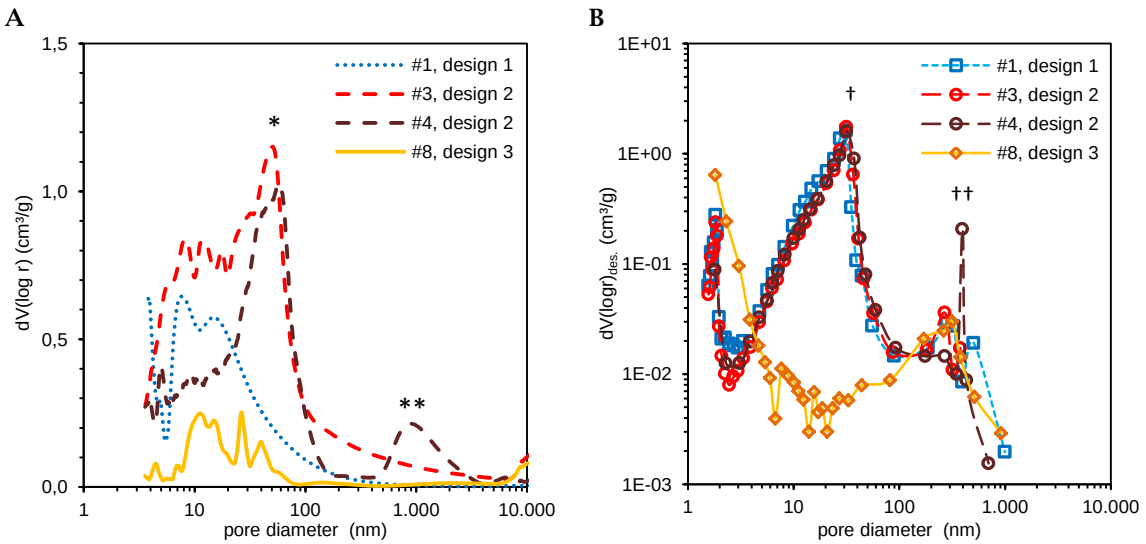

Fig. 7.1 Pore size distribution measured with Hg-intrusion (**A**) and nitrogen sorption (**B**) for diverse CL designs. Peak maxima are highlighted as (*) for Hg-intrusion and (†) nitrogen sorption, respectively.

Fig. 7.1 (B) illustrates the corresponding nitrogen sorption results. Design 1 and 2 are not that clearly differentiated as in the Hg–intrusion results. The peak maximum for design 1 and 2 at ~31 nm (†) is close to that of design 2 for the Hg–intrusion at ~55 nm (*). Moreover, nitrogen sorption results also points an additional peak for sample #4 at 395 nm (††) which is clearly developed at 890 nm (**) for Hg–intrusion method. Design 3 (Sample #8) should not be evaluated further due to measurement artefacts owed by the tensile strength effect for slit shaped pores. In order to interpret the detected PSD shaping differences between Hg–intrusion and nitrogen sorption techniques, Hg–intrusion measurements should be repeated. Furthermore, the mercury intrusion detection range covers 3.6 nm to 150 µm (Fig. 7.1, A) while the standard nitrogen sorption measurements include 0.35 nm to 300 nm (Fig. 7.1, B).[72] The combination of both allows pore size distribution analysis covering a broad range of pore diameters. But still, larger pores of several microns are usually characterized by the application of optical characterization methods such as laser confocal microscopy. Furthermore, mercury intrusion and nitrogen sorption experiments physically base upon diverse mechanisms so that a direct comparison is not suggested. Mercury intrusion follows a penetration process whereas nitrogen sorption is a phase equilibrium process.[82] Some methods exists that transform mercury intrusion data into “mercury desorption isotherm” which finally allows comparison.[82] Hence, it is recommended to transform the obtained data from diverse characterization techniques into comparable parameter so that more information or correlation could be revealed. Further on, a precise failure analysis depending on measurement and preparation errors should be investigated and evaluated in order to validate the experimental findings with respect to the application of a large number of characterization techniques.

Regarding the specific pore volumes obtained from mercury intrusion and nitrogen sorption, remarkable consistencies are detected: design 1 CL presents 0.58 cm^3/g for mercury intrusion and 0.51 cm^3/g for nitrogen sorption, respectively, while design 3 demonstrates corresponding 0.10 cm^3/g for both techniques (Fig. 7.2). In contrast, the design 2 CLs attract attention with large differences of 37 % and 54 % for CL #3 and #4, respectively. Mainly these differences could be related to the presence of pores with diameter larger than 300 nm which are not included within the sorption pore volumes. Moreover, preparation errors such as CL weight determination and the resulting calculation correction could contribute to the differences. Here, sorption experiments performed on a CCM are suggested in order to validate the results collected for the CL on a decal substrate. Furthermore additional porosity determination based on image analysis of CL surfaces and cross–sections are strongly recommended.

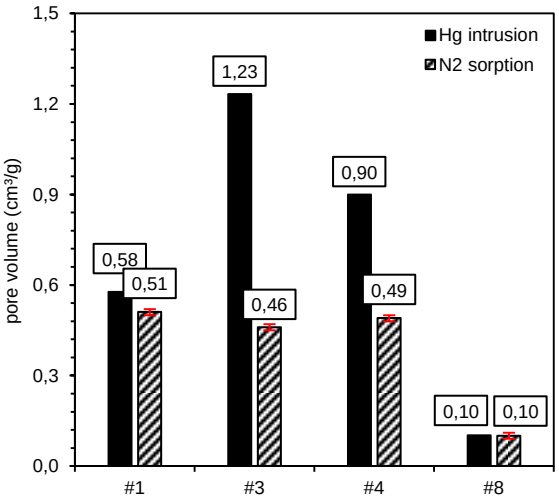

Fig. 7.2 Pore volumes achieved from Hg–intrusion and N_2 sorption porosimetry for diverse catalyst layer designs.

7.2 Functional properties of cathodic catalyst layers

This study includes variation of three parameters mainly influencing the resulting catalyst ink properties – its particle size distribution – and therefore the CL microstructure: (i) the mixing time of the catalyst ink (MT variation), (ii) the ionomer loading variation (I/C variation), and (iii) the particle size distribution variation (PGV variation). The following sequence discusses further functional properties of the cathodic catalyst layers obtained from sheet resistance and adhesion force measurements.

7.2.1 Sheet resistance

The work of Frölich et al. identified the in-plane conductivity of catalyst layers as sensitive characterization method for microstructure variations. It is also assumed that the CLs homogeneity could be deduced from this method. Further on, detected changes in the in-plane conductivity were correlated with variations in the pore network development.[40] Hence, the goal is to design a catalyst layer that is demonstrating high electrical conductivity which means in turn a low sheet resistance so that a high resulting cell performance could be expected.

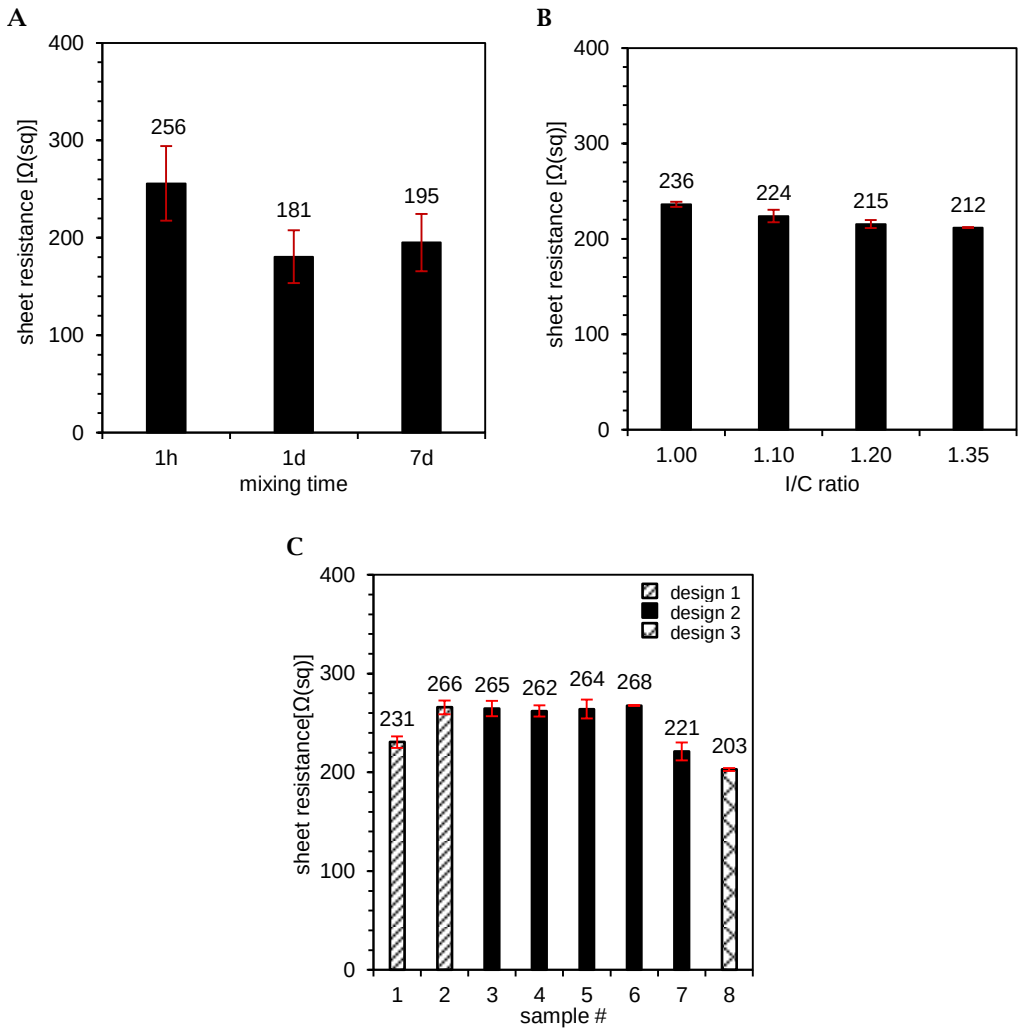

Fig. 7.3 Sheet resistance results archived for diverse catalyst layers whose processing time (**A**), I/C ratio (**B**), and particle size distribution (**C**) was varied within the catalyst ink preparation.

(i) MT variation. Frölich`s work included a process time analysis where resulting catalyst layers obtained from 1d or 8d processed inks are compared. It was found that a shorter process time yielded CLs with higher in–plane conductivity.[40] A similar study was performed within this work. Instead of two time points framing the catalytic ink processing time, three time points were investigated which included 1h, 1d, and 7d. As discussed in chapter 5.1 the samples are categorized into two groups due to their characteristic catalyst layer appearance. The presented sheet resistance results in Fig. 7.3 (A) follow the sample categorization: the CL obtained from a 1h processed ink demonstrated a high sheet resistance of 256 Ω(sq) while longer processed inks resulted in CLs with sheet resistances of averaged 188 Ω(sq). All CLs contain primary and secondary pores but the 1h sample presents a higher fraction of secondary pores and a higher BET surface area (chapter 5.1.2.3). Thus, the high sheet resistance could be related to the large portion of pores which constitute insulating material for electrons so that they need to follow longer conductive pathways. Moreover, large platinum accumulation could also lead to a decrease in sheet resistance as a result of an insufficiently developed carbon network. In contrast, a prolonged processing time minimize these effects so that the sheet resistance decreases. These findings are in good agreement with the electrochemical analysis which presented higher cell performances for the 1d and 7d sample. Thus, a direct correlation between the catalyst layer sheet resistance and its cell performance could be assumed. The difference between the 1d and 7d sample is not considered as significant here but still a slight sheet resistance increase is detectable. Regarding the results of Frölich's work this increase could be remarked feasible but a structural explanation is lacking.

(ii) I/C variation. The ionomer loading influence on the catalyst layer microstructure which is also expected to demonstrate a significant change within the resulting sheet resistance. The results in Fig. 7.3 (B) present only a slight decrease of approximately 5 % for the gradually ionomer loading increase. The sheet resistances for I/C 1.20 and 1.35 are almost identical with 215 Ω(sq) and 212 Ω(sq), respectively. Hence, the obtained results are too close together so that significant structural differences are worthy of discussion. Considering the prior maintained structural insights (chapter 5.2.2) these findings are in good agreement: all CLs contain primary and secondary pores while I/C 1.00 presents the largest pore diameter and CL porosity. Related to the obtained results, it could be assumed that a CL demonstrating large portions of pores and high internal surface area could cause increased sheet resistance which means in turn low electron conductivity. Moreover, these findings are consistent with the prior MT variation results whereby also insulating pores hinder the electric conductivity and therefore increase the sheet resistance.

(iii) PGV variation. Diverse particle size distributions within the catalytic ink lead to different catalyst layer designs. The significant characteristic is the maximum particle size of the size distribution x_{max} which is defined as $20 < x_{max} > 10$ µm for design 1, x_{max} below 10 µm for design 2, and x_{max} below 1 µm for design 3, respectively. Regarding the sheet resistance results in Fig. 7.3 (C) a significant difference (20 %) is only detectable for the design 3 sample (#8) which presents 203 Ω(sq) in contrast to the averaged 254 Ω(sq) for design 2 and 1 samples (#1–#7). Further on, electrochemical analysis validates this finding by major differentiation between design 3 cell performance in comparison to design 2 and 1 CLs (chapter 5.3.3). Thereby, a rapid cell performance breakdown is observed which is related to extremely low CL porosity and absent secondary pores (chapter 5.3.2.2). Thus, the low sheet resistance is overlaid by the tremendously mass transport issues which lead to the insight that the catalyst layer sheet resistance is only one important parameter among many others.

Concluding, the catalyst layer sheet resistance measurement can be used as promising method in order to gain information about the expected cell performance. Further on, microstructural insights can be obtained which could help in catalyst layer design improvement. But the sheet resistance is not independently valid for cell performance prediction. Moreover, since the mass transport is a predominant parameter controlling the electrochemical reaction, the pore network is much more important to the cell performance than the sheet resistance is. Thus, the pore network needs to be adjusted first before electron resistance could be minimized. Furthermore, it is recommended to collect more relevant data so that the sheet resistance share on resulting cell performance can be experimentally quantified.

7.2.2 Adhesion force between catalyst layer and a substrate

The adhesion forces between catalyst layers and a substrate (decal or membrane) are essential parameters for the decal–transfer method. Together with the cohesion between the CL and the membrane these characteristics could be used to identify the process window for the CCM manufacturing.[40] Further on, the adhesion force between the CL and a decal is believed to include structural insight related to the ionomer network development. Therefore, the manufactured catalyst layers obtained from (i) mixing time variation, (ii) ionomer loading variation, and (iii) particle size distribution variation are investigated.

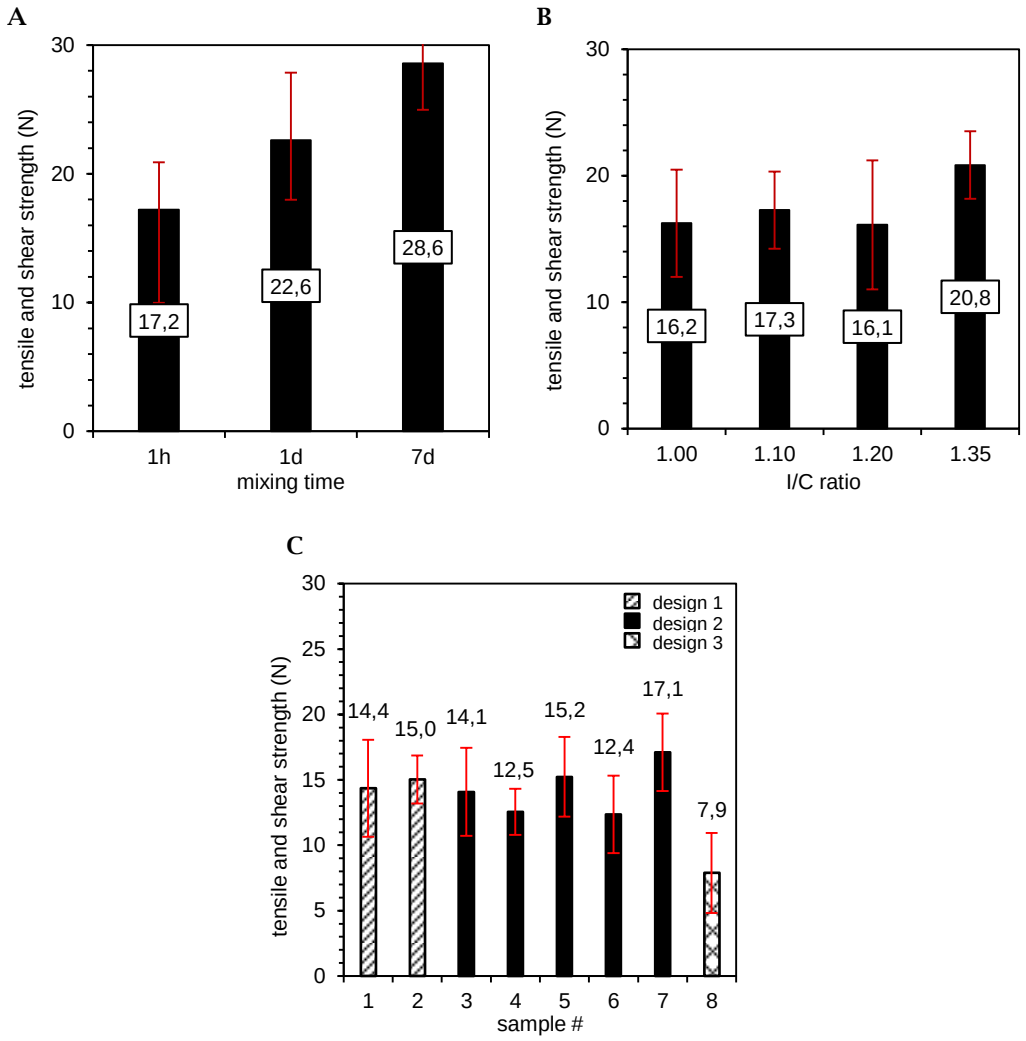

Fig. 7.4 Tensile and shear strength results archived for diverse catalyst layers whose processing time (**A**), I/C ratio (**B**), and particle size distribution (**C**) was varied within the catalyst ink preparation.

(i) *MT variation.* The results in Fig. 7.4 (A) present a tensile and shear strength increase for increased processing time. The CL obtained from a 7d processed ink demonstrate the highest shear and tensile strength of 28.6 N which equals an increase of 40 % from initial 17.2 N for the 1h CL. It is assumed that the ionomer network is growing throughout a prolonged mixing time which leads to a higher adhesion force between the catalyst layer and the decal substrate.

(ii) *I/C variation.* Considering the mixing time variation results, the ionomer network influence the adhesion force between the CL and its substrate. Thus, it is assumed that the ionomer loading also produces significant adhesion force variations. Contrary results are obtained as Fig. 7.4 (B) presents: I/C 1.00 to 1.20 demonstrate similar adhesion forces of averaged 16.5 N and a significant increase of 21 % is measured for I/C 1.35 resulting in 20.8 N. It is feasible that

the high ionomer fraction leads to secondary pore filling which is measurable by an increased adhesion force between CL and decal substrate. Considering the porosity analysis results which also yielded the lowest internal surface area and pore volume for I/C 1.35 in comparison to the other ionomer loadings this assumption can be validated (chapter 5.2.2.3). A direct correlation to cell performance behavior was not identified here but it is important to keep these results in mind when ionomer loadings are varied so that a proper CCM manufacturing process is guaranteed.

(iii) *PGV variation.* Even the particle size distribution variation within catalytic inks did not reveal a significant change within the ionomer network creation since all electrodes contain equal ionomer loading of I/C 1.10. Only design 3 sample #8 presented a significant decrease of 46 % in comparison to the averaged 14.4 N for sample #1– #7 (Fig. 7.4, C). The understanding of ionomer network development is rarely investigated but possibly future work brings further insights. Therefore, it is recommended to correlate the adhesion force measurement results with proton conductivity measurements.

8 APPENDIX

8.1 Samples for chapter 5.1 “Descriptive analysis of cathodic electrode production”.

MT	project	name	DMC KCD	DMC Ink
1h	MT VAR	A LH01-06_WT1h	CCF-141106-LH-006	INK-140729-LH-001
1d	MT VAR	A LH01-06_WT1d	CCF-141106-LH-010	INK-140729-LH-001
7d	MT VAR	ALH01-06_WT7d	CCF-141106-LH-013	INK-140729-LH-001

8.2 Samples for chapter 5.2 “Does the ionomer loading influence the pore size distribution and the overall electrode microstructure characteristics?”.

I/C	project	name	DMC KCD	DMC Ink
1.00	ID08-25	B LH01-04	14279000010000007108532	INK-140930-AH-002
1.10	ID08-24	B LH01-03	14275000010000007108532	INK-140925-LH-001
1.20	ID08-23	B LH01-02	14273000010000007108532	INK-140923-LH-001
1.35	ID08-22	B LH01-01	14176000010000000ID08-22	INK-140618-AM-001

8.3 Samples for chapter 5.3 “CL microstructure tuning by particle size distribution variation of catalytic inks”.

#	project	name	DMC KCD	DMC Ink
1	200m Cathode	v2	14316 KCD-141112-FW-001	INK-141105-AH-001
2	200m Cathode	v4.2	14332 KCD-141128-FW-001	INK-141121-AH-001
3	200m Cathode	v4.1	14330 KCD-141126-FW-001	INK-141119-AH-001
4	B1 100m production	15034	15034000010000007108588	15027000020000007108588
5	200m Cathode	v6	15044 KCD-150213-FW-001	INK-150206-KA-001
6	200m Cathode	v5	15040 KCD-150209-FW-001	INK-150202-KA-001
7	B1 100m production	DBC	14314000020000007108588	14314000010000007108588
8	NMT (Tech 2)	ID10-03	CCF_ID10-03 t-Ende2	INK-150401-RP-001

8.4 Samples for 5.4 “Discussion: Do the ink property settings determine the electrode microstructure independent of the deployed mixing technology?”.

#	project	name	DMC KCD	DMC Ink
Tech 1	B1 100m production	DBC	14314000020000007108588	14314000010000007108588
Tech 2	NMT development (ID10)	ID10–07	1516100001000000KID#4	INK–150603–RP–001

9 REFERENCES

(1) Iván Martén. Why Future Oil Demand Could Be Very Low. http://blogs.wsj.com/experts/2015/04/28/why-future-oil-demand-could-be-very-low/.

(2) Amsterdam Roundtable Foundation and McKinsey & Company The Netherlands. Evolution: Electric vehicles in Europe: gearing up for a new phase? http://www.mckinsey.com/global_locations/europe_and_middleeast/netherlands/en/latest_thinking.

(3) Franco, A. A. *Polymer electrolyte fuel cells: Science, applications, and challenges*; Pan Stanford: Boca Raton, FL, 2013.

(4) Daimler AG. H2 Mobility initiative: Leading industrial companies agree on an action plan for the construction of a hydrogen refuelling network in Germany. http://media.daimler.com/dcmedia/0-921-656547-1-1636552-1-0-0-0-0-0-11694-0-0-1-0-0-0-0-0.html.

(5) Daimler AG. Filling up with hydrogen will be possible Germany-wide in future. http://media.daimler.com/dcmedia/0-921-657589-1-1855351-1-0-0-0-0-1-0-614316-0-1-0-0-0-0-0.html?TS=1452604830278.

(6) E4tech. The Fuel Cell Industry Review 2015. www.FuelCellIndustryReview.com.

(7) European Commission. Reducing CO2 emissions from passenger cars: Policy. http://ec.europa.eu/clima/policies/transport/vehicles/cars/index_en.htm.

(8) M. Ringel, A. Taylor, H. Zablit. The Most Innovative Companies 2015: Four Factors That Differentiate Leaders. https://media-publications.bcg.com/MIC/BCG-Most-Innovative-Companies-2015.pdf.

(9) Jörn Thomas. Zu Besuch bei Tesla in den USA. http://www.auto-motor-und-sport.de/news/kleinserien-hersteller-tesla-zu-besuch-bei-tesla-in-den-usa-2744055.html.

(10) Jerry Hirsch. Elon Musk: Model S not a car but a 'sophisticated computer on wheels'. http://www.latimes.com/business/autos/la-fi-hy-musk-computer-on-wheels-20150319-story.html.

(11) Forbes.com LLC™. The World's Most Innovative Companies 2015. http://www.forbes.com/innovative-companies/list/.

(12) Toyota Motor Sales. Mirai – The Toyota Fuel Cell Vehicle. https://ssl.toyota.com/mirai/fcv.html.

(13) BMW Group. BMW i3. https://www.bmw.de/de/neufahrzeuge/bmw-i/i3/2015/erleben.html?uncert.

(14) Daimler AG. Unternehmensgeschichte: Die Daimler AG: Weltweite Rezession und glänzendes Comeback (2008 – 2009). http://www.daimler.com/konzern/tradition/geschichte/2008-2009.html.

(15) NuCellSys GmbH. Mercedes–Benz F–CELL World Drive. http://www.nucellsys.com/index.dhtml/3056962081338310951h/-/deDE/-/CS/-/Unternehmen/News/201011_News_17112010.

(16) X. Mosquet, M. Russo, K. Wagner, H. Zablit, A. Arora. Accelerating Innovation: New Challenges for Automakers. https://www.bcgperspectives.com/content/articles/automotive_innovation_accelerating_innovation_new_challenges_automakers/.

(17) Eikerling, M.; Kulikovsky, A. A. *Polymer electrolyte fuel cells: Physical principles of materials and operation*; CRC Press Taylor & Francis Group CRC Press is an imprint of the Taylor & Francis Group an informa business: Boca Raton, 2015.

(18) Hartnig, C.; Roth, C. *Polymer electrolyte membrane and direct methanol fuel cell technology*; Woodhead Publishing series in energy no. 31; Woodhead Publishing: Cambridge, England, Philadelphia, Pennsylvania, 2012.

(19) Qi, Z. *Proton exchange membrane fuel cells*; Electrochemical energy storage and conversion.

(20) Khajeh–Hosseini–Dalasm, N.; Fesanghary, M.; Fushinobu, K.; Okazaki, K. A study of the agglomerate catalyst layer for the cathode side of a proton exchange membrane fuel cell: Modeling and optimization. *Electrochimica Acta* **2012**, *60*, 55–65. DOI: 10.1016/j.electacta.2011.10.099.

(21) Jaouen, F.; Lindbergh, G.; Sundholm, G. Investigation of Mass–Transport Limitations in the Solid Polymer Fuel Cell Cathode. *J. Electrochem. Soc.* **2002**, *149* (4), A437. DOI: 10.1149/1.1456916.

(22) Lin, G.; He, W.; van Nguyen, T. Modeling Liquid Water Effects in the Gas Diffusion and Catalyst Layers of the Cathode of a PEM Fuel Cell. *J. Electrochem. Soc.* **2004**, *151* (12), A1999. DOI: 10.1149/1.1808633.

(23) Du, C. Y.; Cheng, X. Q.; Yang, T.; Yin, G. P.; Shi, P. F. Numerical simulation of the ordered catalyst layer in cathode of proton exchange membrane fuel cells. *Electrochemistry Communications* **2005**, *7* (12), 1411–1416. DOI: 10.1016/j.elecom.2005.09.022.

(24) Sun, W.; Peppley, B. A.; Karan, K. An improved two–dimensional agglomerate cathode model to study the influence of catalyst layer structural parameters. *Electrochimica Acta* **2005**, *50* (16–17), 3359–3374. DOI: 10.1016/j.electacta.2004.12.009.

(25) Chisaka, M.; Daiguji, H. Design of ordered–catalyst layers for polymer electrolyte membrane fuel cell cathodes. *Electrochemistry Communications* **2006**, *8* (8), 1304–1308. DOI: 10.1016/j.elecom.2006.06.009.

(26) Secanell, M.; Karan, K.; Suleman, A.; Djilali, N. Multi–variable optimization of PEMFC cathodes using an agglomerate model. *Electrochimica Acta* **2007**, *52* (22), 6318–6337. DOI: 10.1016/j.electacta.2007.04.028.

(27) Kamarajugadda, S.; Mazumder, S. Numerical investigation of the effect of cathode catalyst layer structure and composition on polymer electrolyte membrane fuel cell performance. *Journal of Power Sources* **2008**, *183* (2), 629–642. DOI: 10.1016/j.jpowsour.2008.05.072.

(28) Akabori, S.; Suzuki, K.; Tabe, Y.; Chikahisa, T. Analysis of Cathode Catalyst Layer Structure and Cell Performance in PEFC. *ECS Transactions* **2014**, *64* (3), 305–312. DOI: 10.1149/06403.0305ecst.

(29) Uchida, M. Effects of Microstructure of Carbon Support in the Catalyst Layer on the Performance of Polymer–Electrolyte Fuel Cells. *J. Electrochem. Soc.* **1996**, *143* (7), 2245. DOI: 10.1149/1.1836988.

(30) Epting, W. K.; Litster, S. Effects of an agglomerate size distribution on the PEFC agglomerate model. *International Journal of Hydrogen Energy* **2012**, *37* (10), 8505–8511. DOI: 10.1016/j.ijhydene.2012.02.099.

(31) Dr. Wolfgang Bernhart, Stefan Riederle, Manuel Yoon. *Fuel cells - A realistic alternative for zero emission?*, 2013.

(32) Spendelow, J., Marcinkoski, J. DOE Hydrogen and Fuel Cells Program Record. http://energy.gov/sites/prod/files/2015/06/f22/14014_fuel_cell_system_cost_2014.pdf.

(33) James, B. D., Moton, J. M., Colella, W. G. Mass Production Cost Estimation of Direct H2 PEM Fuel Cell Systems for Transportaion Applications: 2013 Update.

(34) James, B. D., Kalinoski, J. A., Baum, K. N. Mass Production Cost Estimation for Direct H2 PEM Fuel Cell Systems for Automotive Applications: 2009 Update.

(35) *Polymer Membranes for Fuel Cells;* Javaid, Z. S., Matsuura, T., Eds.; Springer US: Boston, MA, 2009.

(36) Franco, A. A. *Polymer electrolyte fuel cells: Science, applications, and challenges*; Science, applications, and challenges; PAN Stanford Publishing: Singapore, 2013.

(37) J. Kleemann,F. Finsterwalder,W. Tillmetz. Characterisation of mechanical behaviour and coupled electrical properties of polymer electrolyte membrane fuel cell gas diffusion layers. *Journal of Power Sources* **2009**, *190* (1), 92–102. DOI: 10.1016/j.jpowsour.2008.09.026.

(38) Kurzweil, P. *Brennstoffzellentechnik: Grundlagen, Komponenten, Systeme, Anwendungen*; Grundlagen, Komponenten, Systeme, Anwendungen; Springer Vieweg: Wiesbaden, 2013.

(39) Bach, S. M. *Neue Charakterisierungsmethoden für die Gasdiffusionslage in PEM-Brennstoffzellen vor dem Hintergrund produktionsprozessbedingter Materialschwankungen*; Schriften des Forschungszentrums Jülich Reihe Energie & Umwelt / Energy & Environment Band 286.

(40) Frölich, K. *Der Decal-Prozess zur Herstellung katalysatorbeschichteter Membranen für PEM-Brennstoffzellen*; Schriftenreihe des Instituts für Angewandte Materialien 47; KIT Scientific Publishing: Karlsruhe, 2015.

(41) Wilson, M. S.; Valerio, J. A.; Gottesfeld, S. Low platinum loading electrodes for polymer electrolyte fuel cells fabricated using thermoplastic ionomers. *Polymer electrolyte fuel cells* [Online] **1995**, *40* (3), 355–363. http://www.sciencedirect.com/science/article/pii/0013468694002723.

(42) Yang, T.–H.; Yoon, Y.–G.; Park, G.–G.; Lee, W.–Y.; Kim, C.–S. Fabrication of a thin catalyst layer using organic solvents. *Eighth Ulmer Electrochemische Tage* [Online] **2004**, *127* (1–2), 230–233. http://www.sciencedirect.com/science/article/pii/S037877530300956X.

(43) Chisaka, M.; Matsuoka, E.; Daiguji, H. Effect of Organic Solvents on the Pore Structure of Catalyst Layers in Polymer Electrolyte Membrane Fuel Cells. *J. Electrochem. Soc.* **2010**, *157* (8), B1218. DOI: 10.1149/1.3439617.

(44) Ngo, T. T.; Yu, T. L.; Lin, H.–L. Influence of the composition of isopropyl alcohol/water mixture solvents in catalyst ink solutions on proton exchange membrane fuel cell performance. *Journal of Power Sources* **2013**, *225*, 293–303. DOI: 10.1016/j.jpowsour.2012.10.055.

(45) Uchida, M. Investigation of the Microstructure in the Catalyst Layer and Effects of Both Perfluorosulfonate Ionomer and PTFE–Loaded Carbon on the Catalyst Layer of Polymer Electrolyte Fuel Cells. *J. Electrochem. Soc.* **1995**, *142* (12), 4143. DOI: 10.1149/1.2048477.

(46) Soboleva, T.; Zhao, X.; Malek, K.; Xie, Z.; Navessin, T.; Holdcroft, S. On the Micro–, Meso–, and Macroporous Structures of Polymer Electrolyte Membrane Fuel Cell Catalyst Layers. *ACS Appl. Mater. Interfaces* **2010**, *2* (2), 375–384. DOI: 10.1021/am900600y.

(47) Tabe, Y.; Nishino, M.; Takamatsu, H.; Chikahisa, T. Effects of Cathode Catalyst Layer Structure and Properties Dominating Polymer Electrolyte Fuel Cell Performance. *J. Electrochem. Soc.* **2011**, *158* (10), B1246. DOI: 10.1149/1.3624606.

(48) Mukherjee, P. P.; Wang, C.–Y. Stochastic Microstructure Reconstruction and Direct Numerical Simulation of the PEFC Catalyst Layer. *J. Electrochem. Soc.* **2006**, *153* (5), A840. DOI: 10.1149/1.2179303.

(49) Secanell, M.; Carnes, B.; Suleman, A.; Djilali, N. Numerical optimization of proton exchange membrane fuel cell cathodes. *Electrochimica Acta* **2007**, *52* (7), 2668–2682. DOI: 10.1016/j.electacta.2006.09.049.

(50) Lekkerkerker, Henk N. W.; Tuinier, R. *Colloids and the Depletion Interaction* 833; Springer Netherlands: Dordrecht, 2011.

(51) Meakin, P. Fractal aggregates. *Advances in Colloid and Interface Science* **1987**, *28*, 249–331. DOI: 10.1016/0001–8686(87)80016–7.

(52) Schlumbohm, C. *Stabilitäts- und Strukturmodifikationen in Katalysatordispersionen der Direktmethanolbrennstoffzelle*; Schriften des Forschungszentrums Jülich. Reihe Energietechnik Schriften des Forschungszentrums Jülich. Energy technology v. 48; Forschungszentrum Jülich, Zentralbibliothek: Jülich, 2006.

(53) O'Hayre, R. P. *Fuel cell fundamentals*, 2nd ed.; John Wiley and Sons: Hoboken, 2009.

(54) Grot, W. *Fluorinated ionomers*; PDL handbook series; PDL/Plastics Design Library; William Andrew Pub: Norwich, NY, 2008.

(55) Mauritz, K.; Moore, R. B. State of understanding of Nafion. *CHEMICAL REVIEWS* [Online] **2004**, 4535–4585. http://aquila.usm.edu/fac_pubs/2996.

(56) Panik, F. Fuel cells for vehicle applications in cars – bringing the future closer. *Journal of Power Sources* [Online] **1998**, *71* (1–2), 36–38. http://www.sciencedirect.com/science/article/pii/S037877539702805X.

(57) Soboleva, T.; Malek, K.; Xie, Z.; Navessin, T.; Holdcroft, S. PEMFC catalyst layers: the role of micropores and mesopores on water sorption and fuel cell activity. *ACS Appl. Mater. Interfaces* **2011**, *3* (6), 1827–1837. DOI: 10.1021/am200590w.

(58) Zhang, J. *PEM fuel cell electrocatalysts and catalyst layers: Fundamentals and applications*; Springer: London, 2008.

(59) Sing, K. S. W. Reporting physisorption data for gas/solid systems with special reference to the determination of surface area and porosity (Recommendations 1984). *Pure and Applied Chemistry* **1985**, *57* (4). DOI: 10.1351/pac198557040603.

(60) Eikerling, M. Water Management in Cathode Catalyst Layers of PEM Fuel Cells. *J. Electrochem. Soc.* **2006**, *153* (3), E58. DOI: 10.1149/1.2160435.

(61) International Organization for Standardization. *Particle size analysis - Laser diffraction methods*, 2009, *19.120* (ISO 13320:2009). http://www.iso.org/iso/catalogue_detail.htm?csnumber=44929.

(62) Alderliesten, M. Mean Particle Diameters. Part II: Standardization of nomenclature. *Part. Part. Syst. Charact.* **1991**, *8* (1–4), 237–241. DOI: 10.1002/ppsc.19910080143.

(63) International Organization for Standardization. *Representation of results of particle size analysis - Part 1: Graphical representation*, 1998, *19.120* (ISO 9276–1:1998). http://www.iso.org/iso/home/store/catalogue_tc/catalogue_detail.htm?csnumber=25860.

(64) Sorensen, C. M. Light Scattering by Fractal Aggregates: A Review. *Aerosol Science and Technology - AEROSOL SCI TECH* **2001**, *35* (2), 648–687. DOI: 10.1080/02786820117868.

(65) Bushell, G. C.; Yan, Y. D.; Woodfield, D.; Raper, J.; Amal, R. On techniques for the measurement of the mass fractal dimension of aggregates. *Advances in Colloid and Interface Science* [Online] **2002**, *95* (1), 1–50. http://www.sciencedirect.com/science/article/pii/S0001868600000786.

(66) Mays, D. C.; Cannon, O. T.; Kanold, A. W.; Harris, K. J.; Lei, T. C.; Gilbert, B. Static light scattering resolves colloid structure in index-matched porous media. *Journal of Colloid and Interface Science* **2011**, *363* (1), 418–424. DOI: 10.1016/j.jcis.2011.06.046.

(67) Schärtl, W. *Light Scattering from Polymer Solutions and Nanoparticle Dispersions*; Springer Berlin Heidelberg: Berlin, Heidelberg, 2007.

(68) International Organization for Standardization. *Determination of particle size distribution by centrifugal liquid sedimentation methods - Part 2: Photocentrifuge method*, 2007, *19.120* (ISO 13318–2:2007). http://www.iso.org/iso/catalogue_detail.htm?csnumber=45771.

(69) LUM GmbH. *Tutorial LUMiSizer® & LUMiFuge® advanced.*

(70) Daimler AG. *Testspezifikation für SNA an Membranmaterialien: VA0102001*. Rev002A.

(71) Otsu. A Threshold Selection Method from Gray-Level Histograms. *IEEE Trans. Syst., Man, Cybern.* **1979**, *9* (1), 62–66. DOI: 10.1109/TSMC.1979.4310076.

(72) Scarlett, B.; Lowell, S.; Shields, J. E.; Thomas, M. A.; Thommes, M. *Characterization of Porous Solids and Powders: Surface Area, Pore Size and Density* 16; Springer Netherlands: Dordrecht, 2004.

(73) DIN Deutsches Institut für Nomung e.V. *Determination of the pore size distribution and the specific surface area of mesoporous solids by means of nitrogen sorption - Method of Barrett, Joyner and Halenda (BJH)*; Beuth Verlag GmbH, 1998 (DIN 66134:1998–02).

(74) DIN Deutsches Institut für Nomung e.V. *Pore size analysis - Representation of pore size distributions*; Beuth Verlag GmbH, 2010, *ICS 17.040.20; 19.120* (DIN 66139:2010–02).

(75) Neimark, A. V.; Lin, Y.; Ravikovitch, P. I.; Thommes, M. Quenched solid density functional theory and pore size analysis of micro–mesoporous carbons. *Carbon* [Online] **2009**, *47* (7), 1617–1628. file://www.sciencedirect.com/science/article/pii/S0008622309000633.

(76) Ravikovitch, P. I.; Neimark, A. V. Density Functional Theory Model of Adsorption on Amorphous and Microporous Silica Materials. *Langmuir* [Online] **2006**, *22* (26), 11171–11179. http://dx.doi.org/10.1021/la0616146.

(77) Kruk, M.; Jaroniec, M. Gas Adsorption Characterization of Ordered Organic–Inorganic Nanocomposite Materials. *Chem. Mater.* **2001**, *13* (10), 3169–3183. DOI: 10.1021/cm0101069.

(78) International Organization for Standardization. *Determination of the specific surface area of solids by gas adsorption - BET method*, 2010, *19.120* (ISO 9277:2010).

(79) Seaton, N. A. Determination of the connectivity of porous solids from nitrogen sorption measurements. *Chemical Engineering Science* [Online] **1991**, *46* (8), 1895–1909. http://www.sciencedirect.com/science/article/pii/000925099180151N.

(80) Liu, H.; Zhang, L.; Seaton, N. A. Determination of the connectivity of porous solids from nitrogen sorption measurements — II. Generalisation. *Chemical Engineering Science* [Online] **1992**, *47* (17–18), 4393–4404. http://www.sciencedirect.com/science/article/pii/000925099285117T.

(81) Liu, H.; Seaton, N. A. Determination of the connectivity of porous solids from nitrogen sorption measurements—III. Solids containing large mesopores. *Chemical Engineering Science* **1994**, *49* (11), 1869–1878. DOI: 10.1016/0009–2509(94)80071–5.

(82) Murray, K. L.; Seaton, N. A.; Day, M. A. Use of Mercury Intrusion Data, Combined with Nitrogen Adsorption Measurements, as a Probe of Pore Network Connectivity. *Langmuir* **1999**, *15* (23), 8155–8160. DOI: 10.1021/la990250x.

(83) Zhdanov, V. P.; Fenelonov, V. B.; Efremov, D. K. Determination of pore–size distribution from sorption isotherms: Application of percolation theory. *Journal of Colloid and Interface Science* [Online] **1987**, *120* (1), 218–223. http://www.sciencedirect.com/science/article/pii/0021979787903432.

(84) KIRKPATRICK, S. Models of disordered materials. In *Ill-Condensed Matter*; Balian, R., Maynard, R., Toulouse, G., Eds.; CO–PUBLISHED WITH NORTH–HOLLAND PUBLISHING CO, 1984; pp 321–403.

(85) DIN Deutsches Institut für Nomung e.V. *Determination of pore volume distribution and specific surface area of solids by mercury intrusion*; Beuth Verlag GmbH, 1993 (DIN 66133:1993–06).

(86) Lu, Bowler, Bowler, Huang. Edge effects in four–point direct current potential drop measurements on metal plates. *Journal of Physics D: Applied Physics* [Online] **2009**, *42* (13), 135004. http://stacks.iop.org/0022–3727/42/i=13/a=135004.

(87) Nicolas Karsta,∗, Vincent Faucheuxb, Audrey Martinentb, Pierre Bouillona. Improvement of water management in polymer electrolyte membrane fuel cell thanks to cathode cracks. *Journal of Power Sources* **2010.** DOI: 10.1016/j.jpowsour.2010.03.025.

(88) Lim, C. Y., Haas, H. *Diagnostic method for an electrochemical fuel cell and fuel cell components*; Google Patents, 2006. https://www.google.ch/patents/US20060051628.

(89) Moussa, A. S.; Soos, M.; Sefcik, J.; Morbidelli, M. Effect of Solid Volume Fraction on Aggregation and Breakage in Colloidal Suspensions in Batch and Continuous Stirred Tanks. *Langmuir* **2007**, *23* (4), 1664–1673. DOI: 10.1021/la062138m.

(90) Kolb, M.; Botet, R.; Jullien, R. Scaling of Kinetically Growing Clusters. *Phys. Rev. Lett.* **1983**, *51* (13), 1123–1126.

(91) Liu, H.; Zhang, L.; Seaton, N. A. Sorption hysteresis as a probe of pore structure. *Langmuir* **1993**, *9* (10), 2576–2582. DOI: 10.1021/la00034a016.

(92) Lowell, S.; Shields, J. E. *Powder Surface Area and Porosity*, Third Edition; Powder Technology Series 2.

(93) Lippens, B. C.; de Boer, J. H. Studies on pore systems in catalysts: V. The t method. *Journal of Catalysis* [Online] **1965**, *4* (3), 319–323. file://www.sciencedirect.com/science/article/pii/0021951765903076.

(94) Song, D.; Wang, Q.; Liu, Z.; Eikerling, M.; Xie, Z.; Navessin, T.; Holdcroft, S. A method for optimizing distributions of Nafion and Pt in cathode catalyst layers of PEM fuel cells. *Electrochimica Acta* **2005**, *50* (16–17), 3347–3358. DOI: 10.1016/j.electacta.2004.12.008.

(95) Murgia, G.; Pisani, L.; Shukla, A. K.; Scott, K. A Numerical Model of a Liquid–Feed Solid Polymer Electrolyte DMFC and Its Experimental Validation. *J. Electrochem. Soc.* **2003**, *150* (9), A1231. DOI: 10.1149/1.1596951.

(96) Norio Ouchiyama, T. T. "Porosity of a Mass of Solid Particles Having a Range of Sizes". *Industrial & Engineering Chemistry Fundamentals* **1981**, *20* (1). DOI: 10.1021/i100001a013.

(97) A. B. Yu,N. Standish; Yu, A. B.; Standish, N. Estimation of the Porosity of Particle Mixtures by a Linear–Mixture Packing Model // Estimation of the porosity of particle mixtures by a linear-mixture packing model. *Industrial & Engineering Chemistry Research - IND ENG CHEM RES* **1991**, *30* (6), 1372–1385. DOI: 10.1021/ie00054a045.

(98) Ricardo P. Dias,José A Teixeira,Manuel G. Mota,Alexander I. Yelshin. Particulate Binary Mixtures: Dependence of Packing Porosity on Particle Size Ratio. *Industrial & Engineering Chemistry Research - IND ENG CHEM RES* **2004**, *43* (24). DOI: 10.1021/ie040048b.

(99) Burgess, C. G. V; Everett, D. H. The lower closure point in adsorption hysteresis of the capillary condensation type. *Journal of Colloid and Interface Science* **1970**, *33* (4), 611–614. DOI: 10.1016/0021–9797(70)90014–7.

(100) Woo, H.–J.; Sarkisov, L.; Monson, P. A. Mean–Field Theory of Fluid Adsorption in a Porous Glass. *Langmuir* **2001**, *17* (24), 7472–7475. DOI: 10.1021/la015532n.

(101) Meyer, K.; Klobes, P. Comparison between different presentations of pore size distribution in porous materials. *Fresenius' Journal of Analytical Chemistry* **1999**, *363* (2), 174–178. DOI: 10.1007/s002160051166.

(102) Wang, Y.; Chen, K. S.; Mishler, J.; Cho, S. C.; Adroher, X. C. A review of polymer electrolyte membrane fuel cells: Technology, applications, and needs on fundamental research. *Applied Energy* **2011**, *88* (4), 981–1007. DOI: 10.1016/j.apenergy.2010.09.030.

(103) Bauckhage, K. Die Viskosität von Suspensionen. Teil I Beschreibung des Fließverhaltens und Bestimmung der Fließkurven. *Chemie Ing. Techn.* **1973**, *45* (15), 1001–1004. DOI: 10.1002/cite.330451512.

(104) Lagaly, G.; Schulz, O.; Zimehl, R. *Dispersionen und Emulsionen: Eine Einführung in die Kolloidik feinverteilter Stoffe einschließlich der Tonminerale*; Steinkopff: Darmstadt, 1997.

(105) Suzuki, T.; Tsushima, S.; Hirai, S. Effects of Nafion® ionomer and carbon particles on structure formation in a proton–exchange membrane fuel cell catalyst layer fabricated by the decal-transfer method. *International Journal of Hydrogen Energy* **2011**, *36* (19), 12361–12369. DOI: 10.1016/j.ijhydene.2011.06.090.

(106) Murray, K. L.; Seaton, N. A.; Day, M. A. An Adsorption–Based Method for the Characterization of Pore Networks Containing Both Mesopores and Macropores. *Langmuir* **1999**, *15* (20), 6728–6737. DOI: 10.1021/la990159t.